The Pennsylvania State University

The Graduate School

John and Willie Leone Family Department of Energy and Mineral Engineering

CHARACTERIZATION OF GAS-CHARGED POROUS MEDIA FROM JOINT INVERSION OF P/S- WAVE ATTENUATION BASED ON OBS AND/OR SONIC LOG DATA

A Dissertation in

Energy and Mineral Engineering

by

Xiong Lei

Submitted in Partial Fulfillment
of the Requirements
for the Degree of

Doctor of Philosophy

August 2018

The dissertation of Xiong Lei was reviewed and approved* by the following:

Eugene Morgan
Assistant Professor of Petroleum and Natural Gas Engineering
Dissertation Advisor
Chair of Committee

Derek Elsworth
Professor of Energy and Geo-Environmental Engineering

Hamid Emami-Meybodi
Assistant Professor of Petroleum and Natural Gas Engineering

Sridhar Anandakrishnan
Professor of Geosciences

Tieyuan Zhu
Assistant Professor of Geosciences

Luis F. Ayala H.
William A. Fustos Family Professor
Professor of Petroleum and Natural Gas Engineering
Associate Department Head for Graduate Education

*Signatures are on file in the Graduate School

ABSTRACT

Attenuation refers to the exponential decay of wave amplitude with distance. It is caused by energy-conserved factors (scattering or geometric dispersion), and inelastic dissipation (intrinsic attenuation) where energy is converted into heat. The intrinsic attenuation is frequency dependent and of interest to exploration geophysics, including application in wave propagation forward modeling, signal filtering, gas detection, full waveform inversion, and, as focused on in this dissertation, reservoir property estimation. We characterize gas reservoir by intrinsic attenuation inversion. The advantages of seismic attenuation inversion are that attenuation has a stronger relationship to hydraulic properties than velocity, and gas has more pronounced effects in terms of attenuation. The proposed methodology is easily extendable to oil and other types of reservoirs.

The foundation of seismic attenuation inversion is the measurement of quality factor, *Q*, which is inversely proportional to attenuation. However, it is difficult to estimate *Q* from reflection data due to the presence of noise intervention, which limits its application. Many methods have been proposed for *Q* estimation mainly for VSP (vertical seismic profile), crosswell, or transmitted data. With this study, we extend those approaches to reflection data. However, the specific techniques to cope with the corresponding issues, comparison of the efficacy for different approaches, and a clear recommendation on which methods are the best to use under which circumstances are rarely presented. The first part of this thesis is dedicated to resolve these issues using synthetic seismic data. We focus on three frequency-domain methods: spectral ratio method (SRM), centroid frequency shift method (CFS), and peak frequency shift method (PFS). They are less affected by scattering interference compared with time-domain methods. For the three frequency-domain methods, five kinds of pre-processing procedures paired with them are tested. We first determine the optimal length of the window function (for seismic signal frequency transformation). Secondly, we find that a traditional FFT coupled with either the SRM or CFS

methods works the best and about equally well in terms of Q estimation error under various levels of noise. A close second is a technique that involves the extraction of wavelets from the signal and their subsequent frequency transformation, again coupled with either SRM or CFS. It is noted that this technique is superior when dealing with thin layers because of its stronger capability of wavelet restoration. Additionally, we find that Q tends to be more accurately estimated for layers with higher attenuation. Moreover, the effective-bandwidth coefficients, which control the length of the effective signal participating in the Q estimation, from 0.2 ~ 0.4 are good values.

Then, I show that the joint inversion of P- and S-wave quality factor (Q_p and Q_s) is powerful in characterizing gas-bearing porous media. Compared to the inversion of Q_p alone, where a rock physics model giving Q_p as an output is inverted for its input parameters (rock and fluid properties), the joint inversion has one more dimension of information, increasing constraints on the model to suppress the occurrence of multiple solutions. Additionally, joint inversion improves the model sensitivity to the input parameters, enhancing its reliability. Moreover, besides porosity, it allows us to invert one more parameter, here gas saturation. In this section, we implement the inversion workflow on the ocean bottom seismometer (OBS) data from Finneidfjord, Norway, where the free-gas accumulation takes place in the sub-seabed. After sensitivity analysis, the efficacy of the inversion for gas saturation and porosity is verified. The nonsensitive parameters are eliminated from the inversion and set as constants, which reduces the complexity of the problem. By using Differential-Evolution MCMC scheme, we efficiently sample the joint posterior of the saturation and porosity. The estimated gas saturation and porosity (modes of the posteriors) agree with previous research in Finneidfjord.

So far, we just discuss and invert the porosity and saturation. The next step would be to invert more solvable unknowns by introducing more information. In the final part of the research, we integrate multiple geophysical datasets (OBS and sonic logs) to realize a more advanced joint inversion. Usually, both the compressional and shear wave sonic waveform data has higher

frequencies than seismic. At the two different frequencies, we can have two pairs of Q_p, Q_s. Adding two more dimensions to the inverse problem constrain the inversion even further, thus reducing uncertainty in estimates and improving the number of the solvable parameters. After establishing the workflow, we take the Hydrate Ridge, Oregon margin where there is free gas accompanied beneath the gas hydrate as a practical example to show the validity of a four-parameter inversion. The gas saturation, porosity, permeability, and characteristic (inclusion) size are simultaneously inverted and in good agreement with the literature about the Hydrate Ridge.

TABLE OF CONTENTS

List of Figures viii

List of Tables xiii

Acknowledgements xiv

Chapter 1 Introduction 1

1.1 Literature Review 5
1.1.1 Gas Saturation 5
1.1.2 Porosity 6
1.1.3 Permeability 7
1.1.4 Other Properties 8
1.1.6 Multicomponent Seismic Data 10
1.1.7 Quality Factor Measurement 11
1.1.8 Rock Physics Model for Seismic Attenuation 12
1.1.9 Stochastic Optimization Algorithm 14
1.2 Statement of the Problem 16
1.3 Novelties of This Thesis 20
1.4 Reference 21

Chapter 2 A Comparison of Methods for Estimating Q 28

2.1 Abstract 28
2.2 Introduction 29
2.3 Methods 36
2.3.1 Technique I 36
2.3.2 Technique II 38
2.3.3 Technique III 38
2.3.4 Technique IV 39
2.3.5 Technique V 40
2.4 Numerical Example 41
2.5 Results and Discussion 44
2.5.1 Window Size Test 44
2.5.2 Comparison of Methods/Techniques for S/N = ∞ and f_p = 50 Hz 46
2.5.3 S/N Analysis for f_p = 50 Hz 51
2.5.4 High Frequency Case (f_p = 1500 Hz) 53
2.5.5 “Thin-layer” Effect 55
2.6 Conclusion 56
2.7 References 59

Chapter 3 Estimation of Free Gas Saturation and Porosity by Joint Bayesian Inversion of P- and S- Wave Attenuation 62

3.1 Abstract 62
3.2 Introduction 63
3.3 Data 67

3.3.1 Geological setting 67
3.3.2 Measuring Attenuation 68
3.4 Methodology 71
3.4.1 Rock Physics Model 72
3.4.2 Sensitivity Analysis 75
3.4.3 Markov-Chain Monte Carlo Sampling 77
3.5 Result 79
3.6 Discussion 81
3.6.1 Ambiguity 81
3.6.2 Numerical Integration 82
3.6.3 Problem Determinability 84
3.7 Conclusion 85
3.8 Appendix 86
3.8.1 Quality Factor (Mavko et al., 2009) 86
3.8.2 Effective Medium Model 87
3.9 References 89

Chapter 4 Characterization of Gas-Charged Porous Media: A Joint Inversion of P/S- Wave Attenuation from Both OBS and Sonic Log Data 94

4.1 Abstract 94
4.2 Introduction 95
4.3 Methodology 100
4.3.1 Intrinsic Attenuation Models 102
4.3.2 Numerical Integration 109
4.4 Application: The Hydrate ridge, Oregon margin 111
4.5 Discussion 118
4.6 Conclusion 127
4.7 Reference 129

Chapter 5 Summary 134

LIST OF FIGURES

Figure 1-1. Seismic velocity and attenuation are coupled as functions of frequency. The frequency range of conventional measurements are indicated. (Batzle et al., 2005)..... 17

Figure 1-2 Schematic diagram of attenuation inversion..... 19

Figure 2-1 Schematic diagram for the spectral ratio method 31

Figure 2-2 Schematic diagram of the centroid frequency shift method 32

Figure 2-3 Schematic diagram of the peak frequency shift method..... 33

Figure 2-4. Definition of effective frequency bandwidth..... 37

Figure 2-5. Schematic diagram of technique I..... 38

Figure 2-6. Schematic diagram of technique II 38

Figure 2-7. Schematic diagram of technique III..... 39

Figure 2-8. Schematic diagram of technique IV..... 40

Figure 2-9. Schematic diagram of technique V 40

Figure 2-10. A 2D wedge model used in this study. The minimum thickness is 0 at Trace 1 and the maximum thickness is 2.5 times of the signal period (T) at trace number 100. The S/Ns are -1 (a), 5 (b), 10 (c) 30 (d), ∞ (e), respectively. The solid blue line indicates the picked signal for the first interface, while the red one represents the picked signal for the second interface. The width of each interface is 1.8 times of the signal period. The white dashed lines indicate the trace numbers corresponding to one-way traveltime of 0.25T, 1T, 1.8T, 2.5T, respectively. 42

Figure 2-11. a. The last trace of wedge model with different S/Ns; b. the spectrum of first and second arrivals for S/N = ∞ and their centroid frequencies. 43

Figure 2-12. Estimated $\hat{Q}$ from the wedge model varying with different traces. The true Q is set as 200 as the dashed line. The smaller trace number means less traveltime, thus more strong interference of wavelets. The wavelet interference which occurs before trace number about 70 between first and second interfaces impairs the Q estimation. ... 45

Figure 2-13. a. Estimation errors with window size under the condition of f_p = 50 Hz, Q = 200, S/N = ∞; b. beginning trace of noninterference zone with window size. The larger trace number means the noninterference zone starts at a thicker layer. In other words, larger trace number corresponds to lower vertical estimation resolution. 46

Figure 2-14. a. Estimation errors with different Q models; and b. boxplot of the MAPEs for different Q models under f_p = 50 Hz and S/N = ∞ for the noninterference zone

(trace number from 70 to 100). The MAPEs are averaged over all frequency-bandwidth coefficients for the noninterference zone. 47

Figure 2-15. Estimation failure rates of the different *Q* models averaging traces of all frequency-bandwidth coefficients under f_p = 50 Hz and S/N = ∞ for the noninterference zone (trace number from 70 to 100). 48

Figure 2-16. Estimation errors with different bandwidth coefficients under f_p = 50 Hz and S/N = ∞. The MAPEs are averaged over all *Q* models for the noninterference zone (trace number from 70 to 100). 49

Figure 2-17. a. Estimation failure rates of the different bandwidth coefficients averaging all *Q* models; and b. boxplot of the MAPEs for different bandwidth coefficients under f_p = 50 Hz and S/N = ∞. The MAPEs are averaged over all *Q* models for the noninterference zone (trace number from 70 to 100). 49

Figure 2-18. Estimation errors for methods/techniques averaging over all *Q* models and bandwidth coefficients for the noninterference zone (trace number from 70 to 100). 51

Figure 2-19. a. Boxplot of the MAPEs for methods/techniques; b. estimation failure rates of methods/techniques averaging all *Q* models and bandwidth coefficients. Both are condition of f_p = 50 Hz and S/N = ∞ for the noninterference zone (trace number from 70 to 100). 51

Figure 2-20. a. Estimation errors with different S/Ns under f_p = 50 Hz. The MAPEs are averaged over all *Q* models and bandwidth coefficients for the noninterference zone (trace number from 70 to 100); b. estimation failure rates for different methods and techniques with different S/Ns under f_p = 50 Hz. The percentages of null values are averaged over all *Q* models and bandwidth coefficients for the noninterference zone. .. 52

Figure 2-21. a. Boxplot of the MAPEs under f_p = 50 Hz for the noninterference zone (trace number from 70 to 100); b. estimation failure rates with different S/Ns. The percentages of null values are averaged over all *Q* models and bandwidth coefficients for the noninterference zone. 53

Figure 2-22. Estimation errors for methods/techniques averaging over all *Q* models and bandwidth coefficients for the noninterference zone (trace number from 70 to 100, f_p = 50 Hz). 53

Figure 2-23. a. Estimation errors with different S/Ns under f_p = 1500 Hz. The MAPEs are averaged over all *Q* models and bandwidth coefficients for the noninterference zone (trace number from 70 to 100); b. estimation failure rates for different methods and techniques with different S/Ns under f_p = 1500 Hz. The percentages of null values are averaged over all *Q* models and bandwidth coefficients for the noninterference zone. .. 54

Figure 2-24. a. Boxplot of the MAPEs under f_p = 1500 Hz for the noninterference zone (trace number from 70 to 100); b. estimation failure rates with different. The percentages of null values are averaged over all *Q* models and bandwidth coefficients for the noninterference zone. 54

Figure 2-25. Estimation errors for methods/techniques averaging over all Q models and bandwidth coefficients for the noninterference zone (trace number from 70 to 100, f_p = 1500 Hz). 55

Figure 2-26. a. Boxplot of the MAPEs for methods/techniques under f_p = 50 Hz and S/N = ∞ for the interference zone (trace number from 60 to 65); b. estimation failure rates for different methods and techniques under f_p = 50 Hz. The percentages of null values are averaged over all Q models and bandwidth coefficients for the interference zone. .. 56

Figure 2-27. Estimation error for methods/techniques averaging over all Q models and bandwidth coefficients for the interference zone (trace number from 60 to 65, f_p = 50 Hz). 56

Figure 3-1. OBS survey in Finneidfjord, Norway. The gray star indicates the OBS; Black curves represent shots by the shipboard boomer. The white circle is the traces selected for Q estimation. The potential free gas area is shown as the hatched polygon. 68

Figure 3-2. R and T components (bottom) of OBS data after component rotation of X and Y components (top). The waveform energy is converted from X and Y components to R component. Only 70 traces showed, totally 556 traces. "Layer 1" is of interest, where the gas reservoir was discovered (Morgan et al., 2012; Vardy 2015). 69

Figure 3-3. Q_p (gray box) and Q_s (white box) estimated from Finneidfjord, Norway by centroid frequency shift method with technique I (Lei and Morgan, 2016). If taking the median, the quality factor of the first layer is Q_p = 26.0, Q_s = 30.5; the quality factor of second layer is Q_p = 48.0, Q_s = 22.0. 70

Figure 3-4. Sensitivity indices for Dvorkin-Mavko Model: a. $\log(Q_p^{-1})$; b. $\log(Q_s^{-1})$. Main and total effects are two different kinds of indices representing the extent of parameter sensitivities to the DM model. 76

Figure 3-5. Pseudocode for DE-MCMC (Brooks et al., 2011)..... 78

Figure 3-6. The performance of DE-MCMC on the joint Q_p and Q_s inversion for Fineidfjord OBS data. a) estimated gas saturation and porosity distributions; b) evolution of the chain during MCMC sampling; c) crossplot of estimated porosity and gas saturation with their posterior probability (color). The average acceptance rate of MCMC is 43%. 80

Figure 3-7. Numerical test for Dvorkin-Mavko model. 82

Figure 3-8. Schematic diagram of ambiguity caused by nonlinearity. 82

Figure 3-9. The joint probability-density distribution of porosity and water saturation. Colors represent the probability of a) prior, b) likelihood, c) posterior. The posterior is equal to the likelihood times prior. 83

Figure 3-10. Marginal distribution of gas (a) saturation and (b) porosity 83

Figure 3-11. Schematic diagram for Q_p, Q_s in different frequencies. The four dimensions of information would be obtained from seismic data and log data. 84

Figure 4-1. a. Sensitivity analysis for Dvorkin-Mavko velocity model, parameter ranges as Table 4-2; b. comparison of the relationship of $Q-S_g$ and Velocity$-S_g$. Both are under the condition of Hydrate Ridge, Oregon margin 97

Figure 4-2. The flowchart of the attenuation inversion 100

Figure 4-3. Schematic diagram of three patchy saturation models. a: White's Spherical model; b: White's Layered model; c: Dvorkin-Mavko model. 104

Figure 4-4. Geological setting of the Hydrate Ridge, offshore Oregon Margin. The shots (black dots, interval is about 40 m) and OBSs (black stars) were deployed. The ODP wells crossing the survey lines are shown as white triangles. 112

Figure 4-5. OBS data, H component, line NS1, station 01, Cruise TN112, Hydrate Ridge. The traces whose CMP's correspond to the well locations are as the dashed lines. 113

Figure 4-6. One trace of the sonic log, representing one depth. The receiver 1 is closest to source and receiver 8 is furthest to the source. The blue diamond area picks the compressional wave which is faster than the shear wave that is selected by red diamond area. The time window for diamonds is 2.5 ms. 114

Figure 4-7. Q estimation from Oregon Margin OBS data and from ODP sonic log data, a. well 1244; b. well 1245..... 114

Figure 4-8. Sensitivity indices for Dvorkin-Mavko model: a. $\log(Q_p^{-1})$; b. $\log(Q_s^{-1})$. Main and total effects are two different kinds of indices representing the extent of parameter sensitivities to the DM model. 116

Figure 4-9. Numerical integration results: marginal distribution of the likelihood of the well 1244 117

Figure 4-10. Numerical integration results: marginal distribution of the likelihood of the well 1245..... 117

Figure 4-11. Sensitivity indices for White's spherical model: a. $\log(Q_p^{-1})$; b. $\log(Q_s^{-1})$. Main and total effects are two different kinds of indices representing the extent of parameter sensitivities to the WS model..... 119

Figure 4-12. Sensitivity indices for White's layered model: a. $\log(Q_p^{-1})$; b. $\log(Q_s^{-1})$. Main and total effects are two different kinds of indices representing the extent of parameter sensitivities to the WL model 120

Figure 4-13. Numerical integration results: marginal distribution of the likelihood of the well 1244, White's layered model 122

Figure 4-14. Numerical integration results: marginal distribution of the likelihood of the well 1245, White's layered model 123

Figure 4-15. Numerical integration results: marginal distribution of the likelihood of the well 1244, White's spherical model 123

Figure 4-16. Numerical integration results: marginal distribution of the likelihood of the well 1245, White's spherical model 124

Figure 4-17. MCMC results: marginal distribution of the likelihood of the well 1244, Dvorkin-Mavko model 125

Figure 4-18. MCMC results: marginal distribution of the likelihood of the well 1245, Dvorkin-Mavko model 125

LIST OF TABLES

Table 2-1. Cases analyzed 41

Table 2-2 Frequency shift (Hz) for different models at different source frequencies. 48

Table 3-1. Initial Parameter Values and Bounds, Finneidfjord, Norway 77

Table 4-1. Mean of *Q* estimated from seismic and sonic log data, Hydrate Ridge, Oregon Margin..... 114

Table 4-2. Initial values and bounds for each parameter..... 116

Table 4-3. Best estimation ($\pm 2\sigma$) of the numerical integration 118

Table 4-4. Best estimation ($\pm 2\sigma$) of the MCMC scheme 126

ACKNOWLEDGEMENTS

"Learning is endless", said Chuang Tzu, an influential Chinese philosopher. Looking back, I would say the path leading to the doctoral degree is the most challenging but enjoyable one so far. The challenging part is what the Ph.D. is. However, thanks to the many helps I got from a lot of people, it also has enjoyable part. There are an enormous number of valued people who have made a difference in my life. Forgive me I cannot list them all.

Firstly, sincere thanks to my advisor Dr. Eugene Morgan who paved the way for my study. It is my honor to have the opportunity working with him for a while of my life. His guidance helped me in all the time of research and writing of this thesis. I could not have imagined having a better advisor and mentor for my Ph.D. study. Without his help, I would not have completed. His patience, support, guidance and encouragement throughout the study were greatly appreciated.

Besides my advisor, I would like to thank the rest of my thesis committee: Dr. Derek Elsworth, Dr. Hamid Emami-Meybodi, Dr. Sridhar Anandakrishnan, and Dr. Tieyuan Zhu, for their insightful comments and encouragement, but also for the hard questions which incented me to widen my research from various perspectives.

I would also extend my thanks to the professors at Penn State University who taught me in the past four years. The courses they offered broadened my horizon and involved me with a new discipline–Petroleum Engineering. They are: Professor Turgay Ertekin, Professor Luis F. Ayala H., Professor Zuleima T. Karpyn, Professor Randy L. Vander Wal, Professor Shimin Liu, Professor Chunshan Song, and Professor Mort D. Webster.

Last but not least, I would like to thank my family: my father, Jinquan Lei, who is always my role model and moral supporter of my life; my mother, Xifeng Xiong, who is hard-working and diligent family supporter; and my sister, Ying Lei, who is also my best friend. Without their support, I would not go that far.

Chapter 1 **Introduction**

Seismic reservoir characterization benefits integrated exploration and reservoir studies by providing information on the reservoir's internal architecture and properties. Geophysicists are able to utilize the reservoir properties to constrain physical models for prediction of the seismic response or re-explore the deeper and riskier resources. From a petroleum engineering perspective, it is an essential part of the development of a reservoir model. Reservoir engineers can make drilling decisions, reduce production risks, assess reserves or predict the remaining resources with the optimal knowledge of reservoir properties. In particular, volumetric reservoir calculations are preliminarily realized by characterizing water saturation and porosity; and the flow performance in dynamic reservoir simulation is based on the comprehensive understanding of, at least, the saturation, porosity, fluid viscosity, and permeability.

Approaches to estimate rock properties have already been widely proposed since last century. Saturation, porosity, and permeability can all be extracted from various wireline well log data. Perhaps most notably, Archie's Law (Archie, 1942, 1947, 1950; Rider, 1986; Peters, 2012; Tiab and Donaldson, 2012) provided a relationship between electrical conductivity/resistivity porosity and brine saturation, and porosity is also provided by density, sonic, and neutron logs (Peters, 2012; Tiab and Donaldson, 2012). Additionally, empirical correlations between porosity and permeability were proposed to estimate rock permeability (Kozeny, 1927; Berg, 1970; Nelson, 1994). More recently, Lee (2004) estimated gas concentration from compressional and shear sonic log by Biot theory (Biot, 1956a; Gassmann, 1951). However, estimates from well logs are restricted spatially to the near-wellbore volume.

Seismic survey data can serve as a useful tool to detect those properties by attribute extraction over wide areas. For example, Lu and McMechan (2002, 2004) inverted the free gas

saturation from seismic impedance; Santoso et al. (1995) calculateed the reservoir porosity by seismic AVO (Amplitude Variation with Offset) inversion; seismic velocity and amplitude are capable of estimating pore pressure (Bowers, 1995; Kvam, 2005); Dadashpour et al. (2007, 2009) predicted porosity and permeability from 4D seismic amplitudes. Summarily, the attributes commonly used to estimate rock properties either from log or seismic data are velocity, resistivity, density, amplitude or impedance. However, seismic attenuation is also, or even more strongly, related to the hydraulic properties of a formation. Biot (1956) first established an analytical relation between porous rock properties and seismic attenuation. More seismic attenuation models dealing with partial saturation have been proposed after that, which examine different geometries of gas inclusion (e.g., White, 1975; White et al., 1975; Dvorkin and Mavko, 2006).

Attenuation refers to the exponential decay of wave amplitude with distance. It is caused by energy-conserved factor (scattering and geometric dispersion), and inelastic dissipation (intrinsic attenuation) where energy is converted into heat. The intrinsic attenuation is frequency dependent. The intrinsic Q is of particular interest to exploration geophysics, because it is important to be considered in wave propagation forward models (such as is done in Zhu and Carcione, 2014); in inverse Q filtering; as a hydrocarbon indicator (Klimentos, 1995; Zhao et al., 2004); as an improvement to full waveform inversion (Barnes et al., 2014); and, as focused on in this research, as a predictor of formation properties.

Many models quantitatively describe the intrinsic attenuation. The earliest and most significant one is the wave-induced-fluid flow model for fluid saturated rocks (Biot, 1956a, b; Stoll and Bryan, 1970), in which seismic waves induce fluid flow in saturated rocks due to fluid-pressure equilibration between the peaks and troughs of a compressional wave or due to grain accelerations in the case of a shear wave, accompanied by internal friction until the pore pressure is equilibrated. Pride et al. (2004) complemented Biot's model at mesoscopic scales. Another notable model

captures the attenuation resulting from "squirt" flow (Mavko and Nur, 1979; O'Connell and Budiansky, 1974). For partially saturated liquid-gas systems, when a seismic wave compresses a rock, the grain contact area is deformed to a much greater extent than the intergranular pores, resulting in local pressure gradients, fluid movement, and viscous dissipation— or "squirt" flow. Dvorkin and Nur (1993) offered a model to treat both Biot and "squirt" flow mechanisms as coupled processes and relates P-wave velocity and attenuation to macroscopic parameters. Additional models include: White's spherical model (White, 1975), which quantifies the attenuation of viscous energy losses due to the seismic wave deforming a gas bubble surrounded by a shell of water; White's layered model (White et al., 1975), which considers a thick section of a rock composed of periodically alternating sub-layers of two different fluids (e.g, gas and water); and Walsh (1966) proposed another kind of model based on the friction dissipation when crack surfaces slide against one another when acted on by a seismic wave.

Compared with velocity, rock property inversion from seismic attenuation has more merits. Ecker et al. (2000) and Zillmer (2006) found that P-wave velocity variation is way too sensitive to gas saturation at low levels of gas concentration, such that reasonable error in velocity measurements translates to excessive error in saturation estimates. This is generally not the case for P-wave attenuation, which shows a more reasonable response to gas saturation over a wider range of saturation values (Morgan et al., 2012). Additionally, attenuation responses much more strongly to the change of effective pressure or differential pressure (defined as overburden pressure minus pore pressure) than velocities (Prasad and Manghnani, 1997). Furthermore, within the seismic frequency range, the dispersion effect, which for velocity is an issue when processing seismic data, is negligible for attenuation (Batzle et al., 2005).

Seismic attenuation inversion, as a powerful tool to provide us reservoir characteristics, has been researched recently. Singleton and Images (2007) utilized Q_p and Q_s to complement

impedance inversion. Raji and Rietbrock (2012) inverted the saturation from a theoretical attenuation-saturation curves but had to treat each case individually with the precondition of various rock properties. Morgan et al. (2012) inverted gas saturation and pore pressure by P-wave attenuation using a genetic algorithm.

In this thesis, we aim to improve upon these recent studies by inverting for more hydraulic properties with fewer known preconditions, since the exact information about the rock properties is difficult to know in many instances. In the first part (Chapter 2), we specifically discuss the common attenuation measurements, including centroid frequency shift method (CFS), spectral ratio method (SRM), and peak frequency method (PFS), aiming at making recommendations on optimal approaches to measure Q. This preliminary chapter is important, as accurate inversion results in later chapters depend on accurate measurements of Q from the field data. In Chapter 3, we propose a joint Q_p and Q_s inversion. Compared to Q_p inversion alone (Morgan et al., 2012), one more dimension of information is added, increasing constraints on the model to suppress the ambiguity in the solution set, and allowing us to estimate one more parameter (porosity) simultaneously. The joint workflow is validated by running on an OBS dataset from Finneidfjord, Norway, where free gas collection in the shallow offshore sediments has documented in previous field data collection efforts. In Chapter 4, we integrate sonic log data with seismic data to realize a more advanced joint inversion, which utilizes four data inputs (four independent Q measurements: Q_p and Q_s from OBS surveys and Q_p and Q_s from sonic logs). In this step, we implement the advanced workflow on Hydrate Ridge, Oregon margin, where free gas has been identified beneath the gas hydrate. Instead of using Markov-Chain Monte Carlo to sample the solution space (joint posteriors), we directly calculate the four marginal distributions of the joint posterior via numerical integration, which is less efficient but more precise.

1.1 Literature Review

In this chapter, I discuss important previous studies related to seismic investigation of gas reservoirs. The first five sections, I review the common reservoir properties, including gas saturation, porosity, permeability and their measurements. Next, I also reviewed the multicomponent seismic data which is the foundation of this research. In the seventh section, quality factor measurements in temporal and spectral domains are reviewed. The eighth section contains various rock physics models to simulate the seismic attenuation. They are chronologically reviewed. At the end, some main stochastic optimization algorithms including simulated annealing, genetic algorithm, and Bayesian algorithm are reviewed.

1.1.1 Gas Saturation

The gas saturation is the fraction of the pore space occupied by gas. Most gas reservoirs also contain some connate (non-movable) water, also known as irreducible water saturation. Gas saturation is used directly in the calculation of reserves and in the calculation of total compressibility.

Current methods to estimate gas saturation from seismic survey have been widely proposed. Holbrook et al. (1996) identified drastic decrease of P-wave velocity for gas bearing sediments in VSP data. Lee (2004) estimated gas concentration from P- and S- wave velocities of well logs by Biot-Gassmann theory (Biot, 1956a; Gassmann, 1951) and found that $Vp/Vs < 2$ could indicate gas. However, because the P-wave velocity depends highly on how the gas is distributed in the pore space, the amount of gas estimated from the P-wave velocity remains high uncertainty. In 2009, further work has been done by Lee and Collett. They concluded that Vp/Vs did not work for gas saturation less than 40%. Moreover, because of the P-wave velocity dispersion, the P-wave

attenuation exists for gas charged sediments within seismic frequency range, instead of the sonic log frequency range. Lu and McMechan (2002) combined two Archie's equations and an indirect empirical formula to obtain the gas concentration from acoustic impedance of single channel seismic data. Later on, they did further research on the same calibration on inverted impedance of a nearby multichannel seismic line to estimate free gas saturation in 2004. Tinivella and Accaino (2000) used a theoretical model to quantify the amount of free gas. The estimation was realized by comparing the interpreted velocity anomalies, which resulted from the analysis of theoretical velocity curves or tomography analysis of OBS data, to the reference velocity curves. At the same time, Tinivella and Lodolo did further work on multi-channel seismic data. But it was just an unreliable approximation of free gas saturation, since compressional velocity is very sensitive to even small amount of free gas in sediments. And it is sensitive to free gas distribution in pore spaces (Domenico, 1977). Bünz et al. (2005) inverted gas concentration from the analyzed velocity of ocean bottom cable (OBC) data through Tinivella (1999) weighted-equation approach and Helgerrud's effective medium model (Helgerud et al., 1999; Ecker et al., 2000). Because of the high uncertainty of velocity and the idealized assumption of patchy gas distribution, the application of this model is limited.

1.1.2 Porosity

Porosity defined as fractional pore space in rock frame, including effective and absolute porosity. The latter counts on both the pores connected with each other and ones not connected with each other. The effective porosity, which is more significant to reservoir characterization, controls fluid storage in aquifers, oil and gas fields. And it can be used to calculate bulk moduli of saturated rock (Gassmann, 1951; Zimmerman et al., 1986; Mavko and Mukerji, 1995). There are a variety of methods quantifying porosity. Manger (1963) listed the techniques by which the porosity

was determined. For downhole petrophysical analysis, porosity was related to conductivity/resistivity and brine saturation by Archie's Law (Archie 1942, 1947, 1950; Rider, 1986; Peters 2012; Tiab and Donaldson 2012). Density sonic or neuron logs can also be used to estimate porosity. For seismic survey, Angeleri and Carpi (1982) calculated reservoir porosity from a pseudo-velocity logs which was inverted from seismic data. In 1987, Doyen used a geostatistical technique to estimate porosity in a numerically simulated reservoir model. Santoso et al. (1995) and Berryman et al. (2000) inverted porosity from seismic attributes by AVO inversion techniques. In 2004, Soubotcheva and Stewart examined the prediction of density porosity logs from seismic attributes using neural networks.

1.1.3 Permeability

Rock permeability is one important flow parameter associated with surface production and injection, defined as how easily a fluid can pass through the rock. Mapping the permeability is an important step for performance-estimation studies. Typically core and well log data can lead to accurate estimation of permeability. Nelson (1994) summarized the empirical permeability-porosity relationships in sedimentary rocks, realizing the estimation of rock permeability from the porosity. The NMR technology which was used for a better estimation of pore space characteristics was applied to measure permeability correlations (Quintero et al., 1999). On the other hand, seismic data also contains permeability information. Pride et al. (2003) discussed the potential to invert permeability from seismic attenuation. Dadashpour et al. (2007, 2009) predicted porosity and permeability from 4D seismic amplitudes based on Gauss-Newton optimization technique.

1.1.4 Other Properties

Pore Pressure

The pore pressure is defined as the pressure of fluids within the pores of a reservoir, usually hydrostatic pressure, or the pressure exerted by a column of water from the formation's depth to sea level. As an indispensable parameter in decline curve analysis, it plays an essential role in reservoir production simulation. Lots of methods also have been proposed to estimate it. Eaton (1975), Foster and Whalen (1966) and Hottmann and Johnson (1965) suggested some empirical equations to determine the laterally changed geo-pressure (often used to describe abnormally high pore fluid pressures) from resistivity or sonic logs. Nevertheless, their failing to take into account the overpressure (defined as the pore fluid pressure in excess of the hydrostatic pressure) leads to a significant error. In 1995, Bowers calculated the effective pressure from the velocity that could be from sonic logs or seismic data considering both under-compaction and fluid expansion mechanisms. Kvam (2005) utilized an amplitude-based approach to estimate the pore pressure. The velocity related to pore pressure was derived from seismic amplitude and had higher temporal resolution than velocities from traveltimes which are commonly used in velocity analysis. And in 2002, Prasad experimentally found V_p/V_s would be used to quantify the effective pressure. However, the validation run is based on ultrasonic data without considering the velocity dispersion effect.

Lithology

Lithology means "the composition or type of rock such as sandstone or limestone" (Hynes, 1991). The formation properties vary with different lithologies, even for rock that holds the same hydrocarbon or water. Understanding the lithology is the foundation from which all other

petrophysical calculations are made. Since it is not always easy to obtain the physical rock sample, some indirect determinations were proposed. Rock typing usually can be carried out by looking up the commercial catalogs of analog data (Thomas et al., 1995). Additionally, acoustic logs are also a common way to identify lithologies. Burke et al. (1969) determined formation lithology of hydrocarbon by crossplot of neutron and density, called M-N plot. But the imaginary M and N values are physically meaningless. And M-N plot is subject to certain ambiguities. In order to counteract these drawbacks, Clavier and Rust (1976) derived a Matrix Identification Plot to identify lithologies. Moreover, seismic data was also utilized in lithology determination. In 2010, Özdemir et al. used density and shear modulus from multicomponent seismic data inversion to successfully indicate lithology. Avseth and Rmstad (2011) conducted a Bayesian inversion on seismic data, well observations, and prior information to predict lithology or fluid classes with associated uncertainties.

Clay content

Clay minerals are composed of layered alumina and silicate molecules (Brindley and Brown, 1980). Clay content generally impairs the permeability and porosity of the pores. The montmorillonite, one of its compositions, often leads to very significant effects on measurements of porosity, saturation and seismic attenuation (Leurer, 1997). The water is often expelled from the shale beds into surrounding permeable beds under the circumstance of overburden stress and, consequently, pore fluid pressure increasing. If the clay-mineral-expelled water cannot escape from the permeable bed, the risk of drilling hazards will be enhanced due to the overpressure.

1.1.6 Multicomponent Seismic Data

Both the compressional and shear wave are important in characterizing the gas reserves. They are sensitive to the type of pore fluid within rocks in either velocity field or attenuation field. This part is reviewing the multicomponent seismic acquisition which motivated the application of P- and S- wave integration in gas characterization.

In 1920, vibrations were first introduced as interpretable information for oil reserves. Ever since then, geophysicists put great efforts on understanding and improving the seismic data acquisition techniques, which helped to discover giant oil fields in many basins in the world. The acquisition technology evolved from two to three dimensions and later to four dimensions. In order to solve the great exploration challenges such as geological formations near salt domes, subsalt formations, tight sands, and source rocks, one single component (P wave) seismic data is not enough. In turn, multicomponent seismology could provide more information of the formations, better characterizing the subsurface. The benefit of multicomponent seismology is to acquire the shear wave by recording the horizontally propagating waves. There is a variety of multicomponent seismology geometries in industry such as 3C/2D, 3C/3D, 3C/4D, 4C/2D, 4C/3D, 4C/4D and 9C3D (3-component shear source recorded by 3-component sensor). In addition to the conventional coil geophones as standard sensors, special multicomponent sensors have been developed to record more motions for land and marine seismic. Current marine multicomponent acquisition system uses 4C sensors with traditional air-gun sources which generate pressure wave. The 3C receivers are placed on the sea floor to record 3-D seismic waves. The fourth component is a hydrophone recording the pressure.

1.1.7 Quality Factor Measurement

The purpose of this section is to give a brief and comprehensive overview of the major advances in estimating *Q*. Chapter 4 elaborates on the precise methodology of the most widely-accepted techniques.

Currently, varieties of approaches have been proposed to estimate *Q* from the seismic transmission data such as VSP (e.g., Hauge, 1985), and crosswell (e.g., Quan and Harris, 1997; Neep et al., 1996); or seismic reflection data such as a single stacked common-depth-point (CDP) reflection data (e.g., Jannsen et al., 1985; Tonn, 1991), and common midpoint (CMP) gather data (e.g., Dasgupta and Clark, 1998; Hackert and Parra, 2004) in either the time domain or frequency domain. For time domain methods, the simplest but crudest one is the amplitude decay method, which originates from quality factor definition but requires true amplitude recordings. In 1974, Gladwin and Stacey put forward that the quality factor could be determined by risetime, which was defined as time from the intersection of the steepest rise of a wavelet to its peak wavelet amplitude. It was an empirical formula, which had already been demonstrated by Kjartansson (1979), but invalid to secondary arrivals. Different from the former simple methods, wavelet modeling approach (Jannsen et al., 1985) estimated *Q* by iteratively matching the synthetic signal with the reference. But the interference of noise, spherical spreading and scattering would fail this method. In 1996, Engelhard derived an expression of *Q* in terms of instantaneous amplitude and frequency, known as analytical signal method. It removed the geometrical spreading from intrinsic attenuation, but accurate synchronization was hard to achieve. The more accurate time-domain method is matching filter method (Cheng and Margrave, 2013), more sophisticated than wavelet-modeling method. Also, it was a time-domain alternative to spectrum modeling methods (Jannsen et al., 1985; Tonn, 1991; Blias, 2011) and very robust to denoise for reflection data.

For spectral domain, Bath (1974) and Hauge (1985) estimated *Q* from the logarithm ratio of amplitude spectrum, called spectral ratio method (SRM), in which the frequency-independent noise would never intervene in the estimation. In 1984, when matching idea was applied to different stages of SRM, a matching-technique method was proposed by Raikes and White (1984). Pinson et al., (2008) found that the SRM performs better when applied to many seismic traces and combined with robust linear regression. Tu and Lu (2010) improved SRM with effective bandwidth coefficient. More than that, Jannsen et al. (1985) and Tonn (1991) researched on spectrum modeling method in additional to the time-domain wavelet modeling method. It performed better than SRM due to no assumption for reflection coefficient and phase velocity. Moreover, Quan and Harris in 1997 presented a more efficient method, which statistically estimated *Q* from the centroid frequency shift. The latest method is peak frequency shift method (PFS) by Zhang and Ulrych, (2002), which estimated *Q* from peak frequency shift instead of centroid frequency shift. Notably, Zhu and Harris (2015) presented a joint inversion strategy for estimating attenuation along with P-wave velocity, where they coupled the centroid frequency shift technique with a velocity traveltime tomography model.

1.1.8 Rock Physics Model for Seismic Attenuation

As mentioned in Chapter 1, the intrinsic *Q* plays a key role in reservoir geophysics, including application in wave propagation forward modeling (such as is done in Zhu and Carcione, 2014), inverse *Q* filter, gas detection (Klimentos, 1995; Zhao et al., 2004), full waveform inversion (Barnes et al., 2014), and hydraulic property estimation. So far, there are many rock physics models which are able to quantitatively describe the intrinsic *Q*. Biot (1956) derived theoretical formulas for compressional and shear velocity limits for saturated rock at very low and very high frequencies. In Biot's theory, the energy loss is caused by internal friction when seismic waves-induce fluid

flows due to pore pressure disequilibrium. Walsh (1966) proposed a model as one source of attenuation based on the friction dissipation when crack surfaces in the contact slide relative to one another during passage of a seismic wave. Berryman (1980) experimentally analyzed and confirmed the validation of the Biot's formulas. The complete frequency dependent expression of V_p and V_s was further derived by Stoll (1977). However, Biot's model can be only used for fully saturated rocks. In 1975, White modeled the seismic effects of partially saturated rocks. He proposed formulas for complex bulk modulus as a function of angular frequency under the assumption that the two kinds of fluid were separated into two concentric spheres (patches). Besides, Dutta and Ode (1979) obtained more rigorous solutions for the same patchy geometry by considering the difference between the dry-frame properties of two patches. White et al. (1975) also proposed a layered model, considering a thick section of rocks composed by alternating thin layers of the porous rock, saturated with fluid. Another kind of attenuation mechanism— "squirt" flow, was proposed by Mavko and Nur (1979). In "squirt" flow theory, when a seismic wave compresses a rock with partially liquid-gas saturation, the grain contact area is deformed to a much greater extent than the intergranular pores, resulting in local pressure gradients, fluid movement, and viscous dissipation. Dvorkin and Nur (1993) offered a model to treat both Biot and "squirt" flow mechanisms as coupled processes and related P velocity and attenuation to macroscopic parameters. Leurer (1997) treated the grain material as two phases, called "effective grain model (EGM)"—silicate layers as elastic part and intracrystalline water between silicate layers as fluid part. Thus, the wave-energy consuming resulted from squirt-flow from the inclusions to the pore space. Further on, in 2008, Leurer and Brown modified the effective grain model with introducing viscoelasticity of granular material, instead of elastic spheres in EGM. Pride et al. (2004) complemented Biot's model at mesoscopic scales. Carcione and Picotti (2006) applied the White's model to different mesoscopic scales for heterogeneous rocks. Dvorkin and Mavko (2006) considered a patchy model of which two kinds of fluid were separately distributed into two patches

without mutual interaction. The moduli at high frequency is estimated by Hill average (Hill, 1963) of those two patches.

1.1.9 Stochastic Optimization Algorithm

Because of the mathematical complexity of the rock physics models, stochastic optimization algorithms are well-suited for the inversion of these models. Here, I review some of the major advances in such techniques. Stochastic optimization algorithms have been growing rapidly in popularity over the last century. Since Metropolis et al. (1953) and Hastings (1970) put forward modified forms for Markov Chain Monte Carlo (MCMC) over configuration space, a lot of stochastic optimization algorithms based on this powerful sampling approach have been proposed. Kirkpatrick et al. (1983) presented a discrete optimization method generated from the idea of Metropolis-Hastings MCMC (Metropolis et al., 1953; Hastings, 1970), called simulated annealing (SA). SA is a stochastic local search technique that mimics the heating and cooling system. Compared to SA, genetic algorithm (GA) (Holland, 1975), a more robust approach, has to make a variety of choices about how to execute the algorithm, making it more effective and efficient. While SA creates a new solution by modifying only one solution with a local move, GA also creates solutions by combining two different solutions, called crossover. Besides, in 1997, 1989, and 1990, Glover suggested a Tabu search to look for the optimal solution of cost function. Tabu search is a higher-level heuristic procedure for solving optimization problems, which imposing constraints to avoid the trap of local optima. In 2003, Higdon et al. discussed variety of Bayesian schemes in solving the inverse problem, including single-site Metropolis Updates, multivariate updating scheme, Differential-Evolution MCMC, and delayed acceptance Metropolis algorithms. The basic idea of Bayesian inference is to fit a probability model, also known as

posterior, to a set of data and summarizing the result by a probability distribution of the model. It is powerful in inversion when getting the accurate posterior distribution.

1.2 Statement of the Problem

The methods for gas saturation estimation reviewed are all velocity related, which is either from sonic log data or inverted from single or multi-channel seismic data, OBS, or OBC data. However, velocity information might not be always a good choice for gas saturation estimation. Domenico (1977) experimentally demonstrated that in a small gas concentration the compressional wave reflection amplitude cannot be an accurate indicator for gas saturation, since it is too sensitive to gas content and changes nonlinearly with gas saturation; Ecker et al. (2000) found out that at low levels of gas concentration the saturation estimation was extremely sensitive to interval velocity values. In addition, Zillmer (2006) concluded that the accuracy of gas quantification enormously depended on the certainties of seismic velocities. Besides, for consolidated sandstone, Wyllie et al. (1958) experimentally analyzed the impact of the gas saturation on velocities at a relative high gas concentration condition. It was, nevertheless, concluded that the gas saturation variation leads to a very small change in velocity under a given differential pressure. Moreover, CO_2 saturation insensitively responds to P-wave velocity at high gas saturation in theoretical studies (Carcione et al., 2006), laboratory experiments (Lei and Xue, 2009) and field studies (Chadwick et al., 2005; Daley et al., 2011; Zhu and Sun, 2017). So, the velocity is either too sensitive to gas saturation at low levels of saturation or not sensitive to gas saturation at high levels of saturation (Figure 4-1b). Additionally, compressional velocity was found to be independent of permeability anisotropy (Gelinsky and Shapiro, 1994; Saleh et al., 2009) and relationships between seismic velocity and permeability is difficult to establish. Summarily, velocity might not be a good indicator of gas concentration.

Whereas, seismic attenuation may be better for gas saturation estimation than the velocity. Firstly, the attenuation has a much stronger relationship with gas saturation. When the compressional wave passes through a partially saturated porous medium, the differential pressure

between water and gas is generated due to the compressibility of gas. This differential pressure results in fluid flow, which brings energy loss due to friction among water, gas and rock grains (Müller et al., 2010). Additionally, besides porosity, permeability and characteristic size are also sensitive parameters to the attenuation rock physics model other than the velocity model (Figure 3-4, Figure 4-1). Furthermore, the velocity dispersion cannot be negligible for a medium with quality factor $Q < 30$ within the seismic frequency range (Molyneux and Schmitt, 1999). However, the conventional impedance inversion assumes the velocity is frequency-independent. At this situation, the accuracy of estimation of gas saturation from seismic velocity is not assured due to the frequency dependency. Q, nevertheless, better fits the frequency-independency assumption within seismic frequency band (Figure 1-1).

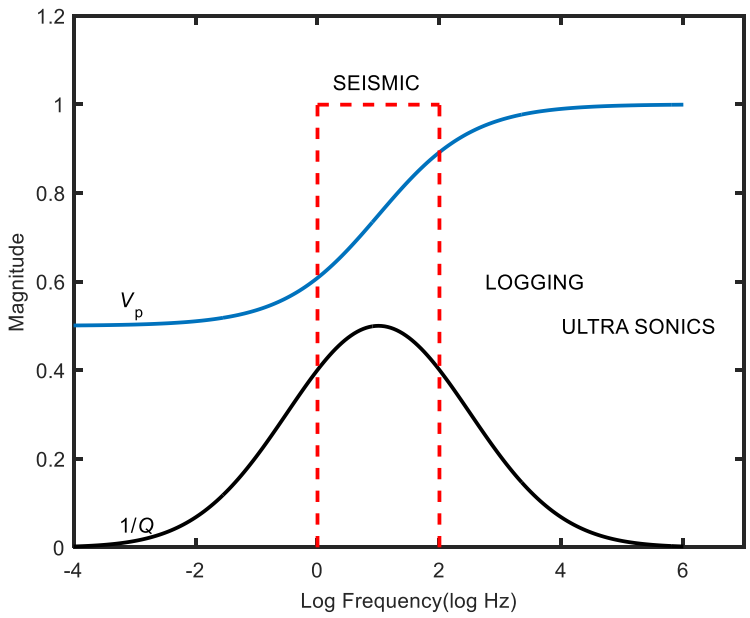

Figure 1-1. Seismic velocity and attenuation are coupled as functions of frequency. The frequency range of conventional measurements are indicated. (Batzle et al., 2005)

Considering those drawbacks of velocity-related methods, when it comes to either estimation of gas saturation or porosity, the seismic attenuation might be a better choice to quantitatively link to target hydraulic properties (White, 1975; White et al., 1975), especially for

cases with small gas concentration. Notably White (1975) built a rock physics model of P-wave attenuation based on Biot theory. Raji (2013) theoretically analyzed the quantitative relationship between the seismic attenuation and gas saturation by the standard linear solid model (Zener and Siegel, 1949), but his estimation had to be treated individually for different rock properties under different conditions; also, the measurement of quality factor should be challenging for practical application; and effective pressure, which has an effect on seismic attenuation, was not taken into consideration. Morgan et al. (2012) inverted the model of Carcione and Picotti (2006), which is a modification of White's model for periodic layered media, with a genetic algorithm to obtain the estimate of gas saturation. This is a stochastic inversion method which can robustly invert different parameters from seismic attenuation under proper constraints based on geological priors. However, only P-wave information was used in his paper; the Q estimation by spectral ratio method was not validated to be assured accurately working for the subsequent inversion; and there is still room to improve the accuracy of the estimation. The following research is an improvement on Morgan et al. (2012).

In this dissertation, the first part is dedicated to Q measurements. The accuracy of this inversion strategy depends on the reliable estimation of attenuation from the seismic data. As discussed in the Literature Review, many competing methods exist for estimating attenuation. However, there is little discussion on which method works best under different circumstances. We systematically compare three commonly used Q measurements and propose guidelines about the preprocessing techniques on data or parameter choices when estimating Q for readers. Secondly, the joint Q_p and Q_s inversion is implemented on OBS (ocean bottom seismometer) data at Finneidfjord, Norway, where sub-seabed free gas has been observed. The basic strategy to solve the whole problem is as Figure 1-2. The Dvorkin-Mavko attenuation model is used to forward model the P- and S- wave quality factors. Next, these modeled values are compared against the measured field values in a Bayesian likelihood function, and a Markov Chain Monte Carlo

algorithm is utilized for inversion of reservoir properties from measured Q values. Lastly, we propose an even more advanced inversion workflow to integrate Q_p, Q_s of seismic data with Q_p, Q_s of sonic log data and verify it on the datasets from Hydrate Ridge, Oregon margin.

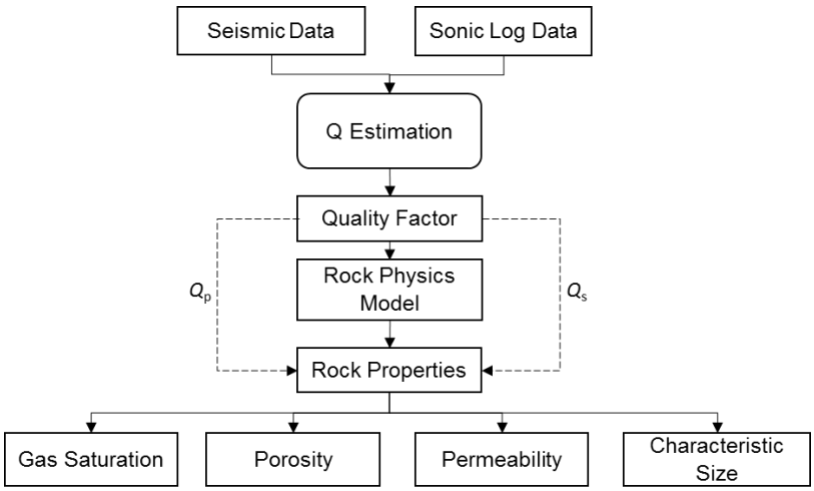

Figure 1-2 Schematic diagram of attenuation inversion

1.3 Novelties of This Thesis

The novelties of this research are:

a) systematically investigate the performance of various methods of Q estimation, provide a detailed procedure including best option to preprocess data and the optimal parameter choice under difference conditions for Q estimation especially when dealing with reflected seismic data.;

b) combine the seismic Q_p and Q_s in the attenuation inversion to reduce the ambiguity of inversion and provide an efficient strategy to simultaneously invert porosity and gas saturation by a stochastic algorithm, prove the feasibility of attenuation-based inversion and demonstrate its benefits compared to velocity-based inversion;

c) further integrate the seismic data with sonic log datasets to realize an advanced and robust four-parameter inversion workflow, offering the values and uncertainties of gas saturation, porosity, permeability, and characteristic size which is poorly determined but a very important parameter in rock physics.

Summarily, the attenuation inversion is meaningful in industrial practice. It reliably quantifies some useful rock properties, which could be used in such as reservoir simulation, volumetric gas reservoir calculation, decline curve analysis, drilling hazard monitoring, etc. In addition to the hydraulic property estimation, the findings of Q estimation would help improve the wave propagation forward modeling, inverse Q filter, gas detection, full waveform inversion, hydromechanical modeling, etc.

1.4 Reference

Angeleri, G.P., Carpi, R., 1982. Porosity prediction from seismic data. Geophys. Prosp. 30, 580–607. doi:10.1111/j.1365-2478.1982.tb01328.x

Archie, G.E., 1950. Introduction to petrophysics of reservoir rocks. Am. Assoc. Pet. Geol. Bull. 34, 943–961.

Archie, G.E., 1947. Electrical resistivity an aid in core-analysis interpretation. Am. Assoc. Pet. Geol. Bull. 31, 350–366.

Archie, G.E., 1942. The Electrical Resistivity Log as an Aid in Determining Some Reservoir Characteristics. Soc. Pet. Eng. 146. doi:10.2118/942054-G

Barnes, C., Cergy-pontoise, U. De, Charara, M., Williamson, P., 2014. P & S wave attenuation effects on full-waveform inversion for marine seismic data 949–953.

Bath, M., 1974. Spectral Analysis in Geophysics. Dev. Solid Earth Geophys. 7, 563.

Batzle, M., Hofmann, R., Prasad, M., Duranti, L., Han, D., 2005. Seismic Attenuation: Observations and Mechanisms, in: SEG/Houston 2005 Annual Meeting. pp. 2003–2006.

Berg, R.R., 1970. Method for Determining Permeability from Reservoir Rock Properties. Gulf Coast Assoc. Geol. Soc. Trans. 20, 303–317.

Berryman, Berge, Bonner, 2000. Transformation of seismic velocity data to extract porosity and saturation values for rocks. J. Acoust. Soc. Am. 107, 3018–27.

Berryman, J.G., 1980. Confirmation of Biot's theory. Appl. Phys. Lett. 37, 382. doi:10.1063/1.91951

Biot, M.A., 1956a. Theory of Propagation of Elastic Waves in a Fluid‐Saturated Porous Solid. II. Higher Frequency Range. J. Acoust. Soc. Am. 28, 168‐178. doi:10.1121/1.1908241

Biot, M.A., 1956b. Theory of Propagation of Elastic Waves in a Fluid-Saturated Porous Solid. I. Lower Frequency Range. J. Acoust. Soc. Am. doi:10.1121/1.1908241

Blias, E., 2011. Q‐factor estimation through optimization approach to near‐offset VSP data. SEG Tech. Progr. Expand. Abstr. 2011 4278‐4282. doi:10.1190/1.3628100

Bowers, G.L., 1995. Pore Pressure Estimation From Velocity Data: Accounting for Overpressure Mechanisms Besides Undercompaction, in: SPE Drilling & Completion. pp. 89–95.

Brindley, G., Brown, G.W., 1980. Crystal Structures of Clay Minerals and their X-Ray Identification. Mineralogical Society of Great Britain and Ireland.

Bünz, S., Mienert, J., Vanneste, M., Andreassen, K.K.A., Stefan, B., 2005. Gas hydrates at the Storegga Slide: Constraints from an analysis of multicomponent, wide-angle seismic data. Geophysics 70, B19. doi:10.1190/1.2073887

Burke, J.A., Campell, R.L., Schmidt, A.W., 1969. The Litho-porosity cross plot. SPWLA TENTH Annu. LOGGING Symp.

Carcione, J.M., Picotti, S., 2006. P-wave seismic attenuation by slow-wave diffusion: Effects of inhomogeneous rock properties. Geophysics 71, 01–08.

Carcione, J.M., Picotti, S., Gei, D., Rossi, G., 2006. Physics and Seismic Modeling for Monitoring

CO2 Storage. Pure Appl. Geophys. 163, 175–207. doi:10.1007/s00024-005-0002-1

Chadwick, R.A., Arts, R., Eiken, O., 2005. 4D seismic quantification of a growing CO2 plume at Sleipner, North Sea, in: Petroleum Geology: North-West Europe and Global Perspectives – Proceedings of the 6th Petroleum Geology Conference. Geological Society of London, pp. 1385–1399. doi:10.1144/0061385

Cheng, P., Margrave, G.F., 2013. Estimation of Q : a comparison of different computational methods. CSPG/CSEG/CWLS GeoConvention 12, 2–5.

Clavier, C., Rust, D.H., 1976. MID plot: a new lithology technique. Log Anal.

Dadashpour, M., Echeverría-Ciaurri, D., Kleppe, J., Landrø, M., 2009. Porosity and permeability estimation by integration of production and time-lapse near and far offset seismic data. J. Geophys. Eng. 6, 325–344. doi:10.1088/1742-2132/6/4/001

Dadashpour, M., Kleppe, J., Landrø, M., 2007. SPE 104519 Porosity and Permeability Estimation by Gradient-Based History Matching using Time- Lapse Seismic Data.

Daley, T.M., Ajo-Franklin, J.B., Doughty, C., 2011. Constraining the reservoir model of an injected CO2 plume with crosswell CASSM at the Frio-II brine pilot. Int. J. Greenh. Gas Control 5, 1022–1030. doi:10.1016/J.IJGGC.2011.03.002

Dasgupta, R., Clark, R.A., 1998. Estimation of Q from surface seismic reflection data. Geophysics 63, 2120. doi:10.1190/1.1444505

Domenico, S.N., 1977. ELASTIC PROPERTIES OF UNCONSOLIDATED POROUS SAND RESERVOIRS. Geophysics 42, 1339–1368.

Doyen, P.M., 1988. Porosity from seismic data: A geostatistical approach. Geophysics 53, 1263–1275. doi:10.1190/1.1442404

Dvorkin, J., Mavko, G., 2006. Modeling attenuation in reservoir and nonreservoir rock. Lead. Edge 25, 194. doi:10.1190/1.2172312

Dvorkin, J., Nur, A., 1993. Dynamic poroelasticity: A unified model with the squirt and the Biot mechanisms. Geophysics 58, 524. doi:10.1190/1.1443435

Eaton, B.A., 1975. The Equation for Geopressure Prediction from Well Logs, in: Fall Meeting of the Society of Petroleum Engineering of AIME. Society of Petroleum Engineers. doi:10.2118/5544-MS

Ecker, C., Dvorkin, J., Nur, A.M., 2000. Estimating the amount of gas hydrate and free gas from marine seismic data. Geophysics 65, 565. doi:10.1190/1.1444752

Engelhard, L., 1996. Determination of Seismic-Wave Attenuation By Complex Trace Analysis. Geophys. J. Int. 125, 608–622. doi:10.1111/j.1365-246X.1996.tb00023.x

Foster, J.B., Whalen, H.E., 1966. Estimation of formation pressures from electrical surveys - Offshore Louisiana. J. Pet. Technol. 18, 165–171.

Gassmann, F., 1951. Über die Elastizität poröser Medien, Vier. Der Natur.

Gelinsky, S., Shapiro, S.A., 1994. Poroelastic velocity and attenuation in media with anisotropic permeability, in: SEG Technical Program Expanded Abstracts 1994. Society of Exploration Geophysicists, pp. 818–821. doi:10.1190/1.1932010

Gladwin, M.T., Stacey, F.D., 1974. Anelastic Degradation of Acoustic Pulses in Rock. Phys. Earth

Planet. Inter. 8, 332–336. doi:10.1016/0031-9201(76)90068-6

Glover, F., 1990. Tabu Search—Part II. ORSA J. Comput. 2, 4–32. doi:10.1287/ijoc.2.1.4

Glover, F., 1989. Tabu Search—Part I. ORSA J. Comput. 1, 190–206. doi:10.1287/ijoc.1.3.190

Glover, F., Laguna, M., 1997. Tabu Search. Kluwer Academic Publishers, Norwell, MA, USA.

Hackert, C.L., Parra, J.O., 2004. Improving Q estimates from seismic reflection data using well-log-based localized spectral correction. Geophysics 69, 1521. doi:10.1190/1.1836825

Hastings, W.K., 1970. Monte Carlo sampling methods using Markov chains and their applications. Biometrika 57, 97–109.

Hauge, P.S., 1981. Measurements of attenuation from vertical seismic profiles. Geophysics 46, 1548–1558. doi:10.1190/1.1441972

Helgerud, M.B., Dvorkin, J., Nur, a., Sakai, a., Collett, T., 1999. Elastic - wave velocity in marine sediments with gas hydrates: Effective medium modeling. Geophys. Res. Lett. 26, 2021. doi:10.1029/1999GL900421

Higdon, D., Lee, H., Holloman, C., 2003. Markov chain Monte Carlo-based approaches for inference in computationally intensive inverse problems, in: Bayesian Statistics 7: Proceedings of the Seventh Valencia International Meeting. pp. 181–198.

Hill, R., 1963. Elastic properties of reinforced solids: Some theoretical principles. J. Mech. Phys. Solids 11, 357–372. doi:http://dx.doi.org/10.1016/0022-5096(63)90036-X

Holbrook, W.S., Hoskins, H., Wood, W.T., Stephen, R. a, Lizarralde, D., 1996. Methane Hydrate and Free Gas on the Blake Ridge from Vertical Seismic Profiling. Science (80-.). 273, 1840–1843. doi:10.1126/science.273.5283.1840

Holland, J.H., 1975. Adaptation in Natural and Artificial Systems. MIT Press, Cambridge, MA, USA.

Hottmann, C.E., Johnson, R.K., 1965. Estimation of Formation Pressures from Log-Derived Shale Properties. J. Pet. Technol. 17. doi:10.2118/1110-PA

Hynes, N.J., 1991. Dictionary of Petroleum Exploration. Drilling, and Production, Tulsa, Oklahoma.

Jannsen, D., Voss, J., Theilen, F., 1985. Comparison of methods to determine Q in shallow marine sediments from vertical reflection seismograms. Geophys. Prospect. 479–497.

Kirkpatrick, S., Gelatt, C.D., Vecchi, M.P., 1983. Optimization by Simulated Annealing. Sci. 220, 671–680. doi:10.1126/science.220.4598.671

Kjartansson, E., 1979. Constant Q-Wave Propagation and Attenuation. J. Geophys. Res. 84, 4737–4748.

Klimentos, T., 1995. Attenuation of P- and S- waves as a method of distinguish gas and condensate from oil and water. Geophysics 60, 447–458.

Kozeny, J., 1927. Über kapillare Leitung des Wassers im Boden 136, 271–306.

Kvam, O., 2005. Pore pressure estimation from single and repeated seismic data sets.

Lee, M.W., 2004. Elastic velocities of partially gas-saturated unconsolidated sediments. Mar. Pet. Geol. 21, 641–650. doi:10.1016/j.marpetgeo.2003.12.004

Lee, M.W., Collett, T.S., 2009. Unique problems associated with seismic analysis of partially gas-saturated unconsolidated sediments. Mar. Pet. Geol. 26, 775–781. doi:10.1016/j.marpetgeo.2008.07.009

Lei, X., Xue, Z., 2009. Ultrasonic velocity and attenuation during CO2 injection into water-saturated porous sandstone: Measurements using difference seismic tomography. Phys. Earth Planet. Inter. 176, 224–234. doi:10.1016/j.pepi.2009.06.001

Leurer, K.C., 1997. Attenuation in fine-grained marine sediments: Extension of the Biot-Stoll model by the "effective grain model" (EGM). Geophysics 62, 1465. doi:10.1190/1.1444250

Leurer, K.C., Brown, C., 2008. Acoustics of marine sediment under compaction: binary grain-size model and viscoelastic extension of Biot's theory. J. Acoust. Soc. Am. 123, 1941–51. doi:10.1121/1.2871839

Lu, S., McMechan, G. a., 2002. Estimation of gas hydrate and free gas saturation, concentration, and distribution from seismic data. Geophysics 67, 582. doi:10.1190/1.1468619

Lu, S.M., McMechan, G.A., 2004. Elastic impedance inversion of multichannel seismic data from unconsolidated sediments containing gas hydrate and free gas. Geophysics 69, 164–179. doi:10.1190/1.1649385

Manger, E.G., 1963. Porosity and Bulk Density of Sedimentary Rocks. Geol. Survery Bull. 1144-E 62.

Mavko, G., Mukerji, T., 1995. Seismic pore space compressibility and Gassmann's relation. Geophysics 60, 1743–1749.

Mavko, G., Nur, A., 1979. Wave attenuation in partially saturated rocks. Geophysics 44, 161–178.

Metropolis, N., Rosenbluth, A.W., Rosenbluth, M.N., Teller, A.H., Teller, E., 1953. Equation of State Calculations by Fast Computing Machines. J. Chem. Phys. 21, 1087–1092. doi:doi:10.1063/1.1699114

Molyneux, J.B., Schmitt, D.R., 1999. First‐break timing: Arrival onset times by direct correlation. Geophysics 64, 1492–1501. doi:10.1190/1.1444653

Morgan, E.C., Vanneste, M., Lecomte, I., Baise, L.G., Longva, O., McAdoo, B., 2012. Estimation of free gas saturation from seismic reflection surveys by the genetic algorithm inversion of a P-wave attenuation model. Geophysics 77, R175. doi:10.1190/geo2011-0291.1

Müller, T.M., Gurevich, B., Lebedev, M., 2010. Seismic wave attenuation and dispersion resulting from wave-induced flow in porous rocks — A review. Geophysics 75, 75A147. doi:10.1190/1.3463417

Neep, J.P., Sams, M.S., Worthington, M.H., O'Hara-Dhand, K.A., 1996. Measurement of seismic attenuation from high-resolution crosshole data. Geophysics 61, 1175–1188. doi:10.1190/1.1444037

Nelson, P., 1994. Permeability-porosity relationships in sedimentary rocks. Log Anal.

O'Connell, R.J., Budiansky, B., 1974. Seismic velocities in dry and saturated cracked solids. J. Geophys. Res. 79, 5412–5426. doi:10.1029/JB079i035p05412

Özdemir, H., Flanagan, K., Tyler, E., 2010. Lithology and hydrocarbon mapping from multicomponent seismic data. Geophys. Prospect. 58, 297–306. doi:10.1111/j.1365-2478.2009.00821.x

Peters, E.J., 2012. Advanced Petrophysics: Geology, porosity, absolute permeability, heterogeneity, and geostatistics, Advanced Petrophysics. Live Oak Book Company.

Petro-elastic and lithology-fluid inversion from seismic data – state-of-the-art and new opportunities Per Avseth (NTNU / Odin Petroleum) and Kjartan Rimstad (NTNU) Summary During the last couple of decades , there have been great advances in seismic , n.d. 23–26.

Pinson, L.J.W.W., Henstock, T.J., Dix, J.K., Bull, J.M., 2008. Estimating quality factor and mean grain size of sediments from high-resolution marine seismic data. Geophysics 73, G19–G28. doi:10.1190/1.2937171

Prasad, M., 2002. Acoustic measurements in unconsolidated sands at low effective pressure and overpressure detection. Geophysics 67, 405. doi:10.1190/1.1468600

Prasad, M., Manghnani, M.H., 1997. Effects of Pore and differential pressure on compressional wave velocity and quality factor in Berea and Michigan sandstones. Geophysics 62, 1163–1176.

Pride, S.R., Berryman, J.G., Harris, J.M., 2004. Seismic attenuation due to wave-induced flow. J. Geophys. Res. 109, 1–19. doi:10.1029/2003JB002639

Pride, S.R., Harris, J.M., Johnson, D.L., Mateeva, A., Nihel, K.T., Nowack, R.L., Rector, J.W., Spetzler, H., Wu, R., Yamomoto, T., Berryman, J.G., Fehler, M., 2003. Permeability dependence of seismic amplitudes. Lead. Edge 22, 518–525. doi:10.1190/1.1587671

Quan, Y., Harris, M.J., 1997. Seismic attenuation tomography using the frequency shift method. Geophysics 62, 895. doi:10.1190/1.1444197

Quintero, L., Boyd, a., Gyllensten, a., El-Wazeer, F., 1999. Comparison of Permeability from NMR and Production Analysis in Carbonate Reservoirs. Proc. SPE Annu. Tech. Conf. Exhib. doi:10.2523/56798-MS

Raikes, S.A., White, R.E., 1984. Measurements of Earth Attenuation from Downhole and Surface Seismic Recordings. Geophys. Prospect. 32, 892–919.

Raji, W.O., 2013. The use of seismic attenuation to indicate saturation in hydrocarbon reservoirs : Theoretical study and modelling approach 4, 45–53.

Raji, W.O., Rietbrock, a., 2012. The use of seismic attenuation for monitoring saturation in hydrocarbon reservoirs. SEG Tech. Progr. Expand. Abstr. 2012 1–6. doi:10.1190/segam2012-0309.1

Rider, M.H., 1986. The geological interpretation of well logs. Blackie.

Saleh, M., Vega, S., Prasad, M., Sharma, R., 2009. A study of permeability and velocity anisotropy in carbonates, in: SEG Technical Program Expanded Abstracts 2009. Society of Exploration Geophysicists, pp. 4238–4242. doi:10.1190/1.3255766

Santoso, D., Alam, S., Hendraya, L., Alfian., Sulistiyono., Munadi, S., 1995. Estimation of limestone reservoir porosity by seismic attribute and AVO analysis. 11th Geophys. Conf. 26, 437–443. doi:10.1071/EG995437

Singleton, S., Images, R.S., 2007. The use of Seismic Attenuation and Simultaneous Impedance Inversion in Geophysical Reservoir Characterization SEG / San Antonio 2007 Annual Meeting SEG / San Antonio 2007 Annual Meeting 1422–1426.

Soubotcheva, N., Stewart, R.R., 2004. Predicting porosity logs from seismic attributes using geostatistics 16, 1–14.

Stoll, R.D., 1977. Acoustic Waves in Ocean Sediments. Geophysics 42, 715. doi:10.1190/1.1440741

Stoll, R.D., Bryan, G.M., 1970. Wave Attenuation in Saturated Sediments. J. Acoust. Soc. Am. 47.

Thomas, E.C., Sneider, J.W., Neasham, Vinegar, H.J., 1995. A Catalog of Petrophysical and Geological Properties of Typical Reservoir Rocks. Shell Oil Co., Houston.

Tiab, D., Donaldson, E.C., 2012. Petrophysics : theory and practice of measuring reservoir rock and fluid transport properties. Gulf Professional Pub./Elsevier.

Tinivella, U., 1999. A method for estimating gas hydrate and free gas concentrations in marine sediments. Bolletino di Geofis. Teor. Ed Appl. 40, 19–30.

Tinivella, U., Accaino, F., 2000. Compressional velocity structure and Poisson's ratio in marine sediments with gas hydrate and free gas by inversion of reflected and refracted seismic data (South Shetland Islands, Antarctica). Mar. Geol. 164, 13–27. doi:10.1016/S0025-3227(99)00123-1

Tinivella, U., Lodolo, E., 2000. Blake Ridge Bottom-Simulating Reflector Transect: Tomographic Velocity Field and Theoretical Model To Estimate Methane, in: Proc. ODP, Scientific Results. pp. 273–281.

Tonn, R., 1991. the Determination O F the Seismic Quality Factor Q From Vsp Data: a Comparison of Different Computational Methods' R a I N E R T O N N 2. Geophys. Prospect. 39.

Tu, N., Lu, W., 2010. Improve Q estimates with spectrum correction based on seismic wavelet estimation. Appl. Geophys. 7, 217–228. doi:10.1007/s11770-010-0252-2

Walsh, J.B., 1966. Seismic Wave Attenuation in Rock Due to Frcition. J. Geophys. Res. 71, 2591–2599.

White, J.E., 1975. Computed Seismic Speeds and Attenuation in Rocks With Partial Gas Saturation. Geophysics 40, 224. doi:10.1190/1.1440520

White, J.E., Mihailova, N., Lyakhovitsky, F., 1975. Low‐frequency seismic waves in fluid‐saturated layered rocks. J. Acoust. Soc. Am. 57, S30–S30. doi:10.1121/1.1995164

Wyllie, M.R.J., R., G.A., Gardner, G.H.F., 1958. An Experimental Investigation of Factors Affecting Elastic Wave Velocities in Porous Media. Geophysics XXIII, 459–493.

Zener, C.M., Siegel, S., 1949. Elasticity and Anelasticity of Metals. J. Phys. Colloid Chem. 53, 1468. doi:10.1021/j150474a017

Zhang, C., Ulrych, T.J., 2002. Estimation of quality factors from CMP records. Geophysics 67, 1542. doi:10.1190/1.1512799

Zhao, W., Li, H., Yao, F., 2004. Attenuation Characterization of seismic waves in the wavelet domain and th detection of gas, in: SEG Int'l Exposition and 74th Annual Meeting, Denvor, Colorado. pp. 8–11.

Zhu, T., Carcione, J.M., 2014. Theory and modelling of constant-q p- and s-waves using fractional spatial derivatives. Geophys. J. Int. 196, 1787–1795. doi:10.1093/gji/ggt483

Zhu, T., Harris, J.M., 2015. Improved estimation of P-wave velocity, S-wave velocity, and

attenuation factor by iterative structural joint inversion of crosswell seismic data. J. Appl. Geophys. 123, 71–80. doi:10.1016/j.jappgeo.2015.09.005

Zhu, T., Sun, J., 2017. Viscoelastic reverse time migration with attenuation compensation. GEOPHYSICS 82, S61–S73. doi:10.1190/geo2016-0239.1

Zillmer, M., 2006. A method for determining gas-hydrate or free-gas saturation of porous media from seismic measurements. Geophysics 71, N21. doi:10.1190/1.2192910

Zimmerman, R.W., Somerton, W.H., King, M.S., 1986. Compressibility of porous rocks. J. Geophys. Res. Solid Earth 91, 12765–12777. doi:10.1029/JB091iB12p12765

Chapter 2 **A Comparison of Methods for Estimating *Q***

2.1 Abstract

As a quantitative measure of seismic attenuation, quality factor (*Q*) is useful to directly indicate hydrocarbon, assist inverse *Q* filtering, and forward model seismic wave propagation; however, quality factor remains difficult to reliably measure from seismic data. Many approaches in either the time or frequency domain have been proposed in the past. Among them, the most popular approaches are the spectral ratio method, centroid frequency shift method, and peak frequency shift method. They are the base of many newly proposed methods and a lot of case studies had implemented them to estimate *Q*, but no benchmarking of these methods currently exists giving an objective comparison of their performances. Furthermore, little guidance is given to the practitioner on how best to implement these methods, namely: is there a best way to utilize those methods in order to more accurately extract *Q*? In this paper, we performed a detailed analysis and comparison of those methods on synthetic seismic data with specified *Q* values. We applied the three methods under different preprocessing techniques, frequency bandwidths, signal frequencies, signal-to-noise ratios (S/N), and *Q* models. We find that *Q* is estimated most accurately under the following conditions: a) using the centroid frequency shift or spectral ratio methods after running FFT on windowed seismic amplitudes or running FFT on extracted wavelets; b) truncating the frequency bandwidth with coefficients between 0.2 ~ 0.4; c) data with higher frequency; d) data with less noise; and e) dealing with layers with lower *Q* (higher attenuation).

2.2 Introduction

In seismic interpretation, *Q* is an important geophysical attribute of the subsurface. It is associated with the intrinsic physical properties of rocks and fluids (Winkler and Nur, 1982; Sheriff and Geldart, 1995), as well as the scattering effect of the seismic wave (Goutbeek et al., 2004); thus, *Q* can be partitioned into two major factors: 1) intrinsically anelastic energy loss due to viscous effect of the pore fluids, shearing at grain boundaries, and mineral dislocations, and 2) scattering energy loss due to the spherical spreading of the wavefront and diffraction at heterogeneities (Hatzidimitriou 1994; Goutbeek et al., 2004; Müller et al., 2010). The difference between these two mechanisms lies in the factor that the energy of the former one is transferred into heat which is unconservative, while the later one mainly results from the geometrical energy redistribution (Gao et al., 1998; Hatzidimitriou, 1994). Since the intrinsic *Q*, due to the first mechanism, is related to the physical properties of rocks and fluids (Winkler & Nur, 1982; Sheriff and Geldart, 1995), it is a valuable diagnostic tool for reservoir characterization and hydrocarbon detection (Toksöz et al., 1979; Frisillo and Stewart, 1980). Additionally, the intrinsic *Q* is crucial to interpret the effect of AVO, improve the resolution of seismic imaging, and advance the study of material properties. However, intrinsic *Q* remains a difficult seismic attribute to measure from field data, and few guidelines exist that speak to the reliability of methods for estimating *Q*.

Currently, many methods exist to estimate quality factor from seismic transmission data such as VSP (e.g., Hauge 1981) and crosswell (e.g., Quan and Harris 1997; Neep et al., 1996), or seismic reflection data such as CDP gathers (e.g., Jannsen et al., 1985; Tonn, 1991) and CMP gathers (e.g., Dasgupta and Clark, 1998; Hackert and Parra, 2004). These methods operate in either the time domain or frequency domain. For time-domain approaches, the simplest one is the amplitude decay method, which is directly derived from the quality factor definition. It quantitively calculates the maximum amplitude reduction, thus has a high requirement of the amplitude

conservation. In 1974, Gladwin and Stacey put forward that the quality factor could be determined by risetime, defined as the time from the intersection of the steepest rise of a wavelet to its peak wavelet amplitude. This empirical method is insensitive against secondary arrivals. Kjartansson (1979) compensated for the lack of theoretical background of the risetime approach. The wavelet modeling method (Jannsen et al., 1985) is an optimization procedure that matches a reference signal with the observed signal. One main problem of this method is its low tolerance of the ambient noise, spherical spreading, or scattering effect. In 1996, Engelhard derived an expression for the seismic quality factor with instantaneous amplitude and frequency of seismic traces, known as the analytical signal method. It considers geometrical spreading, but time synchronization is a difficult issue to tackle. More recently, an accurate time-domain method was the matching filter method (Cheng and Margrave, 2013). It is a time-domain alternative to spectrum modeling methods (Jannsen et al., 1985; Tonn, 1991; Blias, 2011) and very robust to cope with noise on reflection data.

However, the frequency domain methods perform better than those in the time domain, mainly because Q factor almost exclusively has an effect on the shape of the spectrum while the seismic amplitude might be affected by many factors such as underground structure, geometric spreading, and automatic gain control. It is easier to separate the intrinsic attenuation from frequency-independent factors such as spherical spreading or reflectivity (Tu and Lu, 2010) in the spectral domain. For the purpose of the attenuation measurement, the process of wave propagation is assumed to be a linear system. If the spectrum of the seismic source wavelet is $S(f)$, the absorption response is $H(f)$, geometrical spreading and transmission responses are included in $G(f)$, and the received amplitude spectrum is $R(f)$. The spectral ratio method (SRM) (Bath, 1974; Hauge, 1981) obtains relatively accurate Q measurements from the logarithmic ratio of the amplitude spectra assuming that the spherical spreading and scattering is frequency-independent; thus, we have the following expression (Bath, 1974; Hauge, 1981)

$$H(f) = e^{-\frac{\pi f t}{Q}}, \quad (2-1)$$

$$ln\left(\frac{R(f)}{S(f)}\right) = -\frac{\pi t}{Q} f + lnG. \quad (2-2)$$

So, Q is related to the slope of a line fitted to the logarithmic ratio (as Figure **2-1**). This method has been commonly used in practice. Please note that the estimated Q is sensitive to spectral notching and the choice of the effective frequency bandwidth (Tu and Lu, 2010). Pinson et al. (2008) applied an interactively reweighted robust least-squares regression to suppress outliers caused by noise. However, how to choose a proper effective frequency bandwidth is essential and still needs further investigation.

In 1984, Raikes and White employed the idea of matching at different stages of estimation procedures and proposed a matching technique method. Its expression is almost the same as spectral ratio method except for an additional constant and ratio of a transfer function. Another spectral method is spectrum modeling method, which is a byproduct of the wavelet modeling method (Jannsen et al., 1985; Tonn, 1991) and a frequency-domain alternative to the matching filter method (Cheng and Margrave, 2013). It does not need the assumption that reflection coefficient and phase velocity are independent of frequency.

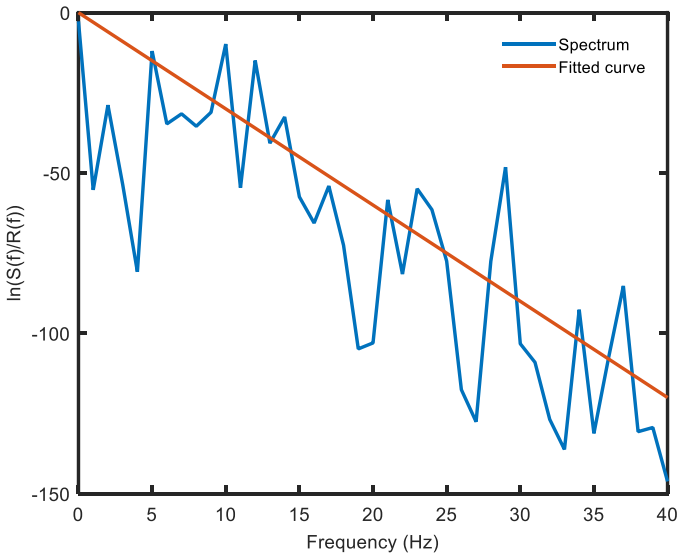

Figure 2-1 Schematic diagram for the spectral ratio method

Instead of using the spectral ratio, Quan and Harris (1997) presented a centroid frequency shift method (CFS) to estimate Q in heterogeneous media. As other spectral approaches, it has a strong capability of resisting frequency-independent noise. Quan and Harris (1997) proposed, if the incident spectrum $S(f)$ is Gaussian, and reflected spectrum is denoted by $R(f)$, the quality factor is as follows

$$Q = \frac{\pi(t_r - t_s)\sigma^2}{f_s - f_r} \tag{2-3}$$

where the centroid frequencies f_s, f_r and spectral variance σ^2 are defined by (as Figure **2-2**)

$$f_s = \frac{\int f|S(f)|df}{\int|S(f)|df}, \tag{2-4}$$

$$f_r = \frac{\int f|R(f)|df}{\int|R(f)|df}, \tag{2-5}$$

$$\sigma_s^2 = \frac{\int(f - f_s)^2|S(f)|df}{\int|S(f)|df}. \tag{2-6}$$

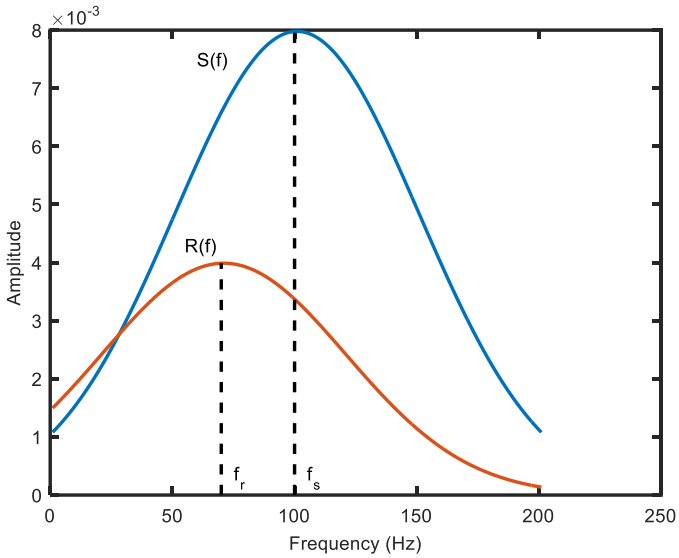

Figure 2-2 Schematic diagram of the centroid frequency shift method

The methods above are all for poststack or zero-offset data. For CMP gathers, Dasgupta and Clark (1998) proposed a *Q*-versus-offset (QVO) method. They applied the classical SRM trace by trace and took the average *Q*. Hackert and Parra (2004) improved the QVO method to remove

the tuning effect by using well-log-based localized spectral correction. One of the latest methods for CMP gathers is the peak frequency shift method (PFS) (Zhang and Ulrych, 2002). PFS calculates Q from the reduction of peak frequencies f_p at different offsets. Q is expressed in terms of the f_p of the reflection waveform and the dominant frequency f_m of the source wavelet that is assumed to be a Ricker wavelet (as Figure **2-3**).

$$Q = \frac{\pi t f_p f_m^2}{2\left(f_m^2 - f_p^2\right)}. \qquad (2-7)$$

This method is compatible with both CMP gathers and poststack data.

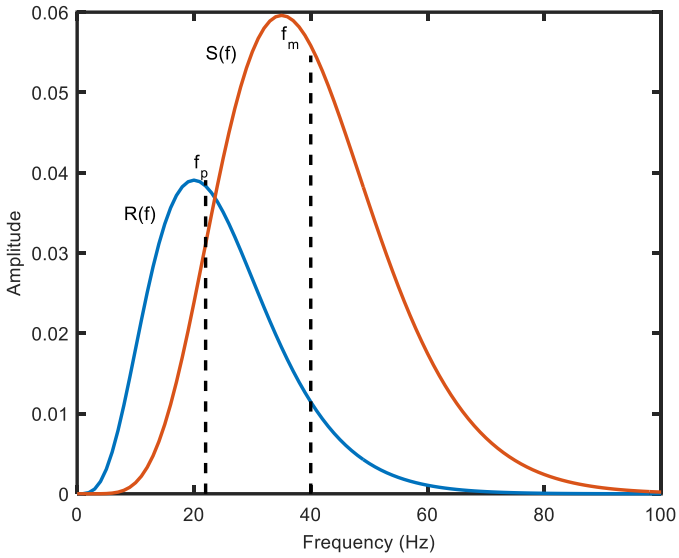

Figure 2-3 Schematic diagram of the peak frequency shift method

More advanced methods based on them are proposed afterwards. For example, CFS was initially developed to conduct the attenuation tomography in Quan and Harris's paper (1997). In 2016, Dutta and Schuster optimized the difference between the observed peak frequency shift and the predicted one to realize a wave-equation Q tomography. However, there are still risks of Q tomography, which lie in the error propagation from the velocity values to the Q values. The tomography technique heavily relies on the velocity model, most likely resulting in the slow or even no convergence problem for noise-rich data or data with a less accurate velocity model (Rossi

et al., 2007). Moreover, most of them are developed specially for earthquake records, of which the energy source or reference trace is easily set. Nevertheless, when it comes to engineering projects, the effective energy of the source is difficulty to determine. So, the spectral methods in estimating *Q* are so important as to be worthy of devoting efforts on analyzing or improving the current ones. The current spectral methods also have some limitations in practical applications. For instance, CFS has the assumption that attenuation is linearly proportional to the frequency, meaning the *Q* is independent of frequency; PFS assumes a Ricker wavelet as the source when deriving the *Q* estimation equations, which is hardly satisfied in practice. Moreover, most applications of attenuation estimation used cross-well data or head waves. But seismic reflection data is handier and more desired to be effectively used. Accurately estimating *Q* from reflection data necessitates some special data-preprocessing techniques which try to satisfy those assumptions before conducting estimation (Tu and Lu, 2010). However, the specific techniques to cope with the corresponding issues, comparison of the efficacy for different approaches, and a clear recommendation on which methods are the best to use under which circumstances are rarely saw. It is expected to have one which would facilitate the practical application of spectral methods or the advanced *Q* tomography.

In this paper, we are committed to compare popular intrinsic *Q* measurements, particularly focusing on the frequency-domain methods: spectral ratio method, centroid frequency shift method, and peak frequency shift method. These popular methods have shown greater success in the literature than other methods (e.g., Sams and Goldberg, 1990; Rickett, 2006; Tu and Lu, 2010; Tary et al., 2017; Oliveira et al., 2017; Zhang et al., 2016); however, we do not expect a method that would work perfectly under any condition (Tonn, 1991). Here, we focus on the investigation of the performance of those three popular methods, figuring out the proper one for a specific condition and suggesting optimal preprocessing techniques. In terms of extracting *Q* from reflection data, this paper discusses five data-preprocessing techniques that help to improve the quality of frequency-

domain data and conserve more useful information. Subsequently, we evaluate the performance of various combinations of techniques and methods using synthetic seismic reflection data. We also test them on models with different Q's, different S/Ns, different frequencies, and different effective frequency bandwidths (will be covered in the next section). The goal of this study is to comprehensively diagnose these methods under varieties of model conditions with various preprocessing techniques and to ultimately provide insights on the optimal choices of preprocessing techniques and estimation methods for a given model, deeply understanding the impact factors of Q measurements.

2.3 Methods

Different kinds of noise caused by the ambient condition, equipment, or personal error would distort the time or frequency characteristics of the signal, affecting the accuracy of *Q* estimation. The demand for noise suppression necessitates data preprocessing. The techniques such as time-frequency transformation, window functions, zero padding, and so forth would be discussed below. Meanwhile, excessive processing would cut down the reliability of estimation since the conservation of the useful information would also be impaired somehow by processing techniques. The degree of preprocessing, such as how much band-pass filter, what kind of window function, what kind of time-frequency decomposition techniques, or, especially, which effective frequency bandwidth (Figure **2-4**), is worth researching.

In particular, the frequency-based methods largely depend on the quality of the time-frequency decomposition. The conventional Fast Fourier Transform (FFT) suffers from the trade-off in time localization and spectral resolution, where a smaller window size will be more representative of the target interface, but its spectrum will be more band limited. Using a continuous wavelet transform (CWT) instead of FFT affords better time localization without the subjectivity of the window choice. However, this comes at the cost of subjectivity in the choice of mother wavelets to use as the basis of the transformation. One would want this mother wavelet to resemble the source wavelet. But in practice, the source wavelet may be unknown. In this section, we offered five candidate preprocessing workflows that focus on exploring the impact of CWT over FFT, as well as other techniques stated before.

2.3.1 Technique I

Firstly, in case of frequency leakage, the Hamming window is a good choice to taper the target signal for spectral transformation. It keeps the high level of frequency resolution and is easily

implemented (Harris, 1978). Then, the time series corresponding to each window is transformed into the frequency domain via FFT after zero-padding, which improves the spectral resolution. Sometimes, residual noise in signals would largely impair the spectra. In order to further mitigate the residual noise, a moving average filter is a common technique to smooth the spectra (Karl, 1989). A crucial factor impacting the accuracy of Q estimation is the effective frequency bandwidth, which suppresses the lower and higher frequency noise. Tu and Lu (2010) suggested determining the bandwidth by an effective-bandwidth coefficient ε (Figure **2-4**).

$$f_{eff} \in \{R(f) \geq \varepsilon \cdot max(|R(f)|)\} \qquad (2-8)$$

where $R(f)$ is the received wavelet spectrum. The effective bandwidth f_{eff} is defined as frequencies when the amplitudes are less than a threshold that is adjusted by ε. The smaller the coefficient, the wider the frequency bandwidth. Subsequently, both the effective received wavelet $R(f)$ and effective source wavelet $S(f)$ are determined by the newly defined bandwidth. At the end, the well-prepared data is used to measure the Q. These steps are displayed conceptually in Figure 2-5.

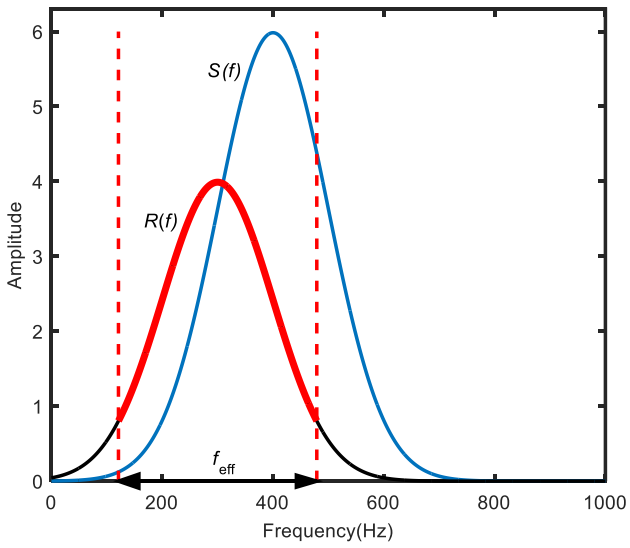

Figure 2-4. Definition of effective frequency bandwidth

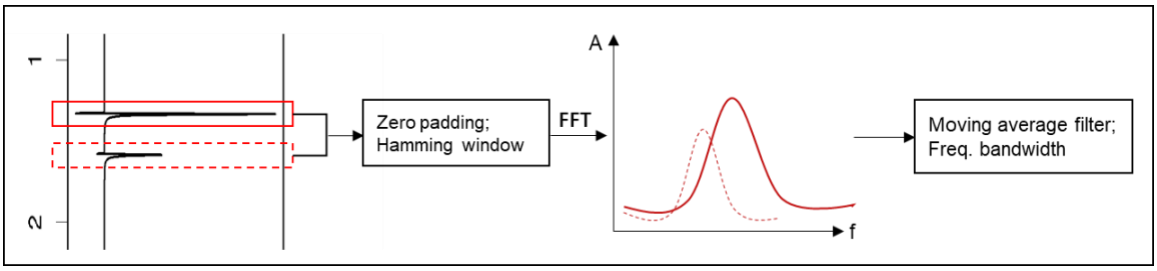

Figure 2-5. Schematic diagram of technique I

2.3.2 Technique II

The target reflection data is transformed into the time-frequency domain through the CWT with a Morlet mother wavelet, of which the central frequency f_c = 0.1 Hz and the standard deviation of its Gaussian envelope σ = 5 (Figure 2-6). Q would be estimated by methods discussed above based on the time slices of the scalogram for source and reflection interfaces. Again, the moving average filtering and the frequency bandwidth constraint are imposed on the spectrum before Q estimation.

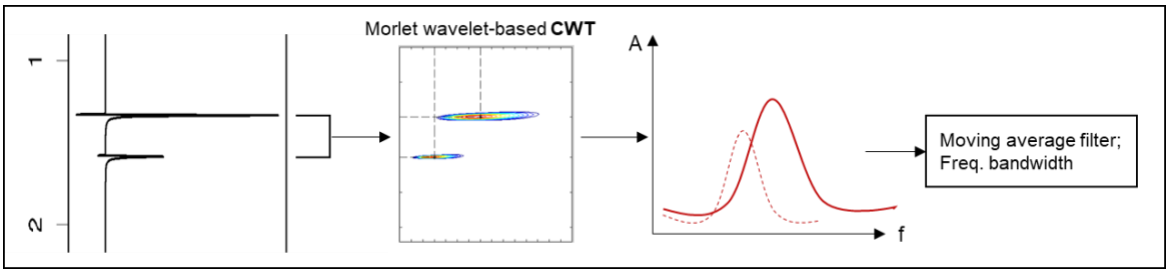

Figure 2-6. Schematic diagram of technique II

2.3.3 Technique III

Here, we apply the same steps to preprocess the data as in Technique II, except that the assumed Morlet wavelet is replaced by a statistically extracted wavelet. Specifically speaking, when analyzing the time-frequency spectrum via continuous wavelet transformation, the mother

wavelet is extracted by the technique of Lu et al. (2007) on the target windowed data, instead of the default Morlet wavelet (Figure 2-7). His method assumes the wavelet fourth-order moment is approximately equal to the fourth-order cumulant of the seismic data. Subsequently, the wavelet is iteratively solved by minimizing the cost function. Comparing Figure 2-6 and Figure 2-7, the operational difference between Techniques II and III lies in the mother wavelet choice.

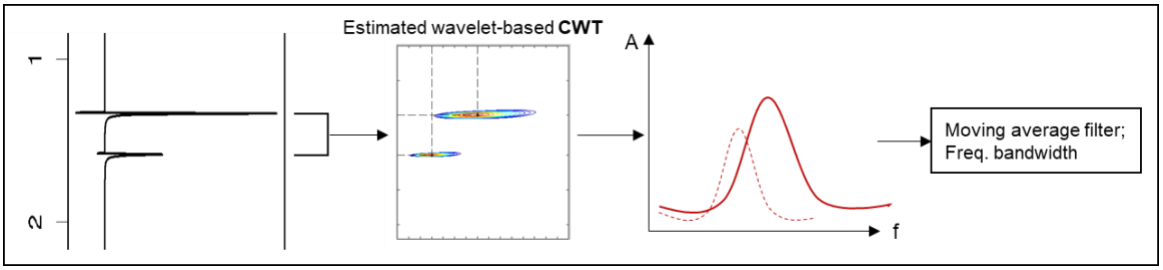

Figure 2-7. Schematic diagram of technique III

2.3.4 Technique IV

After denoising, here we estimate wavelets from both truncated source and reflection signals by Lu's method. Then, we conduct FFT to transform the estimated wavelets from the time domain to frequency domain. Before FFT, the Hamming window and zero padding technique are also implemented on the wavelet (Figure 2-8). Now, those two wavelets represent the source and reflected waves. Then the moving average filter smooths their spectra before *Q* estimation. This process is approximately identical to that proposed by Tu and Lu (2010), except that he used a reflectivity sequence to calibrate the spectrum.

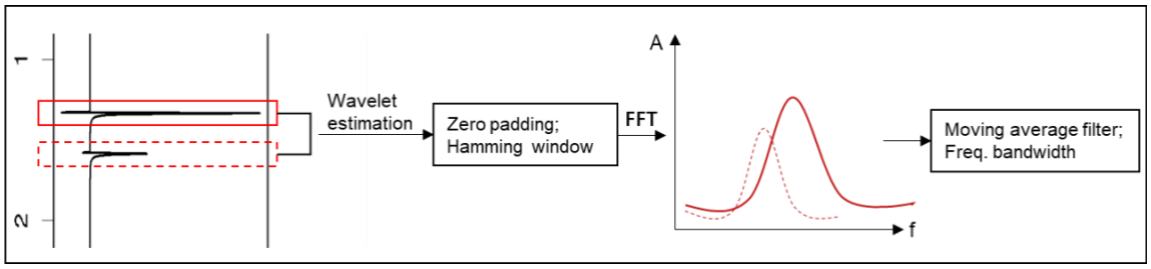

Figure 2-8. Schematic diagram of technique IV

2.3.5 Technique V

As illustrated in Figure 2-9, the last approach carries out the CWT with a Morlet mother wavelet on the new wavelets which are estimated by Lu's method from source and reflection signals, respectively. The parameters of Morlet mother wavelet are the same as that in Technique II. This differs from Technique II in that here the CWT is being performed on the extracted wavelets representing the source and reflected waves, instead of directly running CWT on the signals.

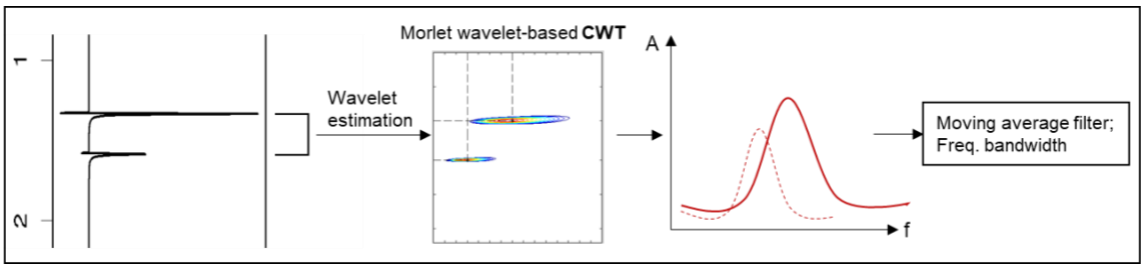

Figure 2-9. Schematic diagram of technique V

2.4 Numerical Example

To investigate the performance of each *Q* estimation methods and techniques, we implement different combinations of methods and techniques under given conditions. The explored factors are shown in Table 2-1. One would expect the level of signal frequency to affect the *Q* estimation due to its frequency dependency. Therefore, we test two candidate frequencies: 50 Hz which approximately accords with traditional seismic reflection surveys, and 1.5 kHz corresponding to high-frequency surveys such as sonic logs. Moreover, noise is another essential factor that would damage the data and *Q* estimation. Investigation of relations between noise scale and *Q* estimation has practical significance. Lastly, we test layers of different intrinsic *Q* values in order to explore measurement accuracy across different geologic media, with the hypothesis being that lower *Q* values should be measured with greater accuracy due to a more detectable frequency shift. All combinations of parameter values in Table 2-1 are tested.

Table 2-1. Cases analyzed

Parameters	Values
Dominant frequency f_p (Hz)	50, 1500
Signal-to-noise ratio S/N (dB)	-1, 5, 10 30, ∞
True model *Q*	10, 20, 50, 80, 120, 200
Bandwidth coefficient ε	0, 0.1, …, 0.9
Estimation methods	CFS, SRM, PFS
Techniques	TI, TII, TIII, TIV, TV

In order to consider the influence of the "thin-layer" effect and traveltime on *Q* estimation, we set a wedge model (Figure 2-10), which is simulated from a Ricker wavelet (Ricker, 1953) with frequency of 50 Hz and 1500 Hz and a reflectivity model of which the thickness varies from 0 to 2.5 times of the signal period (*T*), namely 0 ~ 50 ms for 50 Hz source wavelet and 0 ~ 1.6 ms for 1500 Hz. The reason we set the thickness as units of period is that we hope to discuss the effect of the wavelet overlapping on *Q* estimation regardless of the velocity. Using period to represent the

length of wavelets would account for the situations with different frequencies without the need of considering velocity. The simple 2D synthetic trace data (100 traces) are simulated through convolution of the reflection model with the source wavelets and attenuated reflection wavelets. The evolution of the amplitude spectrum through time is modeled by

$$R(f) = G(f)H(f)S(f). \qquad (2-9)$$

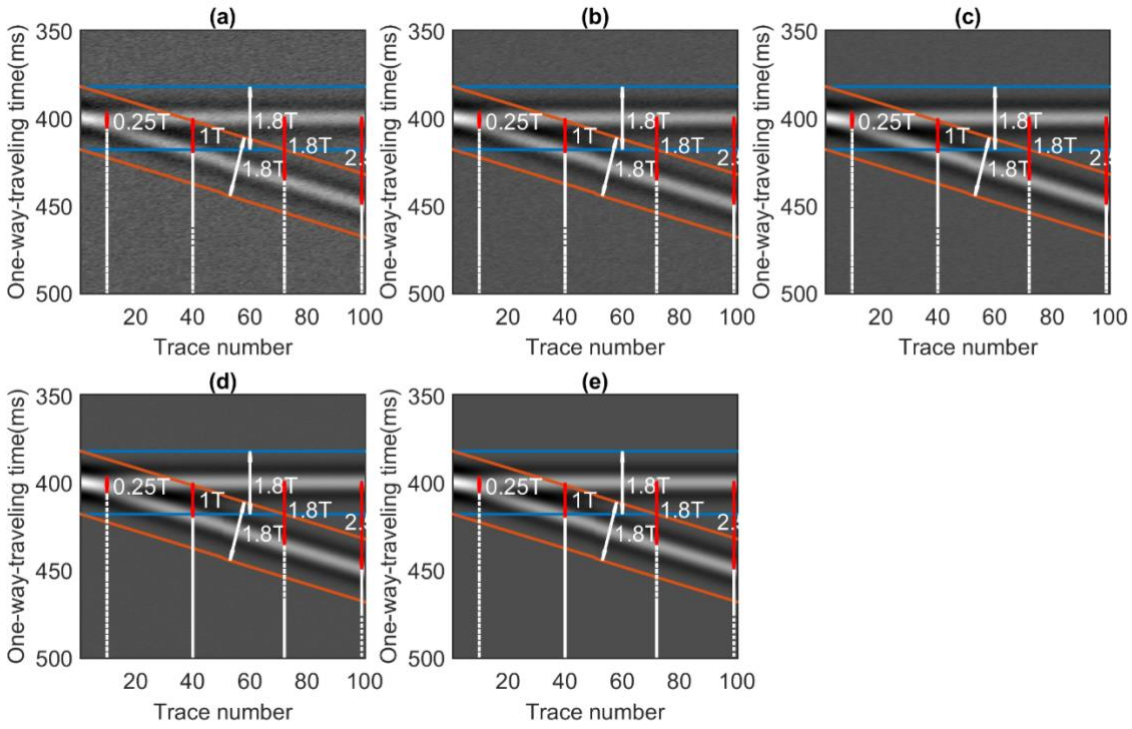

Figure 2-10. A 2D wedge model used in this study. The minimum thickness is 0 at Trace 1 and the maximum thickness is 2.5 times of the signal period (T) at trace number 100. The S/Ns are -1 (a), 5 (b), 10 (c) 30 (d), ∞ (e), respectively. The solid blue line indicates the picked signal for the first interface, while the red one represents the picked signal for the second interface. The width of each interface is 1.8 times of the signal period. The white dashed lines indicate the trace numbers corresponding to one-way traveltime of 0.25T, 1T, 1.8T, 2.5T, respectively.

Since in the equation 2 - 2, 2 - 3, 2 - 7 there is no term with respect to $G(f)$, including geometric spreading or other factors that do not change with frequency, we can ignore it when forward modeling the seismic wave propagation by convolution, meaning that only the absorption attenuation is considered. Thus, the velocity or density information is not necessary to be assigned to the model because they are not participating in either the absorption calculation or the

convolution algorithm. Please note that's different from the wave-equation forward modeling, but effective for discussing the *Q* estimation by those three spectral methods. Also, we only model the zero-offset trace that we can assume the first interface as source wavelets or reference wavelets, which is a very important assumption for those estimation methods. The attenuation is performed in spectral domain for each spectrum by equation 2 - 1. For the convenience, all traveltime here is transferred into one-way traveltime. To keep the balance between the temporal resolution and computational cost, we use sample rate dt = 500 μs for the frequency at 50 Hz and dt = 20 μs for the frequency at 1500 Hz. Figure 2-11 shows the last trace of the wedge model and its spectrum. The five S/Ns -1, 5, 10, 30 and ∞ are investigated.

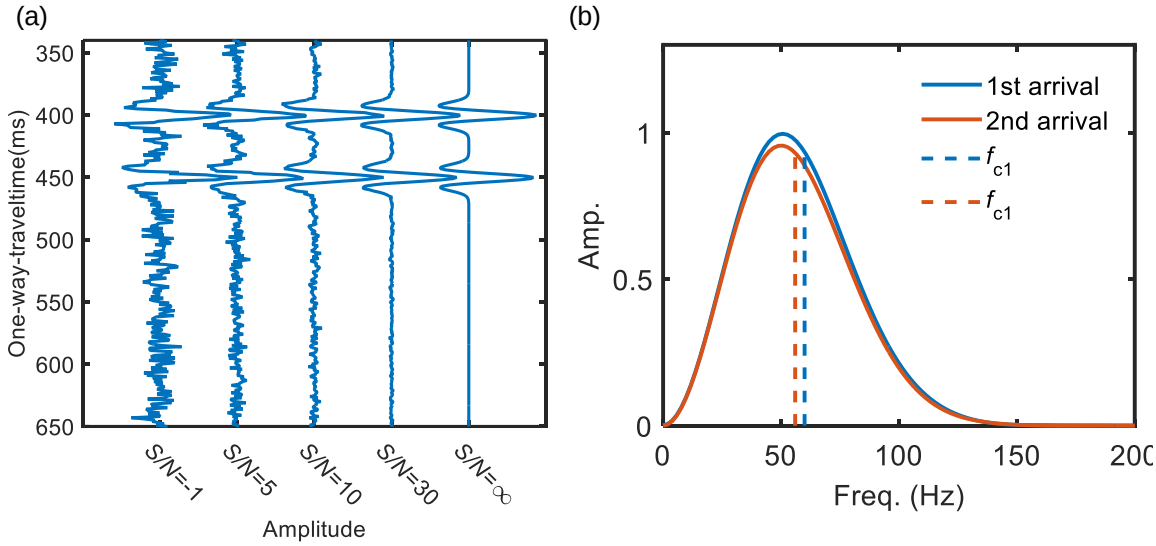

Figure 2-11. a. The last trace of wedge model with different S/Ns; b. the spectrum of first and second arrivals for S/N = ∞ and their centroid frequencies.

2.5 Results and Discussion

2.5.1 Window Size Test

Before discussing window size, we must define a mean absolute percentage error (MAPE) to assess the estimation performance. It is the relative error between estimated $\hat{Q}$ and true Q, averaged over the range of traces i, as in equation 2-9. The "estimation error" in the following discussion means MAPE unless noted otherwise.

$$MAPE(\%) = \frac{1}{N}\sum_{i=1}^{N}\frac{\hat{Q}_i - Q_i}{Q_i} \times 100 \qquad (2-10)$$

As showed in Figure 2-10, the window size is defined as the truncated signal length. For instance, the window size of 1.8T (T represents signal period) means to truncate the signal from the 0.9T above the center of the wavelet to 0.9T below the center of the wavelet. The window size determines the effective signal. Too large of a window size will reduce the estimation resolution. Too small of a window size, however, is not able to represent the whole wavelet or leads to frequency leakage when applying Fourier transformation. Before the window size test, we define a concept called "noninterference zone", which represents the traces from which Q is accurately estimated in the wedge model. Figure 2-12 is a schematic diagram for estimated $\hat{Q}$ varying with different traveltime from 0 to 2.5T. The smaller trace number corresponds to a thinner target layer where there exists a great chance of the wavelet interference. So, in the smaller-trace-number zone, the estimation is not expected to be accurate. While in the noninterference zone the estimated $\hat{Q}$ agrees better with the set-up Q (the absolute percentage error tolerance is set as 5% for this case). The beginning trace of the noninterference zone indicates the minimum traveltime of which the Q is able to be measured under the MAPE of 5%.

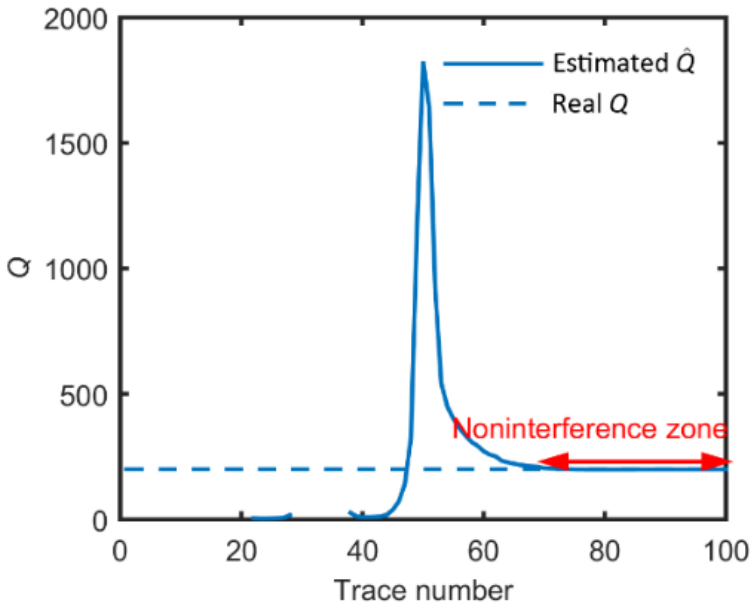

Figure 2-12. Estimated $\hat{Q}$ from the wedge model varying with different traces. The true Q is set as 200 as the dashed line. The smaller trace number means less traveltime, thus more strong interference of wavelets. The wavelet interference which occurs before trace number about 70 between first and second interfaces impairs the Q estimation.

For the purpose of investigation of the optimal window size when conducting Q estimation from reflection data, we implement fifteen combinations of methods and techniques on the model of Q = 200, f_p = 50 Hz, S/N = ∞, with the window size from 0.5T to 2T. In Figure 2-13a, it is obvious that the estimation errors reach the minimum when the window size is larger than 1.5T. The larger window size assures the smaller error; however, in Figure 2-13b we can see the noninterference zone starts at a larger trace number (thicker layer) when choosing a bigger window size, which means for larger window size the ability or resolution of the vertical detection decreases. So, there is a trade-off between the estimation error and vertical resolution. Ultimately, we take 1.8T as a balanced value for the window size. Conservatively, the trace number 70 could be the beginning of the noninterference zone for all estimations, as these marks where the first and second truncated signals are separated from each other in Figure 2-10. We also conduct window size tests for models with different Q's and different source wavelets. It leads us to the very similar conclusions.

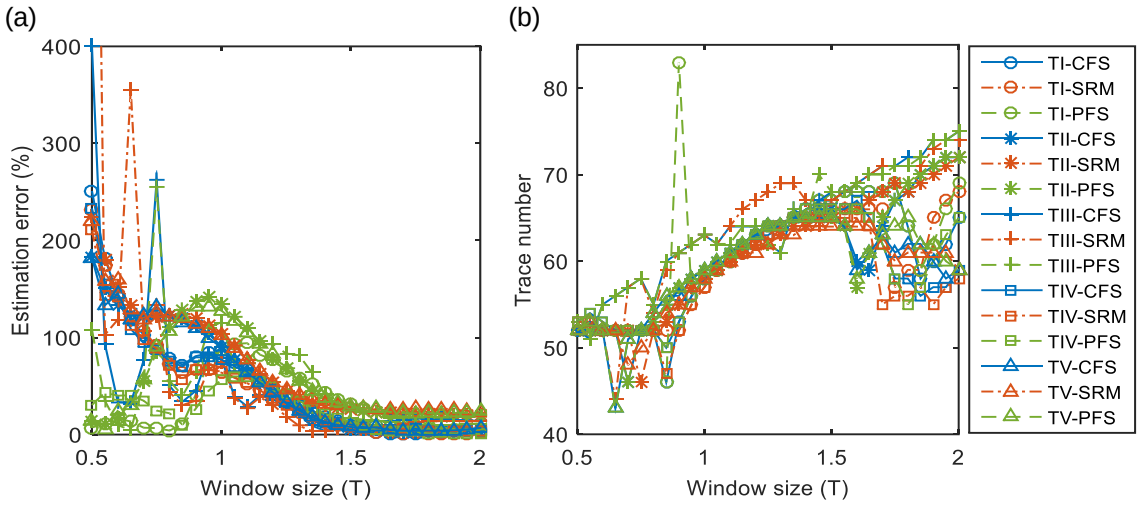

Figure 2-13. a. Estimation errors with window size under the condition of f_p = 50 Hz, Q = 200, S/N = ∞; b. beginning trace of noninterference zone with window size. The larger trace number means the noninterference zone starts at a thicker layer. In other words, larger trace number corresponds to lower vertical estimation resolution.

2.5.2 Comparison of Methods/Techniques for S/N = ∞ and f_p = 50 Hz

Estimation failure rate/null value occurrence

Sometimes, the torture of the signal would make the dominant frequency of the received wavelet larger than that of the source wavelet. When this occurs, it produces no estimation of Q (null or NA values) or illegitimate estimate of Q (i.e., nonpositive values, which we set as null). The estimation failure might occur due to factors such as the interference of noise, spectrum transformation or truncated length. The percentage of the number of the null values to the total trials is defined as the failure rate. Investigation of the failure rate leads us to a view of the ability of the method's or technique's resistance to those factors. We will cover the failure rate in the following discussion.

Influence of the Q model

The true Q of the model represents the magnitude of the attenuation. It would be expected to have a better estimation for a highly attenuated model because a larger difference between the source and received wavelets is more detectable with smaller relative error. We analyze the estimation error and failure rate in different perspectives. Figure 2-14a shows the estimation errors with different Q models for each technique-method. In general, there is not much relation between the model Q and the estimation error. This point could also be demonstrated by the boxplot of MAPEs in Figure 2-14b, which counts on data from all technique-methods as a whole. But the smaller model Q generates less estimation variance, which makes the Q measurement more stable. Additionally, the total estimation failure rate not significantly but gets higher with a larger true Q (Figure 2-15). A possible explanation could be that the smaller Q which corresponds to larger attenuation on signal spectrum would diminish the relative errors of frequency shifts (Table **2-2**) when using them as denominator in equation 2 - 3 or 2 - 7. To sum up here, the accuracy of Q estimation by all methods and techniques is subjected to the Q model itself.

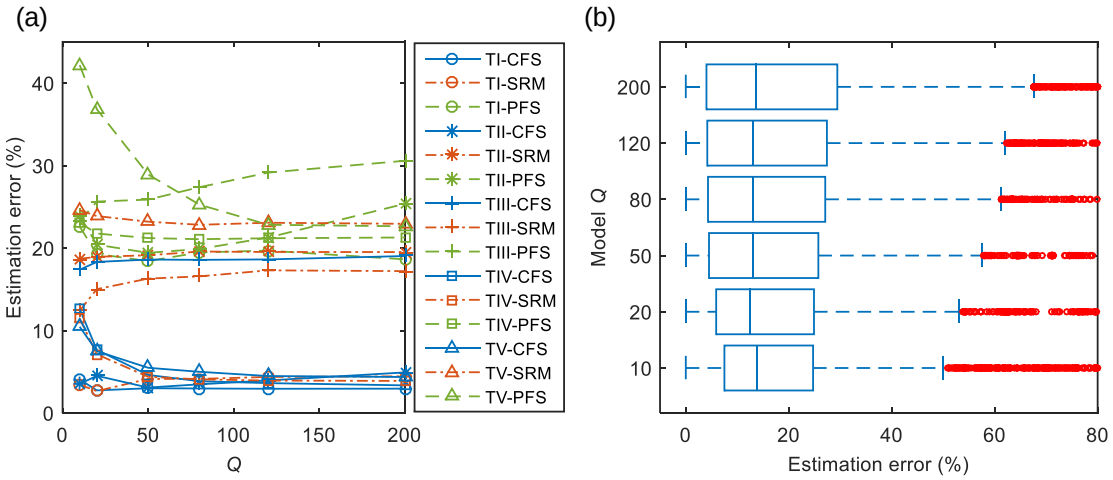

Figure 2-14. a. Estimation errors with different Q models; and b. boxplot of the MAPEs for different Q models under f_p = 50 Hz and S/N = ∞ for the noninterference zone (trace number from 70 to 100). The MAPEs are averaged over all frequency-bandwidth coefficients for the noninterference zone.

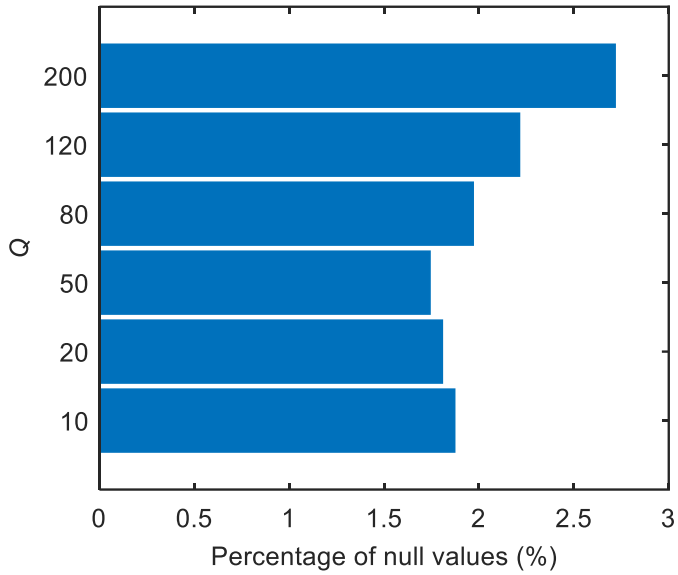

Figure 2-15. Estimation failure rates of the different Q models averaging traces of all frequency-bandwidth coefficients under f_p = 50 Hz and S/N = ∞ for the noninterference zone (trace number from 70 to 100).

Table 2-2 Frequency shift (Hz) for different models at different source frequencies.

	Model Q	10	20	50	80	120	200
Source frequency	50 Hz	6.81	3.73	2.02	1.80	1.79	1.79
	1500 Hz	214.51	111.41	66.25	59.46	59.72	59.93

Influence of the effective frequency bandwidth

The second factor influencing Q estimation is the effective frequency bandwidth. We tested ten effective-bandwidth coefficients 0.0, 0.1, 0.2 …0.9 for all Q models under f_p = 50 Hz and S/N = ∞ (Figure 2-16). Different from last analysis, the estimation errors are averaged over all Q models, not bandwidth coefficients. We still merely take the noninterference zone, trace 70 to 100, into consideration. Figure 2-17a and Figure 2-17b count data from all technique-methods on. From Figure 2-17a, bandwidth coefficients in the range of [~0.2, ~0.4] show consistently low errors for all techniques and methods with less failure rates (Figure 2-17b). In other words, the effective frequency bandwidth which covers about 60%~70% of the received wave spectrum successfully

eliminates the noise or other calculation errors within very low and very high frequencies (equation 2-8). The analysis offers us a proper choice of the bandwidth coefficient.

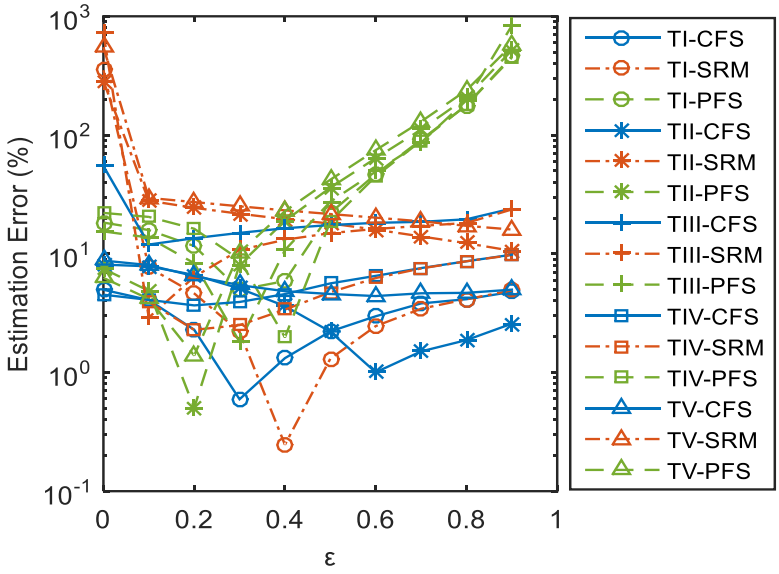

Figure 2-16. Estimation errors with different bandwidth coefficients under f_p = 50 Hz and S/N = ∞. The MAPEs are averaged over all Q models for the noninterference zone (trace number from 70 to 100).

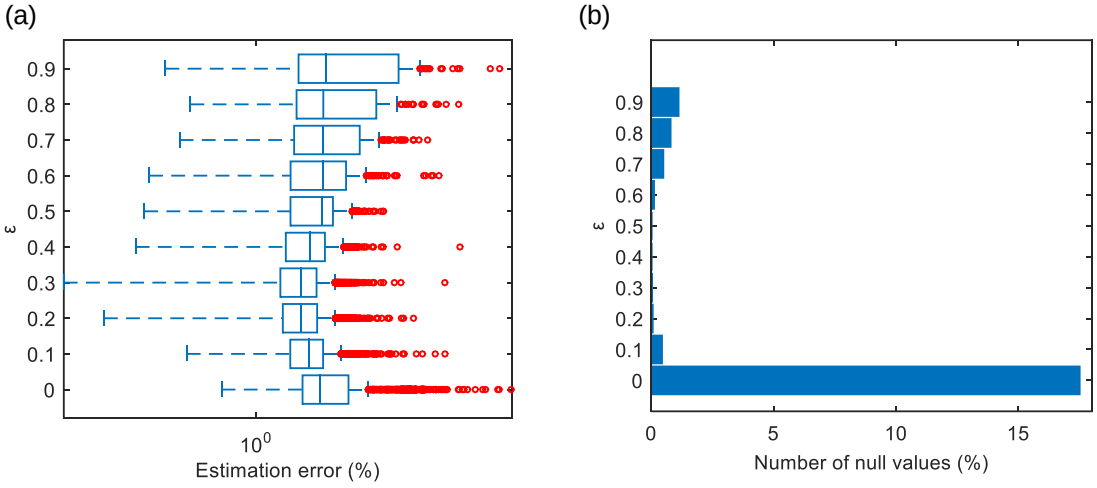

Figure 2-17. a. Estimation failure rates of the different bandwidth coefficients averaging all Q models; and b. boxplot of the MAPEs for different bandwidth coefficients under f_p = 50 Hz and S/N = ∞. The MAPEs are averaged over all Q models for the noninterference zone (trace number from 70 to 100).

Optimal methods/techniques

Figure 2-18, 19, and 20 show the performance of fifteen combinations of techniques and methods. They consider the data from all *Q* models and bandwidth coefficients. In Figure 2-18, the estimation error of CFS is consistently much lower than other methods, even though for technique III and IV errors of CFS and SRM are very close. Technique I and IV performs better than other techniques, especially for CFS and SRM. And their failure rates stay at low levels (Figure 2-19b). Figure 2-19a shows the combination of Technique I and CFS has lowest estimation error.

The reason that technique III has larger error rates is that implementing an estimated-wavelet-based CWT would add the wavelet-extraction error to the frequency transformation. On the other hand, the demanded spectrum after conducting CWT on the windowed signal is just a slice of the time-frequency map. It only considers one instantaneous time, thus more sensitive to errors. Even using average of the spectrum, it would lead to bias to the instantaneous reflection time. In addition, the mother wavelet is supposed to satisfy a technical condition of behaving like a wave (Aguiar-Conraria and Soares, 2011), which is difficult to assure in wavelet estimation. On the contrary, the technique I and IV, for example, applying FFT which takes all time window has less error rate. In terms of the worse performance of PFS, this method relies on the accuracy of peak frequency extraction, which is sensitive to errors and difficult to precisely obtain in practice.

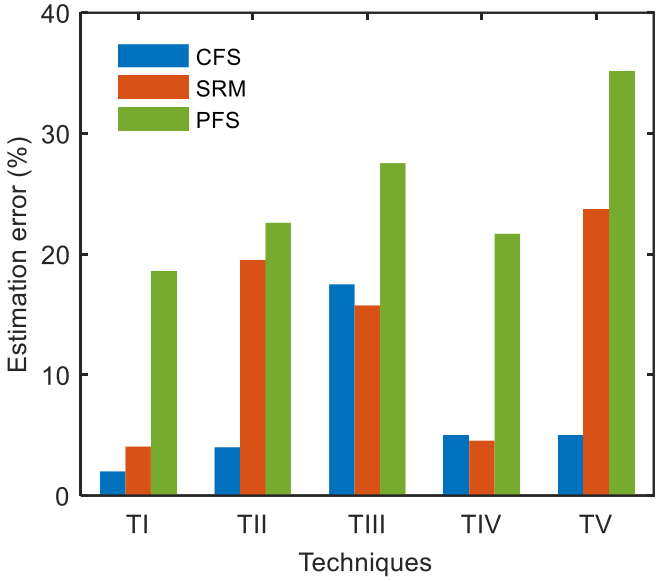

Figure 2-18. Estimation errors for methods/techniques averaging over all Q models and bandwidth coefficients for the noninterference zone (trace number from 70 to 100).

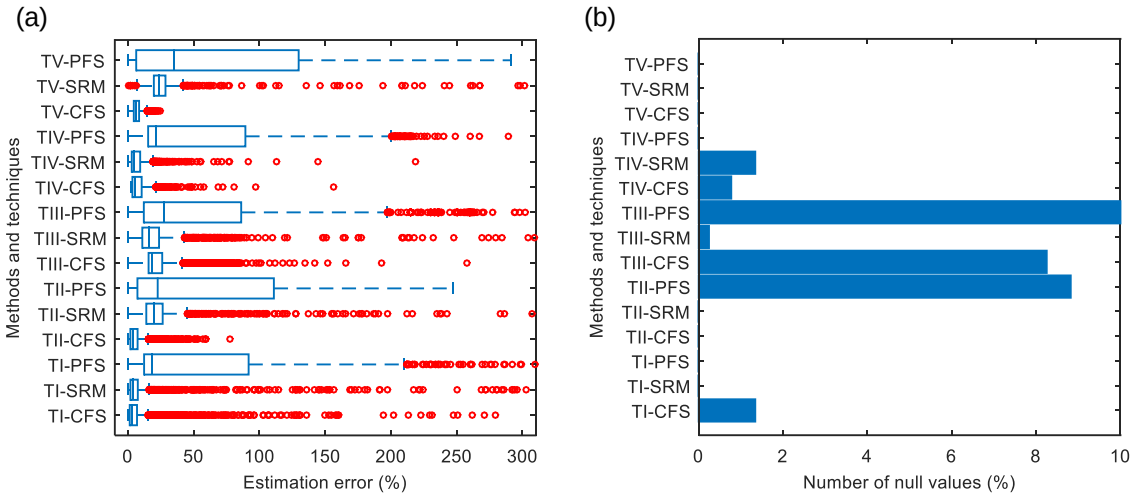

Figure 2-19. a. Boxplot of the MAPEs for methods/techniques; b. estimation failure rates of methods/techniques averaging all Q models and bandwidth coefficients. Both are condition of f_p = 50 Hz and S/N = ∞ for the noninterference zone (trace number from 70 to 100).

2.5.3 S/N Analysis for f_p = 50 Hz

As one would expect, the error rate generally increases with larger amounts of noise or smaller S/N. Figure 2-20a shows CFS stays at the lowest level of errors except for pairing with

Technique III, even across S/N levels. We can also see that TI and TIV perform the best among five techniques except for pairing with PFS in both Figure 2-20a and Figure 2-22. And Figure 2-21 proves the hypothesis that the larger magnitude of noise harms the *Q* estimation in both estimation errors and failure rates. As expected, Figure 2-20b shows that null values occur with greater frequency as more noise is added to the signal, and technique I and IV have low failure rates. Summarily, we could reach the conclusion that techniques I or IV paired with methods CFS or SRM are the optimal choices when conducting *Q* estimation under different levels of noise (Figure 2-20b and Figure 2-22).

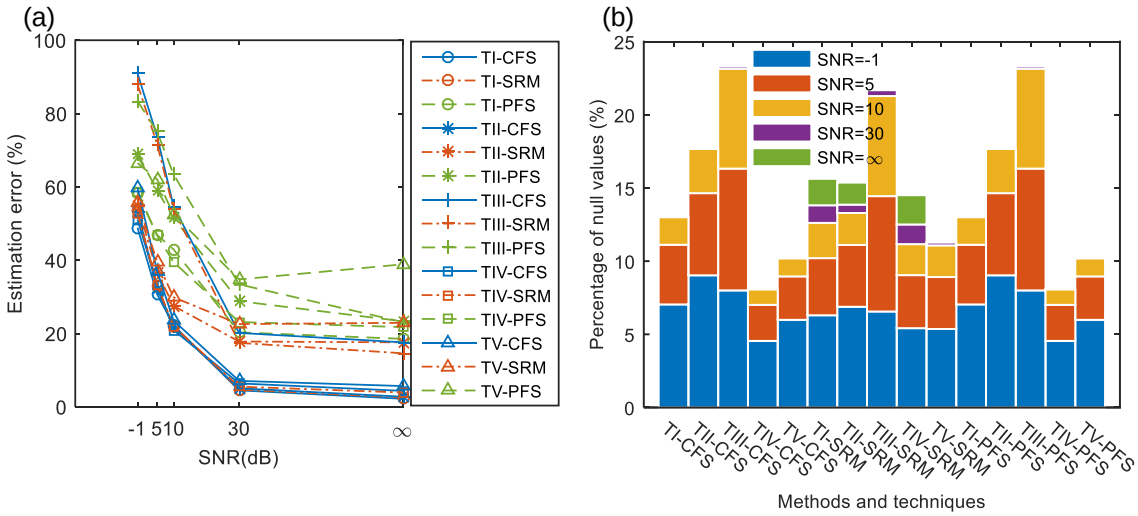

Figure 2-20. a. Estimation errors with different S/Ns under f_p = 50 Hz. The MAPEs are averaged over all *Q* models and bandwidth coefficients for the noninterference zone (trace number from 70 to 100); b. estimation failure rates for different methods and techniques with different S/Ns under f_p = 50 Hz. The percentages of null values are averaged over all *Q* models and bandwidth coefficients for the noninterference zone.

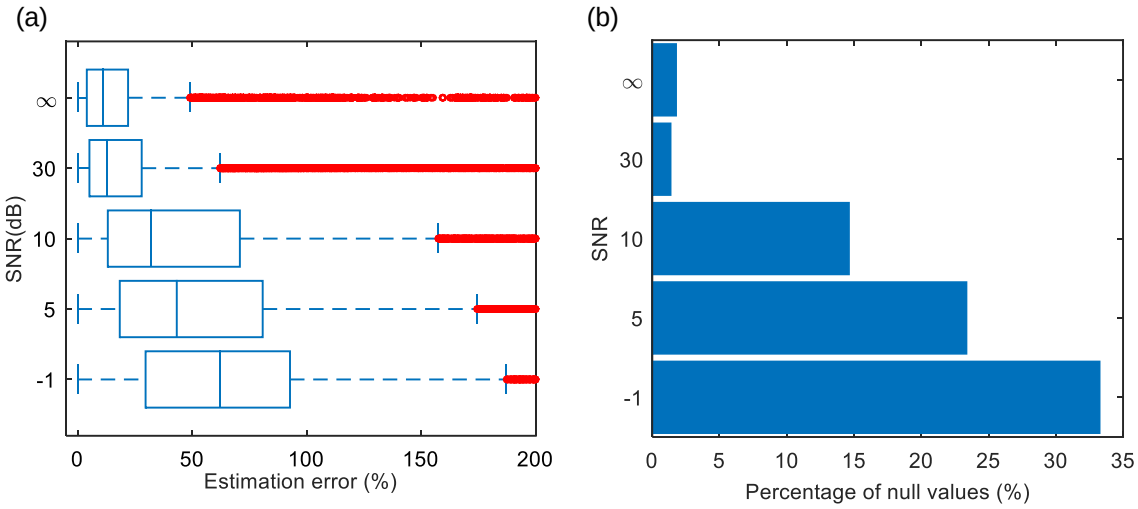

Figure 2-21. a. Boxplot of the MAPEs under f_p = 50 Hz for the noninterference zone (trace number from 70 to 100); b. estimation failure rates with different S/Ns. The percentages of null values are averaged over all Q models and bandwidth coefficients for the noninterference zone.

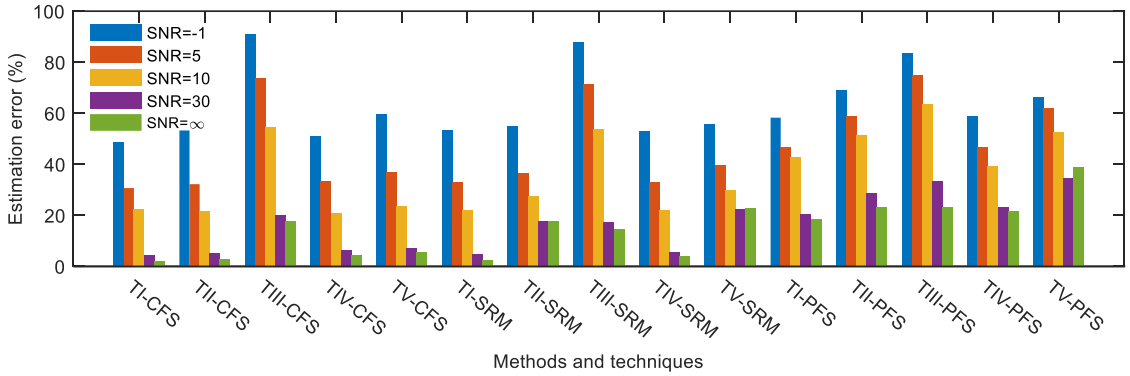

Figure 2-22. Estimation errors for methods/techniques averaging over all Q models and bandwidth coefficients for the noninterference zone (trace number from 70 to 100, f_p = 50 Hz).

2.5.4 High Frequency Case (f_p = 1500 Hz)

From Figure 2-23a to Figure 2-25, it is easy to reach the same conclusion even though we carry out estimation under different frequencies; however, the MAPEs are much smaller than that of 50 Hz case comparing Figure 2-25 with Figure 2-22. Because the relative error resulting from the absolute frequency shift decreases (Table **2-2**) while coping with a higher frequency signal.

Meanwhile, we have less estimation failure according to Figure 2-23b and Figure 2-24b. So, the high-frequency case is easier to measure accurate Q.

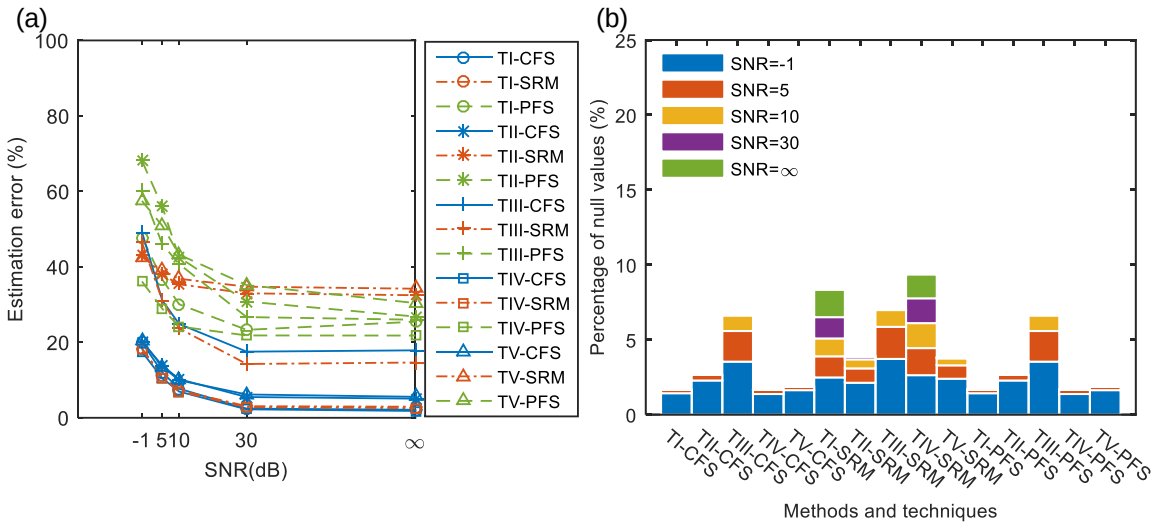

Figure 2-23. a. Estimation errors with different S/Ns under f_p = 1500 Hz. The MAPEs are averaged over all Q models and bandwidth coefficients for the noninterference zone (trace number from 70 to 100); b. estimation failure rates for different methods and techniques with different S/Ns under f_p = 1500 Hz. The percentages of null values are averaged over all Q models and bandwidth coefficients for the noninterference zone.

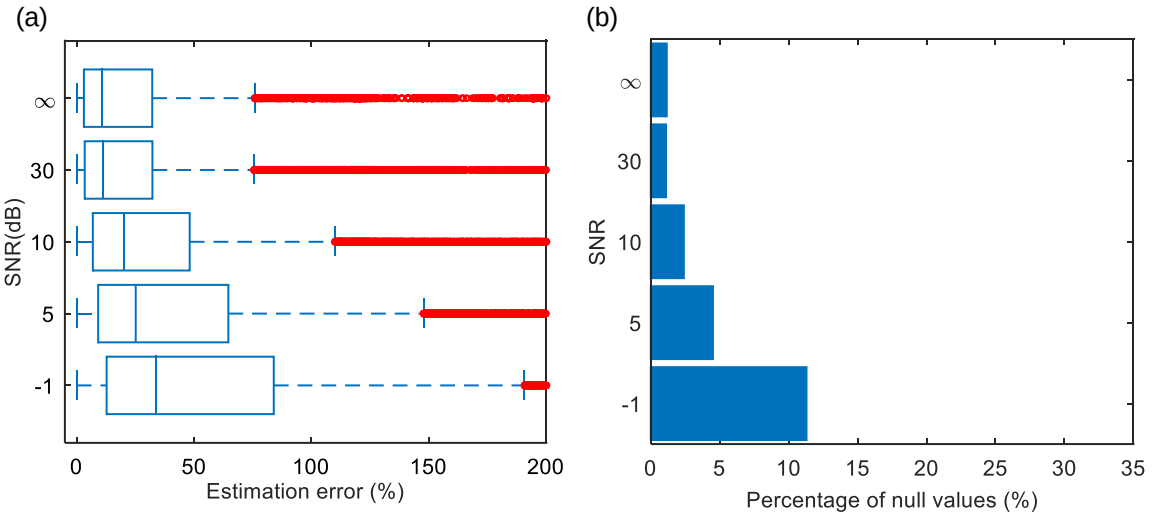

Figure 2-24. a. Boxplot of the MAPEs under f_p = 1500 Hz for the noninterference zone (trace number from 70 to 100); b. estimation failure rates with different. The percentages of null values are averaged over all Q models and bandwidth coefficients for the noninterference zone.

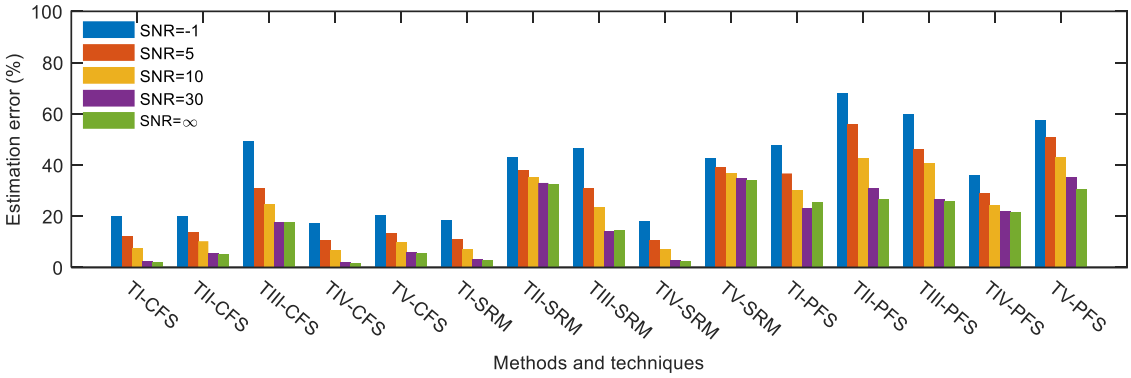

Figure 2-25. Estimation errors for methods/techniques averaging over all *Q* models and bandwidth coefficients for the noninterference zone (trace number from 70 to 100, f_p = 1500 Hz).

2.5.5 "Thin-layer" Effect

As discussed in Figure 2-12, when it comes to a very thin layer (trace number less than 70 or one-way traveltime less than 1.8*T*), the source and reflection wavelets interfere with each other, which will torture the signal spectra, leading to estimation failure or bias. Lu et al. (2007) proposed a high-order statics method to restore the wavelet, which is carried out on Technique IV and V. One would expect technique IV and V give less error rates than others for trace number less than 70 which is in the interference zone. We analyze the estimation errors and failure rates for trace number from 60 to 65. Figure 2-26a and Figure 2-27 demonstrate the hypothesis that the wavelet extraction improves the performance of *Q* measurements. Moreover, TIV and TV has less failure rates than other techniques (Figure 2-26b, Figure 2-27). This experiment tells us the wavelet estimation benefits the *Q* estimation in this aspect, even though it increases the error when associated with CWT.

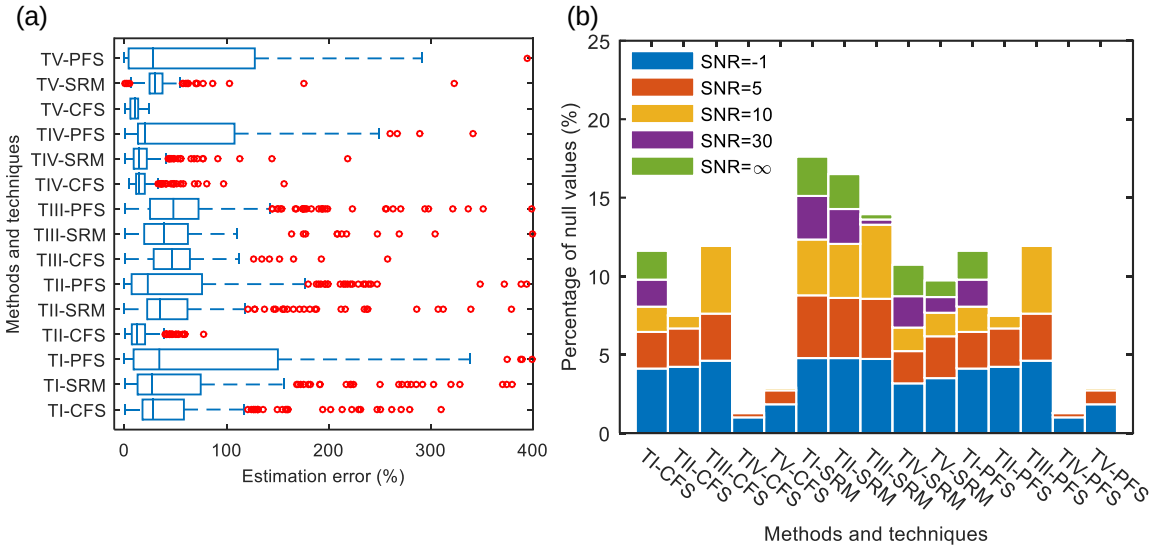

Figure 2-26. a. Boxplot of the MAPEs for methods/techniques under f_p = 50 Hz and S/N = ∞ for the interference zone (trace number from 60 to 65); b. estimation failure rates for different methods and techniques under f_p = 50 Hz. The percentages of null values are averaged over all Q models and bandwidth coefficients for the interference zone.

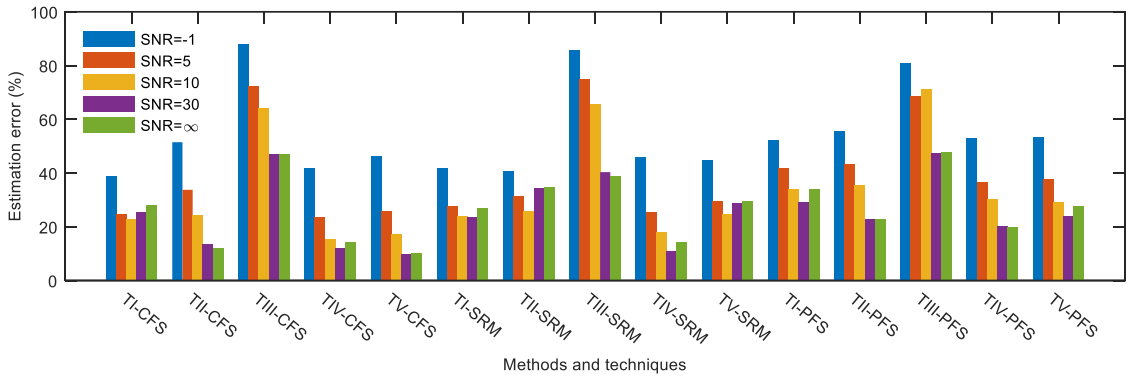

Figure 2-27. Estimation error for methods/techniques averaging over all Q models and bandwidth coefficients for the interference zone (trace number from 60 to 65, f_p = 50 Hz).

2.6 Conclusion

Three main Q estimation approaches, CFS, SRM and PFS, have been specifically analyzed. Regardless of the scattering or other frequency-independent factors in Q estimation, accurate Q measurement from seismic reflection data, especially for prestack data, is still difficult because of

much more noise intervention and more difficult interface tracking. Data preprocessing is necessary to obtain a reliable *Q*. Through this research, we provide a detailed procedure including best options to preprocess data and the optimal parameter choice under difference conditions for *Q* estimation especially when dealing with reflected seismic data.

Although the analysis in this research is based on simulated data (actually, the real *Q* in practical data is hard to know), we consider a complete set of conditions that might be faced in practice. The conclusions made here are significant in guiding the practical application. For three frequency-domain methods, five kinds of preprocessing procedures are implemented on synthetic data before *Q* estimation. After analyzing six models with ten bandwidth coefficients: firstly, the best window size when truncating signals as the source or received wavelet is 1.8 times of the signal period. This is a trade-off value considering both the estimation error and temporal estimation resolution. Secondly, even though it is not significant, *Q* of the greatly attenuated cases can be more accurately estimated because of the relative error decreasing. Additionally, the effective frequency bandwidth choice is essential to all estimation methods because the noise interference in very low or high bandwidth would have a large effect on the frequency shift. Generally, the effective-bandwidth coefficient within 0.2 ~ 0.4 is a good value. Moreover, any pair of technique I or IV and CFS or SRM gives us a smaller MAPE which could be the optimal choice of methods and techniques. And as expected, the *Q* estimation needs signals with lower levels of noise. The combinations of technique I or IV and CFS or SRM still perform better than others in cases with even higher levels of noise. But we could see that technique IV is superior in some cases because of its stronger capability of wavelet restoring once in practice where there is a "thin layer" effect, even though it brings more errors from the wavelet estimation. Lastly, carrying out tests on a higher frequency condition, the MAPE decreases for each scenario. This is good news for *Q* estimation from high-resolution, near-surface surveys which usually have higher frequencies.

So far, we specifically suggest the *Q* estimation method and their preprocessing techniques in order to have a better *Q* measurement. But there is still a problem that we do not cover, namely, the source frequency which is required to know in advance in those three methods. What we can do now in practice is to pick up the first arrival as an approximation for the source wavelet. Maybe more advanced theory should be proposed to overcome the difficulty in acquiring source wavelet in practice.

2.7 References

Aguiar-Conraria, L., Soares, M.J., 2011. The Continuous Wavelet Transform: A Primer. Nipe Wp 6–8.

Aguiar-Conraria, L., Soares, M.J., 2011. The Continuous Wavelet Transform: A Primer. Nipe Wp 6–8.

Bath, M., 1974. Spectral Analysis in Geophysics. Dev. Solid Earth Geophys. 7, 563.

Blias, E., 2011. Q-factor estimation through optimization approach to near-offset VSP data. SEG Tech. Progr. Expand. Abstr. 2011 4278–4282. doi:10.1190/1.3628100

Cheng, P., Margrave, G.F., 2013. Estimation of Q : a comparison of different computational methods. CSPG/CSEG/CWLS GeoConvention 12, 2–5.

Dasgupta, R., Clark, R.A., 1998. Estimation of Q from surface seismic reflection data. Geophysics 63, 2120. doi:10.1190/1.1444505

Dutta, G., Schuster, G.T., 2016. Wave-equation Q tomography. GEOPHYSICS 81, R471–R484. doi:10.1190/geo2016-0081.1

Engelhard, L., 1996. Determination of Seismic-Wave Attenuation By Complex Trace Analysis. Geophys. J. Int. 125, 608–622. doi:10.1111/j.1365-246X.1996.tb00023.x

Frisillo, A.L., Stewart, T.J., 1980. Effect of partial gas/brine saturation on ultrasonic absorption in sandstone. J. Geophys. Res. 85, 5209. doi:10.1029/JB085iB10p05209

Gao, J., Li, Y., Chen, W., 1998. On the instantaneous attributes analysis of seismic data via wavelet transform. 68th Ann. Internat. Mtg 1084–1087.

Gladwin, M.T., Stacey, F.D., 1974. Anelastic Degradation of Acoustic Pulses in Rock. Phys. Earth Planet. Inter. 8, 332–336. doi:10.1016/0031-9201(76)90068-6

Goutbeek, F.H., Dost, B., van Eck, T., 2004. Intrinsic absorption and scattering attenuation in the southern part of the Netherlands. J. Seismol. 8, 11–23. doi:10.1023/B:JOSE.0000009511.27033.79

Hackert, C.L., Parra, J.O., 2004. Improving Q estimates from seismic reflection data using well-log-based localized spectral correction. Geophysics 69, 1521. doi:10.1190/1.1836825

Harris, F.J., 1978. On the use of windows for harmonic analysis with the discrete Fourier transform. Proc. IEEE 66, 51–83. doi:10.1109/PROC.1978.10837

Hatzidimitriou, P.M., 1994. Scattering and anelastic attenuation of seismic energy in northern Greece. pure Appl. Geophys. 143, 587–601. doi:10.1007/BF00879499

Hauge, P.S., 1981. Measurements of attenuation from vertical seismic profiles. Geophysics 46, 1548–1558. doi:10.1190/1.1441972

Jannsen, D., Voss, J., Theilen, F., 1985. Comparison of methods to determine Q in shallow marine sediments from vertical reflection seismograms. Geophys. Prospect. 479–497.

Karl, J.H., 1989. 8 - Digital Filter Design, in: Karl, J.H. (Ed.), Introduction to Digital Signal Processing. Academic Press, San Diego, pp. 165–196. doi:http://dx.doi.org/10.1016/B978-0-12-398420-3.50012-6

Kjartansson, E., 1979. Constant Q-Wave Propagation and Attenuation. J. Geophys. Res. 84, 4737–4748.

Lu, W., Zhang, Y., Zhang, S., Xiao, H., 2007. Blind wavelet estimation using a zero-lag slice of the fourth-order statistics. J. Geophys. Eng. 4, 24–30. doi:10.1088/1742-2132/4/1/004

Müller, T.M., Gurevich, B., Lebedev, M., 2010. Seismic wave attenuation and dispersion resulting from wave-induced flow in porous rocks — A review. Geophysics 75, 75A147. doi:10.1190/1.3463417

Neep, J.P., Sams, M.S., Worthington, M.H., O'Hara-Dhand, K.A., 1996. Measurement of seismic attenuation from high-resolution crosshole data. Geophysics 61, 1175–1188. doi:10.1190/1.1444037

Oliveira, F. de S., de Figueiredo, J.J.S., Oliveira, A.G., Schleicher, J., Araújo, I.C.S., 2017. Estimation of quality factor based on peak frequency-shift method and redatuming operator: Application in real data set. GEOPHYSICS 82, N1–N12. doi:10.1190/geo2015-0234.1

Pinson, L.J.W.W., Henstock, T.J., Dix, J.K., Bull, J.M., 2008. Estimating quality factor and mean grain size of sediments from high-resolution marine seismic data. Geophysics 73, G19–G28. doi:10.1190/1.2937171

Quan, Y., Harris, M.J., 1997. Seismic attenuation tomography using the frequency shift method. Geophysics 62, 895. doi:10.1190/1.1444197

Raikes, S.A., White, R.E., 1984. Measurements of Earth Attenuation from Downhole and Surface Seismic Recordings. Geophys. Prospect. 32, 892–919.

Ricker, N., 1953. THE FORM AND LAWS OF PROPAGATION OF SEISMIC WAVELETS. GEOPHYSICS 18, 10–40. doi:10.1190/1.1437843

Rickett, J., 2006. Integrated estimation of interval-attenuation profiles. GEOPHYSICS 71, A19–A23. doi:10.1190/1.2209722

Rossi, G., Gei, D., Böhm, G., Madrussani, G., Carcione, J.M., 2007. Attenuation tomography: An application to gas hydrate and free gas detection. Geophys. Prospect. 55, 655–669.

Sams, M., Goldberg, D., 1990. The validity of Q estimates from borehole data using spectral ratios. GEOPHYSICS 55, 97–101. doi:10.1190/1.1442776

Sheriff, R.E., Geldart, L.P., 1995. Exploration Seismology, 2nd Editio. ed. Cambridge University Press.

Tary, J.B., van der Baan, M., Herrera, R.H., 2017. Applications of high-resolution time-frequency transforms to attenuation estimation. GEOPHYSICS 82, V7–V20. doi:10.1190/geo2016-0022.1

Toksöz, M.N., Johnston, D.H., Timur, A., 1979. Attenuation of seismic waves in dry and saturated rocks: II. Mechanisms. Geophysics 44, 691. doi:10.1190/1.1440970

Tonn, R., 1991. the Determination O F the Seismic Quality Factor Q From Vsp Data: a Comparison of Different Computational Methods' R a I N E R T O N N 2. Geophys. Prospect. 39.

Tu, N., Lu, W., 2010. Improve Q estimates with spectrum correction based on seismic wavelet estimation. Appl. Geophys. 7, 217–228. doi:10.1007/s11770-010-0252-2

Winkler, K.W., Nur, A., 1982. Seismic attenuation: effects of pore fluids and frictional sliding.

Geophysics 47.

Zhang, C., Ulrych, T.J., 2002. Estimation of quality factors from CMP records. Geophysics 67, 1542. doi:10.1190/1.1512799

Zhang, R.-W., Li, H.-Q., Wen, P.-F., Zhang, B.-J., 2016. THE VELOCITY DISPERSION AND ATTENUATION OF MARINE HYDRATE-BEARING SEDIMENTS. Chinese J. Geophys. 59, 539–550. doi:10.1002/cjg2.30005

Chapter 3 **Estimation of Free Gas Saturation and Porosity by Joint Bayesian Inversion of P- and S- Wave Attenuation**

3.1 Abstract

Seismic attenuation is an effective indicator of free gas. Compared with velocity, anelastic attenuation is more sensitive to saturation and porosity. Quantitatively estimating various rock properties from seismic attenuation is a high-dimensional nonlinear inverse problem. We propose a Bayesian workflow to estimate properties of gas-charged porous media by joint inversion of P- and S-wave quality factors. This joint Bayesian inversion strategy utilizes a previously published rock physics model for anelastic attenuation of both P- and S-waves. Firstly, the centroid frequency shift method is used to estimate the quality factor from OBS data collected in Finneidfjord, Norway. Then, we establish the posterior distribution under the assumption that the errors between measured and modeled Q_p and Q_s follow independent normal distributions, and by specifying prior distributions for the inputs to the rock physics model. Lastly, a Markov Chain Monte Carlo algorithm, as an efficient sampling approach, is implemented to sample the candidate values to construct the solution distribution. Compared to the inversion on Q_p alone, the additional Q_s dramatically reduces the solutions from an infinite number to two. The residual ambiguity of this problem (occurrence of multiple solutions) results from nonlinearity of the physical equations, and it is further mitigated by constraints on the prior information (rock and fluid properties). The advantage of applying a Bayesian approach is that we could have not only the estimation of parameters but also their uncertainties. The results for gas saturation and porosity are in good agreement with previous research in Finneidfjord.

3.2 Introduction

The geophysical inverse problem results from the transformation of any geophysical data into physical properties of the earth (Bosch et al., 2010). Particularly, for seismic inversion the final goal is to infer the rock properties, here gas saturation and porosity are mainly discussed, of the subsurface from seismic data. There are two procedures in order to realize the goal: 1) invert the elastic properties from seismic observation data; 2) estimate the rock properties from the elastic properties via rock physics models. The first step is a linearized inversion (Buland and Omre, 2003; Buland and El Ouair, 2006); however, the second step is usually a highly nonlinear problem with multi-solutions (Cary and Chapman, 1988), which means more than one configurations of elastic earth models fit the seismic data. Generally, applying more constraints on the parameters results in less ambiguity in the solution set (fewer multiple solutions). Many books give more background on the subject of geophysical inverse theory (e.g., Menke, 1984; Tarantola, 1987; Parker, 1994; Sen and Stoffa, 1992; Oliver et al., 2008).

Seismic inversion can be grouped into two major approaches according to solution methods: deterministic and stochastic. The first one utilizes analytical or numerical algorithms to obtain the solution to the inverse problem, whereas the second one searches the best solution by sampling from the posterior probability density and knowing the uncertainty simultaneously. Russell (1988) summarized two of the widely used deterministic approaches: sparse-spike techniques and model-based inversion. The former was initially proposed by Oldenburg et al. (1983), of which deconvolution was imposed on the seismic traces assuming that the reflectivity series are sparse. The latter one (Russell and Hampson, 1991) iteratively updated the synthetic model until minimizing some criteria. For the second category, Bayesian inversion is a typical stochastic approach, which samples the posterior function that consists of likelihood and prior information via Markov Chain Monte Carlo algorithms (Tarantola, 1987; Morgan et al., 2014).

Gouveia and Scales (1998) defined a Bayesian nonlinear model and estimated the maximum-posterior elastic parameters. The ability of quantifying the uncertainties caused by measurement or model errors makes stochastic approaches superior to deterministic ones. Understanding the uncertainty facilitates the risk analysis and optimal decision-making.

The commonly-used seismic inversion methods are velocity based for either deterministic or stochastic approaches. However, seismic attenuation is also, or even more, strongly related to the rock properties. For example, at higher levels, CO_2 saturation generates little P-wave velocity response in theoretical studies (Carcione et al., 2006), laboratory experiments (Lei and Xue, 2009) and field studies (Chadwick et al., 2005; Daley et al., 2011). Whereas at lower levels of gas saturation, Ecker et al. (2000) and Zillmer (2006) found that P-wave velocity is way too sensitive to gas saturation. On the other hand, attenuation was significantly affected by gas saturation (Müller et al., 2010), which is also shown in the sensitivity analysis of this study (Methodology Section). In 1956, Biot firstly established an analytical relation between rock properties and seismic attenuation (Biot, 1956 a,b). More seismic attenuation models were proposed after that (e.g., White, 1975; White et al., 1975; Dvorkin and Mavko, 2006).

Attenuation (which is proportional to the inverse of quality factor, Q^{-1}) refers to the exponential decay of the wave amplitude with propagating distance. It is caused by energy-conserved factors (scattering or geometric dispersion), and anelastic dissipation (intrinsic attenuation) where energy is converted into heat. The intrinsic Q is of particular interest to exploration geophysicists. Because it is important in wave-propagation forward modeling (e.g., Zhu and Harris, 2015); inverse Q filtering; indicating hydrocarbons (Klimentos, 1995; Zhao et al., 2004); and improvement of full waveform inversion (Barnes et al., 2014). In this study, we explore its ability to quantitatively estimate rock and fluid properties. Sometimes, it is difficult to distinguish the intrinsic attenuation from scattering attenuation because both of them are frequency dependent. However, significant scattering will occur only when the inhomogeneity is comparable

in scale to the wavelength of the propagating elastic waves (Jackson and Anderson, 1970). When considering homogeneous media, we do not expect a significant level of scattering effect.

Many models quantitatively describe the intrinsic attenuation. The earliest and significant one is the wave-induced-fluid flow model for fluid-saturated rocks (Biot, 1956ab; Stoll and Bryan, 1970), of which the fluid flows through the pores or cracks due to fluid-pressure equilibration between the peaks and troughs of a compressional wave or due to grain accelerations in the case of a shear wave, accompanying with internal friction until the pore pressure is equilibrated. Pride et al. (2004) complemented Biot's model at mesoscopic scales. The second kind is the attenuation resulting from "squirt" flow (Mavko and Nur, 1979; O'Connell and Budiansky, 1974). For partially-saturated liquid-gas systems, local pressure gradients generated by wave compression on rocks lead to fluid movement and viscous dissipation— "squirt" flow. Dvorkin and Nur (1993) offered a BISQ model to treat both Biot and "squirt" flow mechanisms as coupled processes and relate P-wave velocity and attenuation to macroscopic parameters. Additional models include: Walsh's model (1966), based on the friction dissipation when crack surfaces slide to one another; White's spherical model (White, 1975), quantifying the attenuation due to the gas bubble squeezing and moving by introducing a spherical water pockets with a gas bubble at the center; White's layered model (White et al., 1975), considering a thick section of rock composed of alternating sublayers of porous rock saturated with different saturating fluids.

Summarily, seismic attenuation inversion is a powerful and novel tool in reservoir characterization. Singleton and Images (2007) utilized Q_p and Q_s to complement impedance inversion. Raji and Rietbrock (2012) inverted the saturation from a theoretical attenuation-saturation curve, but had to treat each case individually with the precondition of various rock properties for a given field site. Morgan et al. (2012) inverted gas saturation by P-wave attenuation through the use of a genetic algorithm.

In this paper, we jointly invert gas saturation and porosity from Q_p and Q_s. Compared with only Q_p inversion (Morgan et al., 2012), one more dimension of information is added. It allows us to invert two parameters at the same time and, to some extent, suppressed the ambiguity of this problem. In addition, we take the frequency dispersion of the attenuation into consideration. The Q and velocity vary with different frequency bandwidth (Batzle et al., 2005). The added frequency term in rock physics models for attenuation better rationalizes the joint inversion, which is not considered in impedance inversion. The method is applied to estimate gas saturation and porosity of Finneidfjord, Norway. The inverted gas saturation and porosity are in a good agreement with the results from former reports of this area (Tinivella and Lodolo, 2000; Dickens et al., 1997; Holbrook et al., 1996; Lu and McMechan, 2002).

3.3 Data

3.3.1 Geological setting

Finneidfjord, Norway (Figure 3-1) has a history of landslides, which made it the subject of recent, active field of investigation (Vanneste et al., 2013; Vardy et al., 2012). One suspected factor contributing to offshore slope failure is the accumulation of biogenic free gas in the sub-seabed. These gas-charged sediments can be seen easily in seismic profiles. Determining the properties of the subsurface gas is necessary for characterizing its role in the slope destabilization. The free gas zone is identified around 15 mbsf (meters beneath seafloor) (Vardy, 2015). It is contained in shallow and unconsolidated sediments, where the gas saturation cannot be very high and the porosity is larger than critical porosity, thus the rock is in a suspension state. The gas saturation here is less than 1% according to the inversion of attenuation from airgun data in this area (Morgan et al., 2012). The porosity as recorded is about 0.58 by Leynaud et al. (2007). The performance of the attenuation inversion on this very low gas-saturated sediments is a good example to demonstrate its efficacy. And the rich prior information helps to validate the method and reduces the ambiguity of saturation (see “discussion section” for details).

We use the OBS data (Figure 3-2) because of its capability of detecting both P wave and S wave information. The shot interval is about 8.2 m on average and the dominant frequency is around 200 Hz. The hydrophone recordes the P waves. As there is no compass within the instruments, the orientation of the two horizontal components is unknown, and the conventional procedure is to rotate the components into inline (X) and crossline (Y). After component rotation, the radial component R from horizontal X and Y components mainly contains S waves. In order to conserve the amplitude and mitigate the measurement error, the raw data of which the CDP’s are so close that they are considered as one point (white line in Figure 3-1) is selected to average the estimated

Q's. The labeled "Layer 1" as shown in Figure 3-2 is targeted free-gas zone according to the time-to-depth transformation, which could be realized by sonic log velocity in this area.

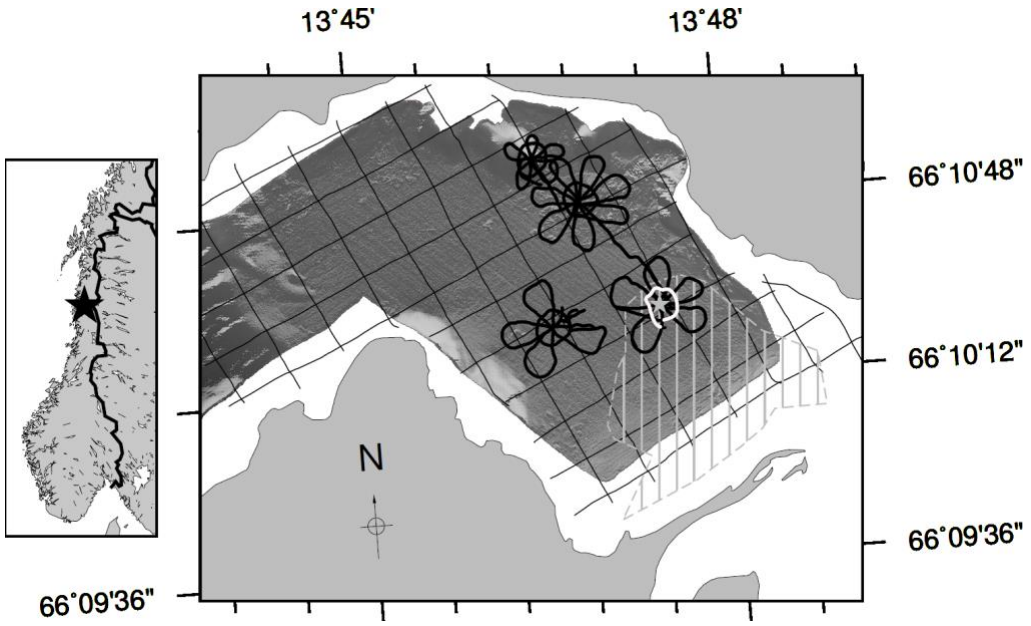

Figure 3-1. OBS survey in Finneidfjord, Norway. The gray star indicates the OBS; Black curves represent shots by the shipboard boomer. The white circle is the traces selected for *Q* estimation. The potential free gas area is shown as the hatched polygon.

3.3.2 Measuring Attenuation

To get the best-measured attenuation, the basic preprocessing steps we take are (Lei and Morgan, 2016): in case of the frequency leakage, the Hamming window is applied to truncate the target signal for spectral transformation. Then, the time series from each window is transformed to the frequency domain via Fast Fourier Transformation (FFT) after zero-padding to improve the spectral resolution. Sometimes, residual noise in the signal could propagate into the spectrum. A moving average filter is a common technique to smooth the spectrum (Karl, 1989). A crucial factor affecting the accuracy of *Q* estimation is the effective-frequency bandwidth, which suppresses the lower and higher frequency noise (Tu and Lu, 2010). After preprocessing, the centroid frequency shift method as recommended by Lei and Morgan (2016) is used to estimate Q_p and Q_s for the place

where sub-seabed free gas has been observed. The OBS data *H* component is used for P- wave attenuation estimation and the rotated *R* component is used for S- wave attenuation estimation. Both Q_p and Q_s are obtained by averaging those neighbored traces in order to stand for the *Q* of the center point.

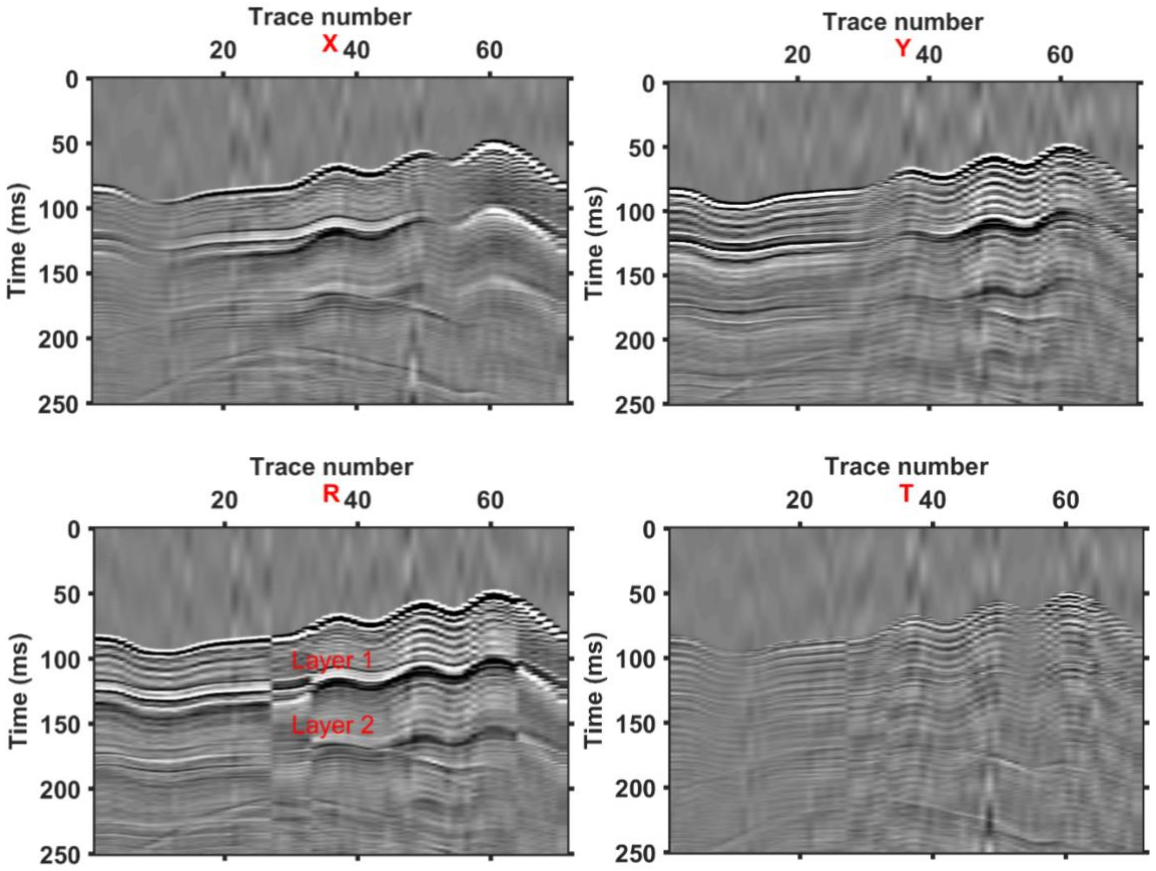

Figure 3-2. *R* and *T* components (bottom) of OBS data after component rotation of *X* and *Y* components (top). The waveform energy is converted from *X* and *Y* components to *R* component. Only 70 traces showed, totally 556 traces. "Layer 1" is of interest, where the gas reservoir was discovered (Morgan et al., 2012; Vardy 2015).

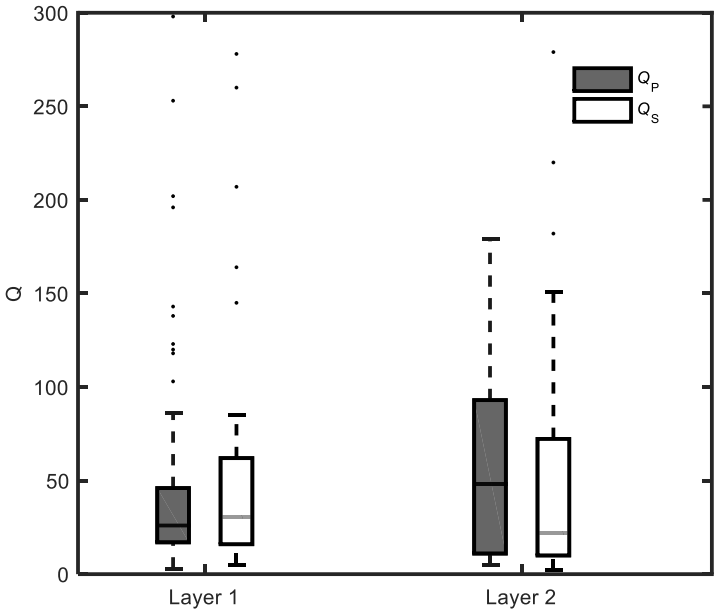

Figure 3-3. Q_p (gray box) and Q_s (white box) estimated from Finneidfjord, Norway by centroid frequency shift method with technique I (Lei and Morgan, 2016). If taking the median, the quality factor of the first layer is $Q_p = 26.0$, $Q_s = 30.5$; the quality factor of second layer is $Q_p = 48.0$, $Q_s = 22.0$.

The measured Q is the effective or apparent quality factor Q_{eff} of a geological formation, which dependes on not only the intrinsic attenuation but also scattering attenuation. However, it is reasonable to assume the scattering effect is negligible for dataset we use at Finneidfjord, Norway (Morgan et al., 2012), because the sediments are reasonably homogenous considering the very shallow and simple reflections. In addition to that, the geometric spreading and reflection effects, which can be assumed to be independent of frequency, have no impacts on frequency-dependent intrinsic Q estimation when using centroid frequency shift method (Quan and Harris, 1997; Hackert and Parra, 2004; Pinson et al., 2008).

3.4 Methodology

Assuming $\boldsymbol{Q} = (Q_p, Q_s)$ is measured from seismic data of gas-charged media with sediment properties $\boldsymbol{m} = (\theta_1, \theta_2, \ldots \theta_m)^T$, the seismic intrinsic attenuation can be linked to the unknown parameters via

$$\boldsymbol{Q} = g(\boldsymbol{m}) + \boldsymbol{e} \qquad (3-1)$$

where $g(\boldsymbol{m})$ denotes the rock physics model; $\boldsymbol{e}$ includes the measurement error of $\boldsymbol{Q}$ and model error. The goal is to inversely solve this equation to estimate the parameters $\boldsymbol{m}$ and its uncertainty. Bayesian methods have been previously used to estimate reservoir properties from seismic data (Grana and Mukerji, 2015; Doyen, 2007). Its capability of detecting multi-solutions and uncertaintities makes it a very promising method.

According to the Bayes theorem, the posterior distribution of $\boldsymbol{m}$ given $\boldsymbol{Q}$ is proportional to the likelihood of $\boldsymbol{Q}$ given $\boldsymbol{m}$ times the prior distribution of $\boldsymbol{m}$. Next, let's see how to calculate the likelihood and prior in order to get the posterior. Assuming the error $\boldsymbol{e}$ is Gaussian distributed, the likelihood is

$$L(\boldsymbol{Q}|\boldsymbol{m}) = \exp\left\{\frac{1}{2}[\boldsymbol{Q} - g(\boldsymbol{m})]^T \boldsymbol{\Sigma}_e^{-1}[\boldsymbol{Q} - g(\boldsymbol{m})]\right\} \qquad (3-2)$$

where $\boldsymbol{\Sigma_e}$ is the covariance matrix of error between the observed $\boldsymbol{Q}$ and modeled quality factor $g(\boldsymbol{m})$. Please note that there is a natural logarithm operator on $\boldsymbol{Q}$ because $\boldsymbol{Q}$ is strictly positive, and the logarithm of $\boldsymbol{Q}$ follow a Gaussian distribution from positive infinite to negative infinite. Assuming all parameters are independent of each other, the prior should be

$$\pi(\boldsymbol{m}) = \prod_{i=1}^{n} \pi(m_i) \qquad (3-3)$$

where there are many ways to assume the prior distribution for one parameter $\pi(m_i)$ (Gelman et al., 2004). The commonly used three approaches are as follows: a) uniform prior: when there is not

enough prior information, we can consider a uniform distributed parameter as prior information when the parameter is bounded at the range $[a, b]$.

$$\pi(m) = \begin{cases} \frac{1}{b-a}, & a \le m \le b, \\ 0, & m < a, m > b; \end{cases} \quad (3-4)$$

b) Logit normal prior: consider a logit-normal distribution for each parameter

$$\pi(m) \propto \exp\left(-\frac{1}{2}\frac{(\text{logit}(P)-\mu)^2}{\sigma_\pi^2}\right) \quad (3-5)$$

where μ and σ_π^2 are prior mean and variance, respectively, and

$$\text{logit}(P) = \log\frac{P}{1-P}, 0 \le P \le 1, \quad (3-6)$$

$$P = \frac{b-m}{b-a}, a \le m \le b; \quad (3-7)$$

c) Triangular Prior:

$$\pi(m) = \begin{cases} \frac{2(m-a)}{(b-a)(c-a)}, & a \le m \le c, \\ \frac{2(b-m)}{(b-a)(b-c)}, & c < m \le b, \\ 0, & m < a, m > b. \end{cases} \quad (3-8)$$

Lastly, the resulting posterior is then given by

$$P(\boldsymbol{m}|\boldsymbol{Q}) \propto \exp\left\{\frac{1}{2}[\boldsymbol{Q} - g(\boldsymbol{m})]^T \Sigma_e^{-1}[\boldsymbol{Q} - g(\boldsymbol{m})]\right\}\prod_{i=1}^{n}\pi(m_i) \quad (3-9)$$

Subsequently, there are two problems left: how we could get the modeled *Q*; and once knowing the posterior of targeted parameters, how we could obtain the solutions to the rock properties and their uncertainties. The next two subsections are committed to solve these two problems, respectively.

3.4.1 Rock Physics Model

The rock physics model from which we get the modeled *Q* links the intrinsic attenuation to the rock properties, such as gas saturation and porosity. It is a mathematic expression of the

seismic wave attenuation in the pore scale of rocks. For partially-saturated models, the rock is often considered as patches (White, 1975; White et al., 1975; Dvorkin and Mavko, 2006). Because the fluids in the pores or cracks will communicate when the seismic wave compresses the rock. The patchy theory conveniently discusses the equilibrium or disequilibrium of different fluids when exposed to very low- or high- frequency waves. Those models differ in their assumptions of patches. However, any model that appropriately represents the partially-saturated rock and is calibrated to the specific reservoir can be used.

In this paper, we focus on the unconsolidated sediments with partial gas saturation at Finneidfjord, Norway. Dvorkin and Mavko (2006) proposed a rock physics model simultaneously combining Q_p and Q_s, for partially gas-saturated rock under the assumption of standard linear solid (Mavko et al., 2009). They quantified the attenuation treating the partially-saturated rock as patches with different phases. The link between frequency-dependent compressional Q and the corresponding compressional moduli M is as follow (Mavko et al., 2009),

$$\frac{1}{Q} = \frac{M_\infty - M_0}{\sqrt{M_\infty M_0}} \frac{f/f_c}{1 + (f/f_c)^2} \qquad (3-10)$$

where M_0 and M_∞ are the low and high-frequency limits of the compressional moduli M, respectively; and f_c is the characteristic frequency at which the inverse Q is maximum.

$$f_c = \frac{\kappa}{{L_c}^2 \eta(\beta_p + \beta_f)} \qquad (3-11)$$

where β_p is the compressibility of the pore space (Walsh, 1965; Zimmerman, 1991)

$$\beta_p = \frac{1}{\phi}\left(\frac{1}{K_{dry}} - \frac{1}{K_m}\right) \qquad (3-12)$$

and β_f is the compressibility of the effective fluid by isostress average (Wood, 1955) of the moduli of the liquid and gaseous phases $\beta_f = S_w\beta_w + (1 - S_w)\beta_g$; η and κ are the viscosity and permeability of the effective fluid; L_c is the characteristic length, which represents the scale of the medium heterogeneity and is related to the pore and grain details.

At a very low frequency, the loading by the elastic wave is slow. The patch is "relaxed" due to the equilibrium of the pore pressure in a fully-liquid-saturated patch and partially-saturated domains next to it. Considering a rock in which $K_{\mathrm{dry}}, G_{\mathrm{dry}}$ are the bulk and shear modulus of the dry rock frame (obtained from effective medium model, see Appendix); K_m is the bulk modulus of the mineral phase; and ϕ is the total porosity, it bulk modulus at partial water saturation S_w is as follow according to Gassmann's equation (Gassmann, 1951)

$$K_{sat} = K_m \frac{\phi K_{dry} - (1+\phi) K_{fl} K_{dry}/K_m + K_{fl}}{(1-\phi) K_{fl} + \phi K_m - K_{fl} K_{dry}/K_m}, \tag{3-13}$$

$$G_{sat} = G_{dry} \tag{3-14}$$

where the fluid bulk modulus K_{fl} is the harmonic average of water modulus K_w and gas modulus K_g (Reuss, 1929):

$$K_{\infty}^{-1} = S_w K_w^{-1} + (1 - S_w) K_g^{-1}. \tag{3-15}$$

Thus, the low-frequency limit of compressional modulus

$$M_0 = K_{sat} + \frac{4}{3} G_{sat}. \tag{3-16}$$

At a very high frequency, all liquid in partially saturated rock is assumed to concentrate in fully-saturated patches and all gas stays in the other patches. The patch is "unrelaxed" because of the disequilibrium caused by oscillatory variations of pore pressure between the fully-water-saturated patch and the fully-gas-saturated patch. Then the high-frequency effective moduli M_{∞} is equal to the harmonic average of the compressional modulus of the two sorts of patches (Hill, 1963). Taking irreducible water saturation into consideration, its expression is

$$M_{\infty}^{-1} = \begin{cases} \dfrac{S_w - S_{wir}}{1 - S_{wir}} M_w^{-1} + \dfrac{1 - S_w}{1 - S_{wir}} M_g^{-1}, S_w > S_{wir} \\ M_0^{-1}, S_w \le S_{wir} \end{cases} \tag{3-17}$$

where M_w and M_g are compressional moduli of the water and gas patch, estimated from Gassmann's equation

$$M_w = \frac{4}{3} G_{dry} + K_m \frac{\phi K_{dry} - (1+\phi) K_{fl} K_{dry}/K_m + K_{fl}}{(1-\phi) K_{fl} + \phi K_m - K_{fl} K_{dry}/K_m}, \tag{3-18}$$

$$M_g = \frac{4}{3}G_{dry} + K_m \frac{\phi K_{dry} - (1+\phi)K_{fl-wir}K_{dry}/K_m + K_{fl-wir}}{(1-\phi)K_{fl-wir} + \phi K_m - K_{fl-wir}K_{dry}/K_m}, \quad (3-19)$$

where

$$K_{fl-wir} = \frac{S_{wir}}{K_w} + \frac{1-S_{wir}}{K_g}. \quad (3-20)$$

Additionally, shear-wave attenuation depends on compressional-wave attenuation of fully water-saturated sediments (Mavko et al., 2005). Assuming the reduction in both the compressional modulus and shear modulus between high-frequency and low-frequency limits are caused by the aligned defects or flaws, the shear-modulus-versus-frequency dispersion is derived from compressional-modulus-versus-frequency dispersion by Hudson's theory for crack media (Hudson, 1980, 1981).

If the material isotropy caused by the randomly-oriented defects is responsible for both the compressional and shear reduction, then the ratio of Q_s to Q_p is

$$\frac{Q_P^{-1}}{Q_S^{-1}} = \frac{1}{M/G}\left[\frac{4}{3} + \frac{5}{4}\frac{(M/G-2/3)(M/G-4/3)^2}{M/G-8/9}\right] \quad (3-21)$$

where M or G is assumed to be the geometrical average of the low and high frequency limits of the compressional or shear moduli $M = \sqrt{M_0 M_\infty}$, $G = \sqrt{G_0 G_\infty}$.

3.4.2 Sensitivity Analysis

To make sure the forward modeling is valid, and the inverse modeling is reliable, it is necessary to conduct a sensitivity analysis. By using the attenuation model of Dvorkin and Mavko (2006), the summary of the input parameters $\boldsymbol{m}$ is below, and their appropriate boundaries and prior values are in Table **3-1**.

$$\boldsymbol{m} = \{S_w, S_{wir}, K_m, G_m, \eta_g, \eta_w, \phi, \phi_c, P_p, P_d, T, gg, f, \kappa, L_c\}. \quad (3-22)$$

where S_w, S_{wir} represents the water and irreducible water saturation in the rock; K_m, G_m are the bulk and shear moduli of the solid phase of the rock; the viscosity is denoted as η; pore pressure

and differential pressure (difference between the pore pressure and the overburden pressure) are denoted as P_p and P_d; the temperature, gas gravity, frequency, permeability and characteristic size are T, gg, f, κ, L_c, respectively. Please note that the characteristic size is a measurement of the rock heterogeneity. Knowing it is important in discussing a frequency dependent rock physics model. It can be used to calculate the resonance frequency of rocks. Because the frequency of given data is fixed and easily calculated, we do not take the frequency into consideration when conducting the sensitivity analysis but set it as a normal seismic frequency 50 Hz. The other parameter ranges that we use are as Table **3-1**. After global sensitivity analysis (Saltelli et al., 2010) of each parameter to the rock physics model (Figure 3-4), the P-wave quality factor is the most responsive to saturation, porosity, bulk and shear moduli, rock permeability, and characteristic size; and it slightly reacts to water viscosity and differential pressure. Summarily, six parameters $\{S_w, \phi, K_m, G_m, \kappa, Lc\}$ have the potential to be reliably estimated by this joint Q_p and Q_s attenuation model considering their sensitivities. On the other hand, mathematically, it is possible to invert any two of the six parameters according to the data available.

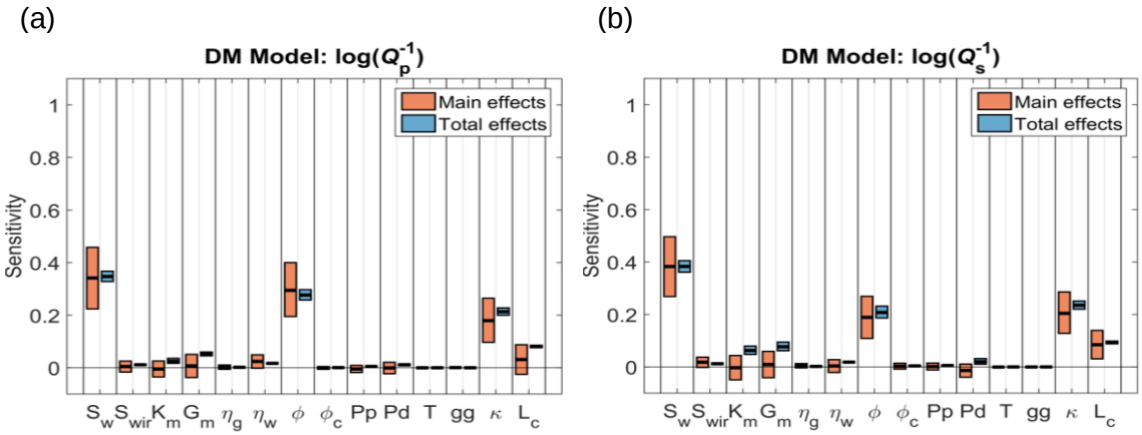

Figure 3-4. Sensitivity indices for Dvorkin-Mavko Model: a. log(Q_p^{-1}); b. log(Q_s^{-1}). Main and total effects are two different kinds of indices representing the extent of parameter sensitivities to the DM model.

Table 3-1. Initial Parameter Values and Bounds, Finneidfjord, Norway

Parameters	Bounds	Initial Value
Gas Saturation S_g (%)	0~1	0.2[a]
Irreducible Water Saturation S_{wir}	0.00~0.40	0.11[b]
Porosity ϕ	0.35~0.70[c]	0.58[c]
Critical Porosity ϕ_c	0.36~0.4[d]	0.38
Solid Grain Bulk Moduli K_m (GPa)	20~70[e]	25[e, f]
Solid Grain Shear Moduli G_m (GPa)	5~50[e]	9[e, f]
Gas Specific Gravity gg	0.56	0.56[e]
Pore Pressure P_p (MPa)	0.55~2.93	0.77[a]
Differential Pressure P_d (MPa)	0~100[c]	80[c]
Gas Viscosity η_g (10^{-3}Pa·s)	0.1~0.2[g]	0.15[g]
Water Viscosity η_w (10^{-3}Pa·s)	1~5[g]	3[g]
Intrinsic Permeability κ (mD)	15~150[c]	35[c]
Temperature T (^{o}C)	5~7[c]	6[c]
Characteristic size L_c (mm)	0.001~2[h, f, i]	0.25[f, i]

[a]Morgan et al. (2012); [b]Polak et al. (2004); [c]Leynaud et al. (2007); [d]Nur et al. (1998); [e]Mavko et al. (2009); [f]Vanneste et al.(2012; 2013a); [g]Carcione and Picotti (2006); [h]Dvorkin and Nur (1993); [i]Vardy et al. (2012)

3.4.3 Markov-Chain Monte Carlo Sampling

Having the distribution of posterior, the next step is to solve the second problem. A robust and straightforward method for computing the samples from the posterior $\pi(\boldsymbol{m}|\boldsymbol{Q})$ is the Markov-Chain Monte Carlo algorithm (MCMC) (Metropolis et al., 1953; Hastings, 1970). There are a lot of MCMC algorithms for updating schemes. But all of them are special cases of Metropolis-Hastings. For instance, the multivariate updating scheme (Gelman et al., 1996; Tierney, 1994) was derived from single-site MCMC (Metropolis et al, 1953); Ter Braak (2006) proposed a Differential Evolution-MCMC; and Fox and Nicholls (1997) use a fast and approximate simulator to develop a delayed acceptance approach.

The Differential Evolution-MCMC is an effective approach to explore the posterior avoiding the difficulty in determining the updating step size. The scheme is as following pseudocodes (Figure 3-5). Assuming vector $\boldsymbol{x}^p$ denotes the m parameters at chain p, in DE-

MCMC, a collection of independent chains $\{\boldsymbol{x}^1, \ldots, \boldsymbol{x}^p, \ldots, \boldsymbol{x}^P\}$ is initialized according to the prior information. The chain $\boldsymbol{x}^p$ is updated according to a multivariate Metropolis step. In the original implementation, σ is chosen quite small that the new proposal $\boldsymbol{x}' = \boldsymbol{x} + \boldsymbol{e}$ would be always accepted. The acceptance rate is mainly controlled by γ at around 44% for each iteration (Ter Braak, 2006).

There are two noticeable points before performing DE-MCMC. Firstly, as mentioned before, measured $\boldsymbol{Q}$ or modeled $g(\boldsymbol{m})$ is supposed to be normalized by a logarithm operator, because the scaled *Q* is more sensitive to those parameters as shown in sensitivity analysis (Figure 3-4). Secondly, random walk sampling in MCMC requires unbounded variables. The parameters $\boldsymbol{m}$, nevertheless, are always bounded in an appropriate range (Table **3-1**) according to geologic information. Subsequently, we take the logit transformation (equation 3 - 6, 3 - 7) before performing DE-MCMC for each variable and then take the inverse logit transformation for the sampled chain to restore the values as final results.

1: Initialize *P* copies $\{\boldsymbol{x}^1, \ldots, \boldsymbol{x}^p, \ldots, \boldsymbol{x}^P\}$
2: **for** $k = 1$ *: niter* **do**
3: **for** $p = 1$ *: P* **do**
4: Choose indices *q* and *r* without replacement from
5: $\{1, \ldots, p-1, p+1, \ldots, P\}$
6: $\boldsymbol{x}^{p\,\prime} = \boldsymbol{x}^p + \gamma(\boldsymbol{x}^q - \boldsymbol{x}^r) + \boldsymbol{e}$, where $\boldsymbol{e} \sim N(0, \sigma^2 \boldsymbol{I}_n)$
7: **if** $u < \pi(\boldsymbol{x}^{p\,\prime}|y)/\pi(\boldsymbol{x}^p|y)$ **then**
8: $\boldsymbol{x}^p = \boldsymbol{x}^{p\,\prime}$
9: **end if**
10: **end for**
11: **end for**

Figure 3-5. Pseudocode for DE-MCMC (Brooks et al., 2011)

3.5 Result

As a crude estimation, getting rid of some possibly determined parameters might cut down the ambiguity of the inversion. Specifically, in the pool of effective parameters of the attenuation model, moduli could be determined by the information of the lithology. In terms of Finneidfjord case, the main composition of sediments in the target layer is silt clay. The bulk modulus K_m = 25 GPa and shear modulus G_m = 9 GPa for silt clay (Mavko et al., 2009); the dominant frequency could be estimated from the seismic data by spectral analysis, $f_d \approx$ 200 Hz for the OBS data at Fineidfjord; and the permeability is reported as 35 mD by Leynaud et al. (2007). The last parameter, characteristic size L_c, is poorly determined but related to the details of pores and grains. It could be guessed at the same order of magnitude as the average grain size or the average crack length (Mavko, et al., 2009). Vardy (2012) analyzed the grain size and *Q* relation.

Now there are three parameters left: saturation, porosity, and pore pressure. For convenience, we set the pore pressure P_p = 0.77 MPa (Morgan et al., 2012), and only discuss the inversion for saturation and porosity. Even if the pore pressure is not an accurate prior, it does not have too much effect on the inversion because of its low sensitivity index. The final results are showed below.

The Figure 3-6 is the results of DE-MCMC. It is obvious that the Markov chain converges at S_w less than 1% and ϕ around 0.5. The medians of S_g and ϕ are 0.53% ± 0.186% and 0.50 ± 0.044, respectively. The prior constrains the likelihood according to the prior mean and variance. In case of too strongly shaping the likelihood, a large variance of the prior is necessary to make sure the likelihood dominates in the posterior. The estimated results agree with the previous research on Fineidjord area, in which S_g < 1% (Morgan, et al., 2012) and $\phi \approx$ 58% (Leynaud et al. 2007; Hustoft et al., 2009). The S_g from this inversion is informative and reasonably accurate.

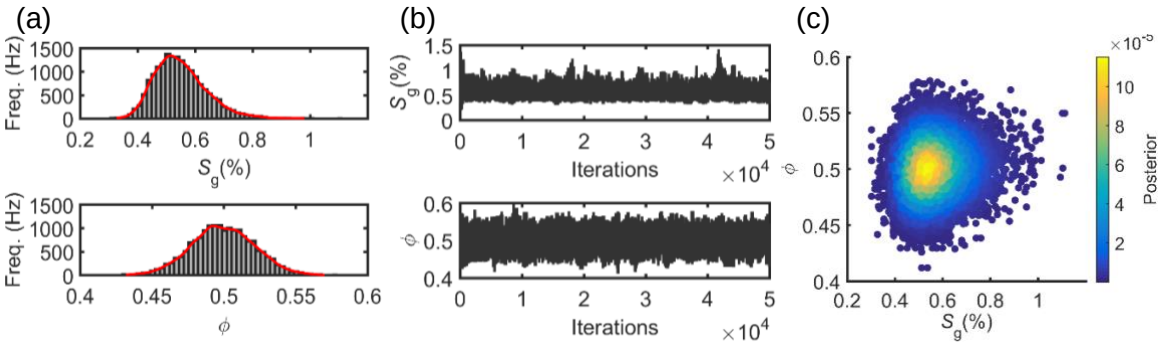

Figure 3-6. The performance of DE-MCMC on the joint Q_p and Q_s inversion for Fineidfjord OBS data. a) estimated gas saturation and porosity distributions; b) evolution of the chain during MCMC sampling; c) crossplot of estimated porosity and gas saturation with their posterior probability (color). The average acceptance rate of MCMC is 43%.

3.6 Discussion

The joint Bayesian inversion workflow is presented, which can be used for different rock physics models under different reservoir conditions such as shale gas reservoir or CO_2 sequestration, as long as the gas-induced seismic intrinsic attenuation is significant enough. The complexity of solving the inverse problem is handled by the stochastic algorithm. The main advantages of this method are: the error in equation 3-9 includes the uncertainty of both modeling and measuring and is considered into the final estimation; Q_s enhances the model sensitivity, making it possible to more reliably estimate the targeted parameters; the one more additional dimension of information Q_s and the prior reduce the ambiguity of the two-variable inverse problem in solving gas saturation and porosity; DE-MCMC scheme aims at walking along with a most-likely way to converge to optimal solutions with adaptive steps, thus saving a lot of computation time, especially compared with numerical integration method as discussed in the following subsection 3.6.2; it is promising to map the rock properties of potential gas configuration only if we can transform the seismic cube to instantaneous Q cube.

3.6.1 Ambiguity

Although the shear wave information reduces the ambiguity of the two-variable inverse problem, the multi-solutions caused by the nonlinearity of the model are still existent. Figure 3-7 showed the numerical test for Dvorkin-Mavko model. We change S_w and ϕ within their bounds in a step to exhaustively calculate the modeled Q_p. It is obvious that the relationship between attenuation and parameters S_w and ϕ is nonlinear. Conversely, given a modeled Q_p, the number of corresponding solutions of saturation and porosity are infinite. The projection of the solutions in the plane of saturation and porosity will be roughly an ellipse (Figure 3-8). By adding Q_s, we have

one more ellipse and the final solutions should be the intersection points *A* and *B* of those two circles, which enormously mitigates the ambiguity from an infinite number of solutions into two solutions. The residual ambiguity would be further suppressed by constraints or the prior information, thus we can have the final solution (Figure 3-10).

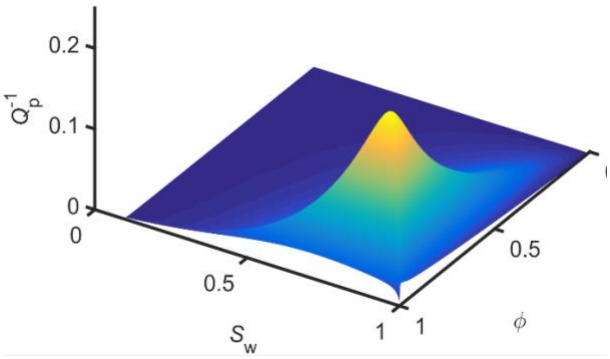

Figure 3-7. Numerical test for Dvorkin-Mavko model.

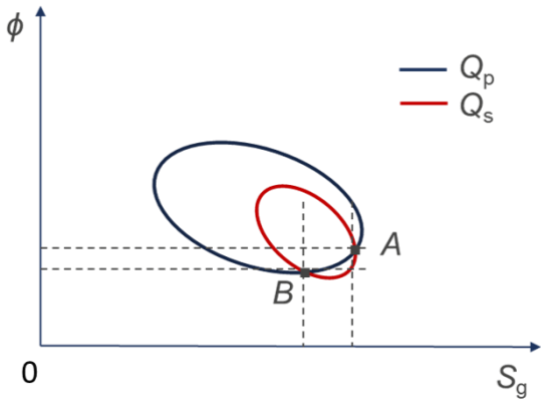

Figure 3-8. Schematic diagram of ambiguity caused by nonlinearity.

3.6.2 Numerical Integration

Another way of solving the parameters from posterior is numerical integration. As we know, we could get the best estimation and its variance from marginal distribution. The marginal distribution can be calculated from integration of joint distribution with respect to each parameter. In Figure 3-9, we plot the joint distribution of prior, likelihood and posterior by inputting grid values of S_g and ϕ based on their bounds into the Bayesian model (equation 3-9). In the likelihood, there are two modes resulting from nonlinearity of the rock physics model. From Figure 3-10, firstly, we can see that there is only one solution to porosity because the relationship between attenuation and porosity is monotonic within the given bounds. Secondly, even though the likelihood is multi-mode, the posterior is single mode for saturation after introducing the prior. The prior is a multivariate logit-normal distribution with mean S_g = 0.2%, ϕ = 0.58, which come from reports or papers (Morgan et al., 2012; Leynaud et al., 2007) on this area. The variance of the prior

controls the weight of the prior in the posterior, which should be chosen according to the reliability of the prior information. Here we take 1.5.

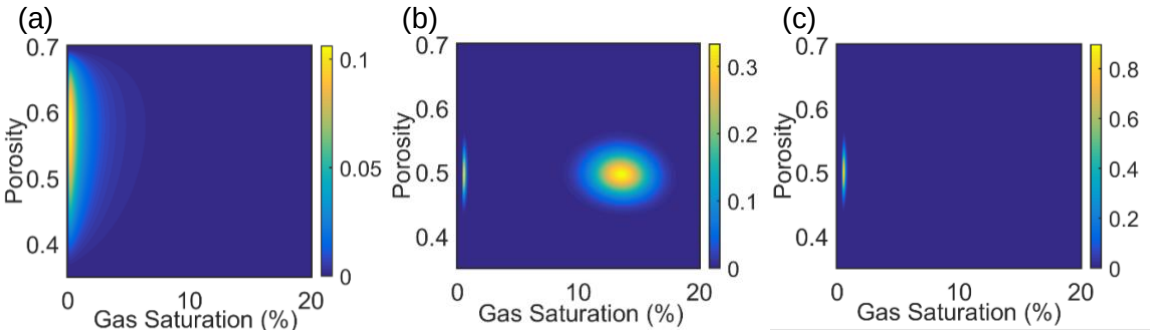

Figure 3-9. The joint probability-density distribution of porosity and water saturation. Colors represent the probability of a) prior, b) likelihood, c) posterior. The posterior is equal to the likelihood times prior.

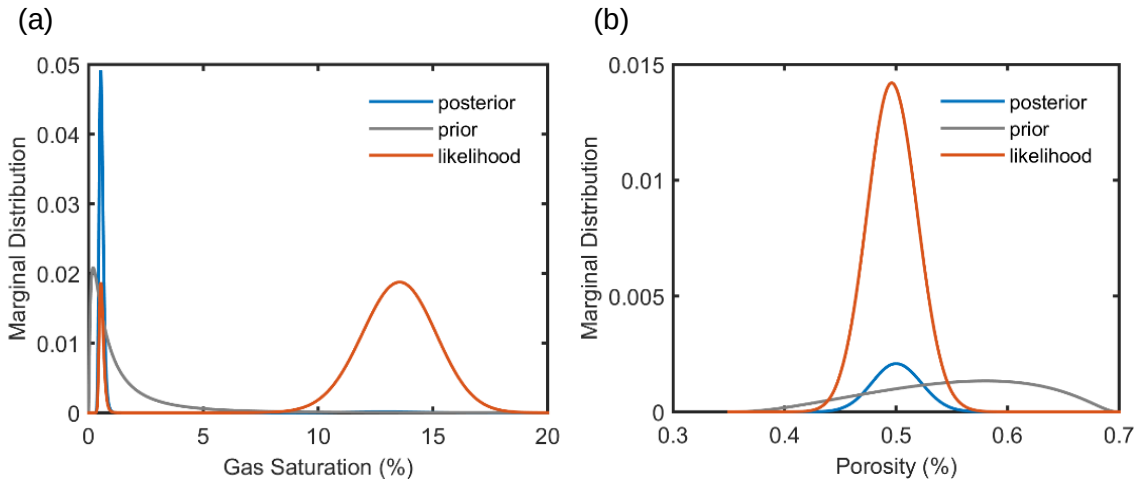

Figure 3-10. Marginal distribution of gas (a) saturation and (b) porosity

The results from numerical integration are S_g = 0.53% ± 0.090%, ϕ = 0.50 ± 0.001. Although they are almost the same as results from MCMC, the computation efficiency is different, especially when dealing with much more parameter inversion. For my code, it takes 1.5 ms to perform one-time iteration. There is not much difference in computational consumption for this example. However, it would spend 72 hours to integrate a four-parameter grid of 100×100×100×100, while by MCMC it only takes 2.5 min to perform 1,000,000 iterations which are enough to converge. So, the posterior integration method is less efficient than the MCMC method.

3.6.3 Problem Determinability

Mathematically, the number of independent information determines how many unknowns we can solve. Our method is open to add more information, thus to estimate more parameters. For example, Q_p or Q_s measured from sonic logs is independent information since they are in different frequency scales (Figure 3-11). The two more dimensions of information would further constrain the model and it might extend the two-variable inverse problem to a four-variable inverse problem. It will be shown in the next chapter.

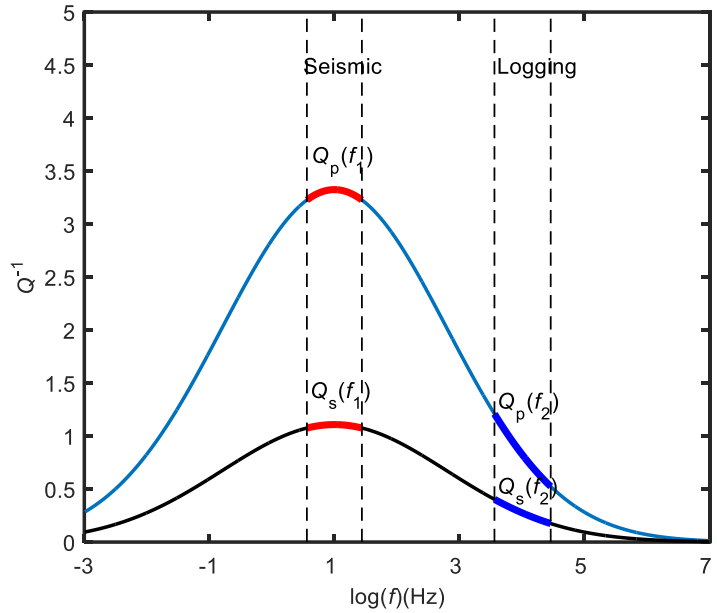

Figure 3-11. Schematic diagram for Q_p, Q_s in different frequencies. The four dimensions of information would be obtained from seismic data and log data.

3.7 Conclusion

We present a Bayesian inversion workflow combing the Q_p and Q_s information to assess gas saturation and porosity. This attenuation-based approach is different from traditional velocity-based inversion. Compared to velocity, the attenuation responses much more strongly to saturation. Dvorkin-Mavko model is capable of simulating P- and S- wave seismic attenuation simultaneously in terms of various gas and sediment properties. After global sensitivity analysis, the efficacy of saturation and porosity estimation through attenuation inversion is validated. The ambiguity could be mitigated by adding more information into the model, further constraining the parameters, or imposing prior information on the specific parameters. Additionally, the Bayesian approach, as a powerful tool to solve the nonlinear inverse problem, is implemented on the Dvorkin-Mavko model. The Differential-Evolution MCMC scheme performs well in this case when sampling the target variables. The estimated gas saturation and porosity are in good agreement with the historical research. The biggest advantage of stochastic inversion is that we cannot only estimate the unknowns (median or mean), but also know the uncertainties of the estimation (posterior distribution).

3.8 Appendix

3.8.1 Quality Factor (Mavko et al., 2009)

Assuming a standard linear solid, there would be an expression as

$$\eta\dot{\sigma}_{ij} + (E_1 + E_2)\sigma_{ij} = E_2\left(\eta\dot{\varepsilon}_{ij}\right) \qquad (A-1)$$

where E_1 and E_2 are elastic moduli, ε and σ are stress and strain, and η is a material constant resembling viscosity.

Mathematically, the quality factor is the ratio of the imaginary and real parts of the complex modulus

$$\frac{1}{Q} = \frac{M_I}{M_R}. \qquad (A-2)$$

If we assume sinusoidal motion

$$\varepsilon = \varepsilon_0 e^{i\omega t} \qquad (A-3)$$

$$\sigma = \sigma_0\, e^{i\omega t} \qquad (A-4)$$

and substitute into equation A - 1

$$\sigma_0 = M(\omega)\varepsilon_0. \qquad (A-5)$$

The complex frequency-dependent modulus is

$$M(\omega) = \frac{E_2(E_1 + i\omega\eta)}{(E_1 + E_2 + i\omega\eta)}. \qquad (A-6)$$

In the limits of the low frequency and the high frequency, the limit moduli are

$$M_0 = \frac{E_2E_1}{E_1 + E_2}, \omega \to 0 \qquad (A-7)$$

$$M_\infty = E_2, \omega \to \infty. \qquad (A-8)$$

Please note that at very low and very high frequencies the moduli are real and independent of frequency, and thus in these limits the material behaves elastically. Rewrite the complex modulus in terms of those limits:

$$M(\omega) = \frac{M_\infty \left[M_0 + i\frac{\omega}{\omega_c}(M_\infty M_0)^{1/2}\right]}{\left(M_\infty + i\frac{\omega}{\omega_c}(M_\infty M_0)^{1/2}\right)} \quad (\mathrm{A}-9)$$

and

$$Re[M(\omega)] = \frac{M_0 M_\infty [1 + (\omega/\omega_c)^2]}{M_\infty + (\omega/\omega_c)^2 M_0} \quad (\mathrm{A}-10)$$

$$Im[M(\omega)] = \frac{(\omega/\omega_c)\sqrt{M_\infty M_0}(M_\infty - M_0)}{M_\infty + (\omega/\omega_c)^2 M_0} \quad (\mathrm{A}-11)$$

where ω_c is the material resonance frequency

$$\omega_c = \frac{\sqrt{\left(E_1(E_1+E_2)\right)}}{\eta}. \quad (\mathrm{A}-12)$$

The quality factor is the ratio of the imaginary and real parts of the complex moduli:

$$\frac{1}{Q} = \frac{M_I(\omega)}{M_R(\omega)}, \quad (A-13)$$

$$\frac{1}{Q} = \frac{M_\infty - \mathrm{M}_0}{\sqrt{M_\infty \mathrm{M}_0}} \frac{\omega/\omega_c}{1+(\omega/\omega_c)^2} = \frac{E_2}{\sqrt{E_1(E_1+E_2)}} \frac{\omega/\omega_c}{1+(\omega/\omega_c)^2}; \quad (\mathrm{A}-14)$$

thus, it is related to the very high and very low frequencies.

3.8.2 Effective Medium Model

The effective medium model estimates the mixture modulus of the dry frame, connecting the three endpoints in the modulus-porosity plane, one at zero porosity, another at critical porosity, and the last at 100% porosity of zero rigidity.

At critical porosity, the effective bulk K_{HM} and shear G_{HM} moduli of the dry pack are given by the Hertz-Mindlin (Mindlin and Deresiewicz, 1949)contact theory:

$$K_{HM} = \left[\frac{n^2(1-\phi_c)^2}{18\pi^2(1-\nu)^2}P\right]^{\frac{1}{3}} \quad (A-15)$$

$$G_{HM} = \frac{5-4\nu}{5(2-\nu)}\left[\frac{3n^2(1-\phi_c)^2}{2\pi(1-\nu)^2}P\right] = \frac{1}{3} \quad (A-16)$$

where P is the effective pressure; K, G are bulk and shear moduli of the solid phase, and ν is Poisson's ratio; n is the average number of the contacts per grain in the sphere pack, which is empirically related to porosity by (García and Medina, 2006; Makse et al., 2004)

$$n = n_0 + 9.7(\phi + \phi)^{0.48}, n_0 = 4.46, \phi = 0.384. \quad (A-17)$$

At the porosity below critical, the dry frame bulk moduli between two endpoints, the pure solid phase and the phase of the sphere pack, in the porosity-moduli plane can be mathematically expressed as

$$K_{dry} = \left[\frac{\phi/\phi_c}{K_{HM} + \frac{4}{3}G_{HM}} + \frac{1-\phi/\phi_c}{K + \frac{4}{3}G_{HM}}\right]^{-1} - \frac{4}{3}G_{HM}, \quad (A-18)$$

$$G_{dry} = \left[\frac{\phi/\phi_c}{G_{HM} + Z} + \frac{1-\phi/\phi_c}{G + Z}\right]^{-1} - Z, \quad (A-19)$$

$$Z = \frac{G_{HM}}{6}\left(\frac{9K_{HM} + 8G_{HM}}{K_{HM} + 2G_{HM}}\right). \quad (A-20)$$

At porosity above critical, the connection is established between the sphere pack and the void of zero rigidity. Then the effective dry-frame moduli are:

$$K_{dry} = \left[\frac{(1-\phi)/(1-\phi_c)}{K_{HM} + \frac{4}{3}G_{HM}} + \frac{(\phi-\phi_c)/(1-\phi_c)}{\frac{4}{3}G_{HM}}\right]^{-1} - \frac{4}{3}G_{HM}, \quad (A-21)$$

$$G_{dry} = \left[\frac{(1-\phi)/(1-\phi_c)}{G_{HM} + Z} + \frac{(\phi-\phi_c)/(1-\phi_c)}{Z}\right]^{-1} - Z, \quad (A-22)$$

$$Z = \frac{G_{HM}}{6}\left(\frac{9K_{HM} + 8G_{HM}}{K_{HM} + 2G_{HM}}\right). \quad (A-23)$$

Lastly, the bulk moduli K_{sat} and shear moduli G_{sat} can be calculated by Gassmann's equations (equation 3 - 13, 3 - 14).

3.9 References

Barnes, C., Cergy-pontoise, U. De, Charara, M., Williamson, P., 2014. P & S wave attenuation effects on full-waveform inversion for marine seismic data 949–953.

Batzle, M., Hofmann, R., Prasad, M., Duranti, L., Han, D., 2005. Seismic Attenuation: Observations and Mechanisms, in: SEG/Houston 2005 Annual Meeting. pp. 2003–2006.

Biot, M.A., 1956b. Theory of Propagation of Elastic Waves in a Fluid-Saturated Porous Solid. I. Lower Frequency Range. J. Acoust. Soc. Am. doi:10.1121/1.1908241

Biot, M.A., 1956a. Theory of Propagation of Elastic Waves in a Fluid‐Saturated Porous Solid. II. Higher Frequency Range. J. Acoust. Soc. Am. 28, 168–178. doi:10.1121/1.1908241

Bosch, M., Mukerji, T., Gonzalez, E.F., 2010. Seismic inversion for reservoir properties combining statistical rock physics and geostatistics: A review. GEOPHYSICS 75, 75A165-75A176. doi:10.1190/1.3478209

Brooks, S., Gelman, A., Jones, G., Meng, X.-L., 2011. Handbook of Markov chain Monte Carlo. CRC Press/Taylor & Francis.

Buland, A., El Ouair, Y., 2006. Bayesian time-lapse inversion. GEOPHYSICS 71, R43–R48. doi:10.1190/1.2196874

Buland, A., Omre, H., 2003. Bayesian linearized AVO inversion. GEOPHYSICS 68, 185–198. doi:10.1190/1.1543206

Carcione, J.M., Picotti, S., 2006. P-wave seismic attenuation by slow-wave diffusion: Effects of inhomogeneous rock properties. Geophysics 71, 01–08.

Carcione, J.M., Picotti, S., Gei, D., Rossi, G., 2006. Physics and Seismic Modeling for Monitoring CO2 Storage. Pure Appl. Geophys. 163, 175–207. doi:10.1007/s00024-005-0002-1

Cary, P.W., Chapman, C.H., 1988. Automatic 1-D waveform inversion of marine seismic refraction data. Geophys. J. Int. 93, 527–546. doi:10.1111/j.1365-246X.1988.tb03879.x

Chadwick, R.A., Arts, R., Eiken, O., 2005. 4D seismic quantification of a growing CO2 plume at Sleipner, North Sea, in: Petroleum Geology: North-West Europe and Global Perspectives – Proceedings of the 6th Petroleum Geology Conference. Geological Society of London, pp. 1385–1399. doi:10.1144/0061385

Daley, T.M., Ajo-Franklin, J.B., Doughty, C., 2011. Constraining the reservoir model of an injected CO2 plume with crosswell CASSM at the Frio-II brine pilot. Int. J. Greenh. Gas Control 5, 1022–1030. doi:10.1016/J.IJGGC.2011.03.002

Dickens, G.R., Paull, C.K., Wallace, P., 1997. Direct measurement of in situ methane quantities in a large gas-hydrate reservoir. Nature 385, 426–428. doi:10.1038/385426a0

Doyen, P., 2007. Seismic reservoir characterization: an earth modelling perspective, Education tour series. EAGE publications.

Dvorkin, J., Mavko, G., 2006. Modeling attenuation in reservoir and nonreservoir rock. Lead. Edge 25, 194. doi:10.1190/1.2172312

Dvorkin, J., Nur, A., 1993. Dynamic poroelasticity: A unified model with the squirt and the Biot mechanisms. Geophysics 58, 524. doi:10.1190/1.1443435

Ecker, C., Dvorkin, J., Nur, A.M., 2000. Estimating the amount of gas hydrate and free gas from marine seismic data. Geophysics 65, 565. doi:10.1190/1.1444752

Fox, C., Nicholls, G., 1997. Sampling Conductivity Images via MCMC. Leeds Annu. Stat. Work. 91--100.

García, X., Medina, E.A., 2006. Hysteresis effects studied by numerical simulations: Cyclic loading-unloading of a realistic sand model. GEOPHYSICS 71, F13–F20. doi:10.1190/1.2181309

Gassmann, F., 1951. Über die Elastizität poröser Medien, Vier. Der Natur.

Gelman, A., Carlin, J.B., Stern, H.S., Rubin, D.B., 2004. Bayesian Data Analysis. Texts in Statistical Science.

Gelman, A., Roberts, G.O., Gilks, W.R., 1996. Efficient Metropolis Jumping Rules 599–607.

Gouveia, W.P., Scales, J.A., 1998. Bayesian seismic waveform inversion: Parameter estimation and uncertainty analysis. J. Geophys. Res. Solid Earth 103, 2759–2779. doi:10.1029/97JB02933

Grana, D., Mukerji, T., 2015. Bayesian inversion of time-lapse seismic data for the estimation of static reservoir properties and dynamic property changes. Geophys. Prospect. 63, 637–655. doi:10.1111/1365-2478.12203

Hackert, C.L., Parra, J.O., 2004. Improving Q estimates from seismic reflection data using well-log-based localized spectral correction. Geophysics 69, 1521. doi:10.1190/1.1836825

Hastings, W.K., 1970. Monte Carlo sampling methods using Markov chains and their applications. Biometrika 57, 97–109.

Hill, R., 1963. Elastic properties of reinforced solids: Some theoretical principles. J. Mech. Phys. Solids 11, 357–372. doi:http://dx.doi.org/10.1016/0022-5096(63)90036-X

Holbrook, W.S., Hoskins, H., Wood, W.T., Stephen, R. a, Lizarralde, D., 1996. Methane Hydrate and Free Gas on the Blake Ridge from Vertical Seismic Profiling. Science (80-.). 273, 1840–1843. doi:10.1126/science.273.5283.1840

Hudson, J. a. A., 1981. Wave speeds and attenuation of elastic waves in material containing cracks. Geophys. J. R. Astron. Soc. 64, 133–150. doi:10.1111/j.1365-246X.1981.tb02662.x

Hudson, J.A., 1980. Overall properties of a cracked solid. Math. Proc. Cambridge Philos. Soc. 88, 371–384. doi:10.1017/S0305004100057674

Hustoft, S., Dugan, B., Mienert, J., 2009. Effects of rapid sedimentation on developing the Nyegga pockmark field: Constraints from hydrological modeling and 3-D seismic data, offshore mid-Norway. Geochemistry, Geophys. Geosystems 10, n/a-n/a. doi:10.1029/2009GC002409

Jackson, D.D., Anderson, D.L., 1970. Physical mechanisms of seismic-wave attenuation. Rev. Geophys. 8, 1. doi:10.1029/RG008i001p00001

Karl, J.H., 1989. 8 - Digital Filter Design, in: Karl, J.H. (Ed.), Introduction to Digital Signal Processing. Academic Press, San Diego, pp. 165–196. doi:http://dx.doi.org/10.1016/B978-0-12-398420-3.50012-6

Klimentos, T., 1995. Attenuation of P- and S- waves as a method of distinguish gas and condensate from oil and water. Geophysics 60, 447–458.

Lei, X., Morgan, E.C., 2016. A comparison of methods for estimating Q, in: SEG Technical Program Expanded Abstracts 2016. Society of Exploration Geophysicists, pp. 3021–3025. doi:10.1190/segam2016-13971809.1

Lei, X., Xue, Z., 2009. Ultrasonic velocity and attenuation during CO2 injection into water-saturated porous sandstone: Measurements using difference seismic tomography. Phys. Earth Planet. Inter. 176, 224–234. doi:10.1016/j.pepi.2009.06.001

Leynaud, D., Sultan, N., Mienert, J., 2007. The role of sedimentation rate and permeability in the slope stability of the formerly glaciated Norwegian continental margin: the Storegga slide model. Landslides 4, 297–309. doi:10.1007/s10346-007-0086-z

Lu, S., McMechan, G. a., 2002. Estimation of gas hydrate and free gas saturation, concentration, and distribution from seismic data. Geophysics 67, 582. doi:10.1190/1.1468619

Makse, H.A., Gland, N., Johnson, D.L., Schwartz, L., 2004. Granular packings: Nonlinear elasticity, sound propagation, and collective relaxation dynamics. Phys. Rev. E 70. doi:10.1103/PhysRevE.70.061302

Mavko, G., Dvorkin, J., Walls, J., 2005. A theoretical estimate of S‐wave attenuation in sediment, in: SEG Technical Program Expanded Abstracts 2005. Society of Exploration Geophysicists, pp. 1469–1472. doi:10.1190/1.2147967

Mavko, G., Nur, A., 1979. Wave attenuation in partially saturated rocks. Geophysics 44, 161–178.

Mavko, G., Tapan, M., Dvorkin, J., 2009. The Rock Physics Handbook: Tools for seismic analysisin porous media, Second Edi. ed. Cambridge University Press, New York.

Menke, W., 1984. Geophysical data analysis : discrete inverse theory. Academic Press.

Metropolis, N., Rosenbluth, A.W., Rosenbluth, M.N., Teller, A.H., Teller, E., 1953. Equation of State Calculations by Fast Computing Machines. J. Chem. Phys. 21, 1087–1092. doi:doi:10.1063/1.1699114

Mindlin, R.D., Deresiewicz, H., 1949. Compliance of Elastic Bodies in Contact. J. Appl. Mech. 16, 327.

Morgan, E., Vanneste, M., Vardy, M., 2014. Characterization of the Slope-destabilizing Effects of Gas-charged Sedi- ment via Seismic Surveys 2.

Morgan, E.C., Vanneste, M., Lecomte, I., Baise, L.G., Longva, O., McAdoo, B., 2012. Estimation of free gas saturation from seismic reflection surveys by the genetic algorithm inversion of a P-wave attenuation model. Geophysics 77, R175. doi:10.1190/geo2011-0291.1

Müller, T.M., Gurevich, B., Lebedev, M., 2010. Seismic wave attenuation and dispersion resulting from wave-induced flow in porous rocks — A review. Geophysics 75, 75A147. doi:10.1190/1.3463417

Nur, A., Mavko, G., Dvorkin, J., Galmudi, D., 1998. Critical porosity: A key to relating physical properties to porosity in rocks. Lead. Edge 17, 357–362. doi:10.1190/1.1437977

O'Connell, R.J., Budiansky, B., 1974. Seismic velocities in dry and saturated cracked solids. J. Geophys. Res. 79, 5412–5426. doi:10.1029/JB079i035p05412

Oldenburg, D.W., Scheuer, T., Levy, S., 1983. Recovery of the acoustic impedance from reflection seismograms. GEOPHYSICS 48, 1318–1337. doi:10.1190/1.1441413

Oliver, D.S., Liu, N., Reynolds, A.C., 2008. Inverse theory for petroleum reservoir characterization and history matching. Cambridge University Press.

Parker, R.L. (Robert L., 1994. Geophysical inverse theory. Princeton University Press.

Pinson, L.J.W.W., Henstock, T.J., Dix, J.K., Bull, J.M., 2008. Estimating quality factor and mean grain size of sediments from high-resolution marine seismic data. Geophysics 73, G19–G28. doi:10.1190/1.2937171

Polak, S., Lundin, E., Zweigel, P., Bøe, R., Lindeberg, E., Olesen, O., 2004. Storage potential for CO2 in the Frohavet Basin, Mid-Norway. Trondheim.

Pride, S.R., Berryman, J.G., Harris, J.M., 2004. Seismic attenuation due to wave-induced flow. J. Geophys. Res. 109, 1–19. doi:10.1029/2003JB002639

Quan, Y., Harris, M.J., 1997. Seismic attenuation tomography using the frequency shift method. Geophysics 62, 895. doi:10.1190/1.1444197

Raji, W.O., Rietbrock, a., 2012. The use of seismic attenuation for monitoring saturation in hydrocarbon reservoirs. SEG Tech. Progr. Expand. Abstr. 2012 1–6. doi:10.1190/segam2012-0309.1

Reuss, A., 1929. Berechnung der Fließgrenze von Mischkristallen auf Grund der Plastizitätsbedingung für Einkristalle . ZAMM - J. Appl. Math. Mech. / Zeitschrift für Angew. Math. und Mech. 9, 49–58. doi:10.1002/zamm.19290090104

Russell, B., Hampson, D., 1991. Comparison of poststack seismic inversion methods, in: SEG Technical Program Expanded Abstracts 1991. Society of Exploration Geophysicists, pp. 876–878. doi:10.1190/1.1888870

Russell, B.H., 1988. Introduction to Seismic Inversion Methods. Society of Exploration Geophysicists. doi:10.1190/1.9781560802303

Saltelli, A., Annoni, P., Azzini, I., Campolongo, F., Ratto, M., Tarantola, S., 2010. Variance based sensitivity analysis of model output. Design and estimator for the total sensitivity index. Comput. Phys. Commun. 181, 259–270. doi:10.1016/j.cpc.2009.09.018

Sen, M.K., Stoffa, P.L., 1992. Rapid sampling of model space using genetic algorithms: examples from seismic waveform inversion. Geophys. J. Int. 108, 281–292. doi:10.1111/j.1365-246X.1992.tb00857.x

Singleton, S., Images, R.S., 2007. The use of Seismic Attenuation and Simultaneous Impedance Inversion in Geophysical Reservoir Characterization SEG / San Antonio 2007 Annual Meeting SEG / San Antonio 2007 Annual Meeting 1422–1426.

Stoll, R.D., Bryan, G.M., 1970. Wave Attenuation in Saturated Sediments. J. Acoust. Soc. Am. 47.

Tarantola, A., 1987. Inverse problem theory : methods for data fitting and model parameter estimation. Elsevier.

Ter Braak, C.J.F., 2006. A Markov Chain Monte Carlo version of the genetic algorithm Differential Evolution: Easy Bayesian computing for real parameter spaces. Stat. Comput. 16, 239–249. doi:10.1007/s11222-006-8769-1

Tierney, L., 1994. Markov Chains for Exploring Posterior Distributions. Ann. Stat. 22, 1701–1762. doi:10.1214/aos/1176325750

Tinivella, U., Lodolo, E., 2000. Blake Ridge Bottom-Simulating Reflector Transect: Tomographic Velocity Field and Theoretical Model To Estimate Methane, in: Proc. ODP, Scientific Results. pp. 273–281.

Tu, N., Lu, W., 2010. Improve Q estimates with spectrum correction based on seismic wavelet estimation. Appl. Geophys. 7, 217–228. doi:10.1007/s11770-010-0252-2

Vanneste, M., Forsberg, C.F., Glimsdal, S., Harbitz, C.B., Issler, D., Kvalstad, T.J., Løvholt, F., Nadim, F., 2013a. Submarine Landslides and Their Consequences: What Do We Know, What Can We Do?, in: Landslide Science and Practice. Springer Berlin Heidelberg, Berlin, Heidelberg, pp. 5–17. doi:10.1007/978-3-642-31427-8_1

Vanneste, M., Geotechnical, N., Longva, O., Survey, G., Morgan, E., Forsberg, C.F., Kvalstad, T.J., Strout, J.M., Brendryen, J., Haflidason, H., Norsar, I.L., 2013b. Finneidfjord , a Field Laboratory for Integrated Submarine Slope Stability Assessments and Characterization of Landslide-Prone Sediments : A Review, in: Offshore Technology Conference.

Vanneste, M., L'Heureux, J.-S., Baeten, N., Brendryen, J., Vardy, M.E., Steiner, A., Forsberg, C.F., Kvalstad, T.J., Laberg, J.S., Chand, S., Longva, O., Rise, L., Haflidason, H., Hjelstuen, B.O., Forwick, M., Morgan, E., Lecomte, I., Kopf, A., Vorren, T.O., Reichel, T., 2012. Shallow Landslides and Their Dynamics in Coastal and Deepwater Environments, Norway, in: Submarine Mass Movements and Their Consequences. Springer Netherlands, Dordrecht, pp. 29–41. doi:10.1007/978-94-007-2162-3_3

Vardy, M.E., 2015. Deriving shallow-water sediment properties using post-stack acoustic impedance inversion. Near Surf. Geophys. 13. doi:10.3997/1873-0604.2014045

Vardy, M.E., L'Heureux, J.-S., Vanneste, M., Longva, O., Steiner, A., Forsberg, C.F., Haflidason, H., Brendryen, J., 2012. Multidisciplinary investigation of a shallow near-shore landslide, Finneidfjord, Norway. Near Surf. Geophys. 10, 267–277. doi:10.3997/1873-2012022

Walsh, J.B., 1966. Seismic Wave Attenuation in Rock Due to Frcition. J. Geophys. Res. 71, 2591–2599.

Walsh, J.B., 1965. The effect of cracks on the compressibility of rock. J. Geophys. Res. 70, 381–389. doi:10.1029/JZ070I002P00381

White, J.E., 1975. Computed Seismic Speeds and Attenuation in Rocks With Partial Gas Saturation. Geophysics 40, 224. doi:10.1190/1.1440520

White, J.E., Mihailova, N., Lyakhovitsky, F., 1975. Low-frequency seismic waves in fluid-saturated layered rocks. J. Acoust. Soc. Am. doi:10.1121/1.1995164

Wood, A.B., 1955. A textbook of sound, Third Revi. ed. Macmillan Co., New York.

Zhao, W., Li, H., Yao, F., 2004. Attenuation Characterization of seismic waves in the wavelet domain and th detection of gas, in: SEG Int'l Exposition and 74th Annual Meeting, Denvor, Colorado. pp. 8–11.

Zhu, T., Harris, J.M., 2015. Improved estimation of P-wave velocity, S-wave velocity, and attenuation factor by iterative structural joint inversion of crosswell seismic data. J. Appl. Geophys. 123, 71–80. doi:10.1016/j.jappgeo.2015.09.005

Zillmer, M., 2006. A method for determining gas-hydrate or free-gas saturation of porous media from seismic measurements. Geophysics 71, N21. doi:10.1190/1.2192910

Zimmerman, R.W., 1991. Compressibility of sandstones. Elsevier.

Chapter 4 **Characterization of Gas-Charged Porous Media: A Joint Inversion of P/S- Wave Attenuation from Both OBS and Sonic Log Data**

4.1 Abstract

Seismic attenuation is an effective indicator of the presence of gas. Compared to velocity, the attenuation responses more strongly to the saturation and permeability besides the porosity. Quantitatively assessing various rock properties from seismic attenuation is a high-dimensional non-linear inverse problem. Considering the inherent non-uniqueness in the inverse problem and the feature of Bayesian inference in data integration and uncertainty analysis, it makes more sense to formulate the inverse problem in a statistical Bayesian framework. We propose a Bayesian workflow to estimate properties of gas-charged porous media by joint Q_p and Q_s inversion from both seismic and sonic log data. The attenuation rock physics models are capable of simultaneously linking Q_p and Q_s of seismic and petrophysical logging datasets to key rock properties of interest. The available information affords to solve at most four parameters only if the attenuation is sensitive to them. In the case study, Q_p and Q_s are measured from both OBS and sonic waveform datasets from the Hydrate Ridge at the Oregon Margin by the centroid frequency shift approach. Then, according to the Bayes theorem, the likelihood function consists of a multivariate Gaussian distribution under the assumption that the error between measured and modeled Q's is Gaussian. We choose gas saturation, porosity, permeability and characteristic size as target parameters after global sensitivity analysis. Subsequently, the marginal posterior distribution of each parameter is calculated by the numerical integration with the adaptive quadrature, which shows the best estimation and its uncertainty. Integrating the sonic log data with seismic data can enormously mitigate the ambiguity of the inversion and estimate more unknowns. The results of the four parameters are in good agreement with previous research in this area.

4.2 Introduction

Geophysical inverse problems target transforming any geophysical data into physical properties. For instance, extracting porosity or density from seismic reflection data is a goal of the typical seismic inversion. Generally, realization of the inference of reservoir properties including characteristics of the rocks (lithology, fluid, porosity) and the physical conditions (pressure, permeability) to which they are subjected from geophysical data is a usual procedure of reservoir characterization. The seismic reflection data, as a main type of geophysical data, cannot only indicate the geometric structure of the subsurface, but also quantifies the properties of the lithologies and fluids.

Conventional seismic inversion obtains time-domain impedance from seismic trace data. Subsequently, the impedance is related to rock properties by rock physics models. They can be grouped into three basic categories: recursive inversion (Lindseth, 1979), generalized linear inversion (Cooke and Schneider, 1983), or sparse spike inversion (Oldenburg et al., 1983). The recursive inversion is based on the well-known formula giving a reflection coefficient in terms of the adjacent acoustic impedance. The impedance is recursively inverted from the very first layer assuming the wavelet is known. The generalized linear inversion utilizes a first order Taylor series expansion of the forward model as the update scheme to optimize the guessed impedance. The last one was initially proposed by Oldenburg et al. (1983), of which deconvolution was imposed on the seismic traces assuming that the reflectivity series are sparse. These three kinds of inversion belong to deterministic method, estimating a single impedance that minimizes the difference between synthetic and real seismic traces. The stochastic method, however, solves the inverse problem to get not only a single set of predicated parameters but also a probability density function on the model space, which represents the uncertainty in the inversion results. Bayesian inversion is a typical stochastic approach, which combines available prior knowledge with the information

contained in the measured data (Tarantola and Valette, 1982; Tarantola, 1987; Duijndam, 1988; Scales and Tenorio, 2001; Ulrych et al., 2001). Gouveia and Scales (1998) defined a Bayesian nonlinear model and estimated the maximum-posterior elastic parameters. Spikes et al. (2007) have demonstrated a rock-physics motivated Bayesian formulation to invert seismic amplitude and well data for reservoir properties. The ability of quantifying the uncertainties caused by measurement or model errors makes stochastic approaches superior to deterministic ones. Understanding the uncertainty facilitates the risk analysis and optimal decision-making.

Even though there are many existent inversion methods, the seismic data is not fully exploited. As shown in Figure 4-1a, the commonly used velocity-based inversion models are only sensitive to porosity and bulk density for the case analyzed in this paper. Many other important properties of the rock such as permeability or saturation are not able to be reliably inverted. For example, at higher levels, CO_2 saturation insensitively responds to P-wave velocity in theoretical studies (Carcione et al., 2006), laboratory experiments (Lei and Xue, 2009) and field studies (Chadwick et al., 2005; Daley et al., 2011), which can also be demonstrated by Figure 4-1b. From Figure 4-1b, we can further find out that at very low levels of gas saturation a small change of saturation would bring a huge change in velocity, which would increase the inversion uncertainty. Additionally, compressional velocity was found to be independent of permeability anisotropy (Gelinsky and Shapiro, 1994; Saleh et al., 2009). While seismic attenuation was significantly affected by gas saturation (Müller et al., 2010; Cabrera et al., 2013) and permeability (Rasolofosaon, 1988; Akbar et al., 1993; Shatilo et al., 1996) in addition to porosity (Klimentos and McCann, 1990; Shatilo et al., 1996) as shown in the sensitivity analysis (Figure 3-4).

Attenuation (also known as Q^{-1}) refers to the exponential decay of the wave amplitude with propagating distance. It is caused by energy-conserved factors (scattering or geometric dispersion), and anelastic dissipation (intrinsic attenuation) where energy is converted into heat. The intrinsic Q is of particular interest to exploration geophysicists. Because it is important in wave-propagation

forward modeling (e.g., Zhu and Harris, 2015); inverse Q filtering; gas-bearing indicating (Klimentos, 1995; Zhao et al., 2004); improvement of full waveform inversion (Barnes et al., 2014). And it is of more interest to us because it can be linked to rock properties and used to parameter estimation. Sometimes, it is difficult to distinguish the intrinsic attenuation from scattering attenuation because both are frequency dependent. In transmission experiments, techniques have been developed to separate the intrinsic attenuation and scattering attenuation (e.g., Wu and Aki, 1988; Sato and Fehler, 2009). In seismic reflection experiments, there have not been reliable techniques that can separate them so far. However, only the inhomogeneity is comparable in scale to the wavelength of elastic waves, the significant scattering will occur (Jackson and Anderson, 1970). When considering homogeneous media, we do not expect a significant level of scattering effect.

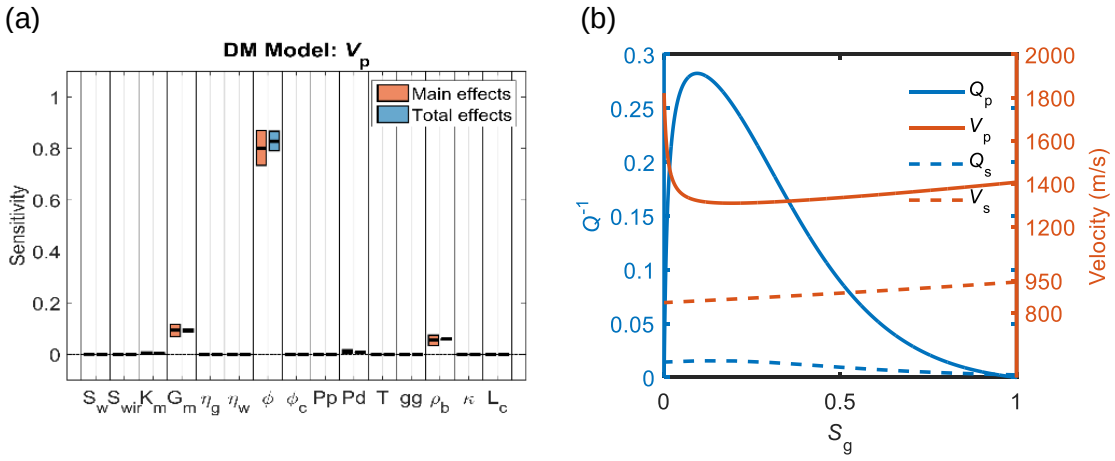

Figure 4-1. a. Sensitivity analysis for Dvorkin-Mavko velocity model, parameter ranges as Table **4-2**; b. comparison of the relationship of Q–S_g and Velocity–S_g. Both are under the condition of Hydrate Ridge, Oregon margin

Many models quantitatively describe the intrinsic attenuation. The earliest and significant one is the wave-induced-fluid flow model for fluid-saturated rocks (Biot, 1956ab; Stoll and Bryan, 1970), of which the fluid flows through the pores or cracks due to fluid-pressure equilibration between the peaks and troughs of a compressional wave or due to grain accelerations in the case of a shear wave, accompanying with internal friction until the pore pressure is equilibrated. Pride et

al. (2004) complemented Biot's model at mesoscopic scales. The second kind is the attenuation resulting from "squirt" flow (Mavko and Nur, 1979; O'Connell and Budiansky, 1974). For partially-saturated liquid-gas systems, local pressure gradients generated by wave compression on rocks lead to fluid movement and viscous dissipation— "squirt" flow. Dvorkin and Nur (1993) offered a BISQ model to treat both Biot and "squirt" flow mechanisms as coupled processes and relate P velocity and attenuation to macroscopic parameters. Additional models include: Walsh's model (1966), based on the friction dissipation when crack surfaces slide to one another; White's spherical model (White, 1975), quantifying the attenuation due to the gas bubble squeezing and moving by introducing a spherical water pockets with a gas bubble at the center; White's layered model (J. E. White et al., 1975), considering a thick section of rock composed of alternating thin layers of porous rock saturated with fluids.

Summarily, seismic attenuation inversion is a powerful and novel tool in reservoir characterization. Singleton and Images (2007) utilized Q_p and Q_s to complement impedance inversion. Raji and Rietbrock (2012) inverted the saturation from theoretic attenuation-saturation curve but had to treat each case individually with the precondition of various rock properties for a given field site. Morgan et al. (2012) inverted gas saturation by P-wave attenuation through the genetic algorithm.

In this paper, we pursue to invert gas saturation, porosity, and permeability from joint Q_p and Q_s with OBS and sonic log data as an improvement for the paper by Lei and Morgan (2015). Other than the joint Q_p and Q_s inversion for OBS data only, two more dimensions of information are added, increasing constraints on the model to suppress the ambiguity, thus shaping the likelihood distribution of the Bayesian algorithm to reduce the modes. Moreover, the additional log data theoretically enables the inversion to estimate two more unknowns. The characteristic size that is a sensitivity parameter to the attenuation model as a byproduct is also inverted. It represents the scale of heterogeneity of the rock and is a poorly determined parameter. Accurately estimating

characteristics size is significant because it determines the resonance frequency thus would be helpful to dispersion analysis. The new inversion is applied on open-source datasets from the Hydrate Ridge, Oregon Margin for the free-gas characterization. The inverted parameters agree with the previous researches (Lee and Collett, 2005) on this area.

4.3 Methodology

In reservoir characterization, the general inverse problem can be represented by the formula

$$\boldsymbol{S} = \boldsymbol{G}\boldsymbol{m} + \boldsymbol{e} \qquad (4-1)$$

where $\boldsymbol{S}$ is the seismic survey, $\boldsymbol{G}$ is the forward model, $\boldsymbol{m}$ is the elastic parameters, e.g., the P- or S- wave impedance, and $\boldsymbol{e}$ is a random error normally distributed with zero mean. When it comes to the attenuation inversion, we substitute $\boldsymbol{Q}$ for $\boldsymbol{S}$, $\boldsymbol{G}$ represents the attenuation rock physics model instead of the velocity-based model, and $\boldsymbol{m}$ is the rock properties such as gas saturation, porosity, etc. The flowchart of the attenuation inversion is shown in Figure 4-2.

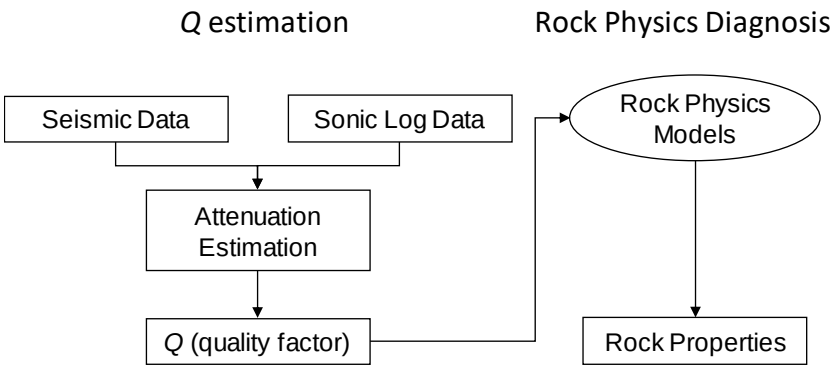

Figure 4-2. The flowchart of the attenuation inversion

With $\boldsymbol{Q} = \left(Q_{p,seismic}, Q_{s,seismic}, Q_{p,log}, Q_{s,log}\right)$ measured from seismic and sonic log data at a location containing gas and sediment properties $\boldsymbol{m} = (m_1, m_2, \dots, m_n)^T$, the seismic attenuation can be linked to the unknown parameters via

$$\boldsymbol{Q} = g(\boldsymbol{m}) + \boldsymbol{e} \qquad (4-2)$$

where $g(\boldsymbol{m})$ denotes the mapping from the rock properties to Q, which can be quantitatively described by the rock physics model. $\boldsymbol{e}$ includes the measurement Q error and model error. The goal is to inversely solve this equation to estimate the parameters $\boldsymbol{m}$ and their uncertainties. Bayesian methods have been previously used to estimation reservoir properties from seismic data

(Bosch et al., 2010). It is capable of detecting multi-solutions and uncertainties, also taking prior information into account.

According to the Bayes theorem, the posterior distribution of $\boldsymbol{m}$ given $\boldsymbol{Q}$ is proportional to the likelihood of $\boldsymbol{Q}$ given $\boldsymbol{m}$ times the prior distribution of $\boldsymbol{m}$. Assuming the error e is Gaussian distributed, the likelihood is

$$L(\boldsymbol{Q}|\boldsymbol{m}) = \exp\left\{\frac{1}{2}[\boldsymbol{Q} - g(\boldsymbol{m})]^T \boldsymbol{\Sigma}_e^{-1}[\boldsymbol{Q} - g(\boldsymbol{m})]\right\} \quad (4-3)$$

where $\boldsymbol{\Sigma}_e$ is the covariance matrix of error between the observed $\boldsymbol{Q}$ and modeled $\widehat{\boldsymbol{Q}} = g(\boldsymbol{m})$. Assuming all parameters are independent of each other, the prior should be

$$\pi(\boldsymbol{m}) = \prod_{i=1}^{n} \pi(m_i). \quad (4-4)$$

There are many ways to represent the prior for one parameter $\pi(m_i)$. The commonly used approaches are as follows:

a) Uniform prior: when there is not enough prior information, we can consider a uniform distributed parameter bounded within $[a, b]$ as prior information

$$\pi(m) = \begin{cases} \dfrac{1}{b-a}, & a \le m \le b, \\ 0, & m < a, m > b; \end{cases} \quad (4-5)$$

b) logit normal prior: we could also consider a logit normal distribution for each parameter

$$\pi(m) \propto \exp\left(-\frac{1}{2}\frac{(\text{logit}(P) - \mu)^2}{\sigma_\pi^2}\right) \quad (4-6)$$

where μ and σ_π^2 are the mean and variance of prior, respectively, and

$$\text{logit}(P) = \log\frac{P}{1-P}, P = \frac{b-m}{b-a}; \quad (4-7)$$

or c) triangular prior with an arbitrary point c within $[a, b]$:

$$\pi(m) = \begin{cases} \dfrac{2(m-a)}{(b-a)(c-a)}, & a \le m \le c, \\ \dfrac{2(b-m)}{(b-a)(b-c)}, & c < m \le b, \\ 0, & m < a, m > b. \end{cases} \quad (4-8)$$

Lastly, the resulting posterior is then given by

$$P(\boldsymbol{m}|\boldsymbol{Q}) \propto \exp\left\{\frac{1}{2}[\boldsymbol{Q} - g(\boldsymbol{m})]^T \Sigma_e^{-1}[\boldsymbol{Q} - g(\boldsymbol{m})]\right\} \prod_{i=1}^{n} \pi(m_i)\,. \qquad (4-9)$$

4.3.1 Intrinsic Attenuation Models

To solve the inverse problem relies on the rock physics models. The rock physics model is a mathematic expression of the intrinsic attenuation mechanisms. Intrinsic loss is the fraction of wave energy that is converted to heat in each wave period, often indicated by inverse quality factor Q^{-1}. The physical mechanisms of wave-induced energy loss include: the crack surfaces sliding to one another (Walsh, 1995); wave-induced fluid flow from the crack to the pore or the edge to the center due to pressure difference between the peek and the trough of the compressional wave (Biot, 1956a; Biot, 1956b; Stoll and Bryan, 1970); the squirting flow due to the pore space deformation when the wave compresses (Mavko and Nur, 1979; O'Connell and Budiansky, 1974; Dvorkin and Nur, 1993); the internal gas bubble squeezing and motion (White, 1975; White et al., 1975). Other attenuation mechanism is negligible since they make much small contribution to the overall energy loss. For linear viscoelastic media, elastic moduli are no longer constants, but complex variables in terms of frequency, which gives rise to wave dispersion and attenuation. There are many mathematical models for the complex moduli to describe the wave behavior in viscoelastic and anisotropic media (Carcione, 2014). Among them, the standard linear solid model (Zener and Siegel, 1949) is preferred because it is convenient to be used in finite-difference algorithms (Emmerich, 1987); has finite phase velocity and attenuation coefficient at very high and very low frequencies; is able to include more elements. In SLS, shear stress and shear strain would be related by using

$$\eta\dot{\sigma}_{ij} + (E_1 + E_2)\sigma_{ij} = E_2\left(\eta\dot{\varepsilon}_{ij}\right) \qquad (4-10)$$

where E_1 and E_2 are additional elastic moduli and η is a material constant resembling viscosity. If we assume sinusoid motion

$$\varepsilon = \varepsilon_0 e^{i\omega t} \tag{4-11}$$

$$\sigma = \sigma_0\, e^{i\omega t} \tag{4-12}$$

and substitute into equation 4 - 10

$$\sigma_0 = M(\omega)\varepsilon_0. \tag{4-13}$$

The complex frequency-dependent modulus is

$$M(\omega) = \frac{E_2(E_1 + i\omega\eta)}{(E_1 + E_2 + i\omega\eta)}. \tag{4-14}$$

In the limits of the low frequency and the high frequency, the limit moduli are

$$M_0 = \frac{E_2 E_1}{E_1 + E_2}, \omega \to 0 \tag{4-15}$$

$$M_\infty = E_2, \omega \to \infty. \tag{4-16}$$

Please note that at very low and very high frequencies the moduli are real and independent of frequency, and thus in these limits the material behaves elastically. Rewrite the complex modulus in terms of those limits:

$$M(\omega) = \frac{M_\infty \left[M_0 + i\frac{\omega}{\omega_c}(M_\infty M_0)^{1/2}\right]}{\left(M_\infty + i\frac{\omega}{\omega_c}(M_\infty M_0)^{1/2}\right)} \tag{4-17}$$

where ω_c is the material resonance frequency

$$\omega_c = \frac{\sqrt{\left(E_1(E_1 + E_2)\right)}}{\eta}. \tag{4-18}$$

The quality factor is the ratio of the imaginary and real parts of the complex moduli:

$$\frac{1}{Q} = \frac{M_I(\omega)}{M_R(\omega)} \tag{4-19}$$

$$\frac{1}{Q} = \frac{M_\infty - M_0}{\sqrt{M_\infty M_0}} \frac{\omega/\omega_c}{1 + (\omega/\omega_c)^2}; \tag{4-20}$$

thus, it is related to the very high and very low frequencies.

The attenuation models commit to give mathematic descriptions of the complex moduli, thus offering the quantity of the *Q*. According to the investigation scale of the induced fluid flow, they can be classified as "macroscopic", "mesoscopic", and "microscopic". The macroscopic flow occurs at the wavelength scale. Biot loss is a typical macroscopic attenuation; however, it drastically underestimates the energy loss in the seismic band (Pride et al., 2004). Mavko and Nur, (1979), Budiansky and O'connell, (1976) and O'Connell and Budiansky (1978) proposed a microscopic "squirt-flow" model considering the fluid flow from microcracks to pores. Even though it seems capable of quantifying the attenuation in laboratory at the ultrasonic frequency, it is still not consistent with the measured attenuation in the seismic band. The preferred investigation scale for intrinsic attenuation is mesoscopic. For partially saturated media, the patch fluid saturation contributes much to mesoscopic-scale heterogeneity, which affects the rock properties (e.g., Knight et al., 1998). The patches are occupied by two immiscible fluids and the pressure difference occurs because of the different compressibility of two fluids. When the wave squeezes the rock and pores, the pressure is higher in a patch with more compressible fluid than that in a patch with less compressible fluid; thus, the attenuation results from the two-fluid-phase equilibrium. In the next part, we are going to discuss three patchy saturation models.

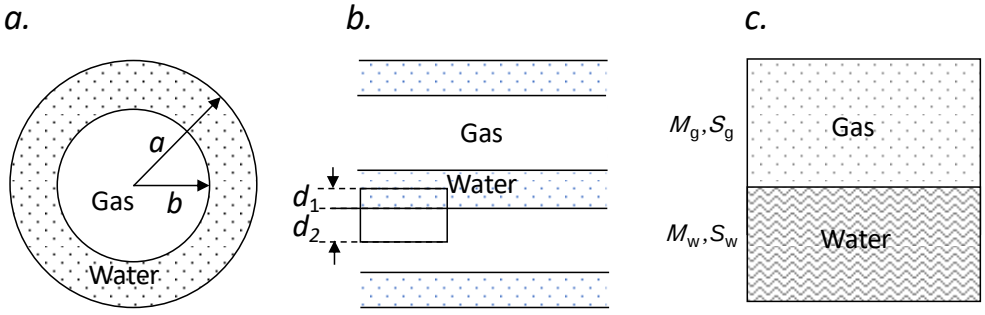

Figure 4-3. Schematic diagram of three patchy saturation models. a: White's Spherical model; b: White's Layered model; c: Dvorkin-Mavko model.

Dvorkin-Mavko model

Dvorkin and Mavko (2006) proposed a theory for calculating the P- and S-wave inverse quality factors (Q_s^{-1} or Q_s^{-1}) at partial gas saturation. It copes with the complex moduli at infinite frequency limits by way of assuming two separate rectangular patches containing water and gas phases (Figure 4-3c). The reaction of the rock with patchy saturation to loading from the elastic wave depends on the frequency. If the frequency is low and then the loading is slow, there would be equilibrium between the fully liquid-saturated patch and partially-saturated domains next to it. Then, the very low frequency compressional moduli

$$M_0 = K_{sat} + 4/3\mu_{dry} \qquad (4-21)$$

is estimated from Gassmann's equation (Gassmann, 1951) directly.

$$K_{sat} = K_m \frac{\phi K_{dry} - (1+\phi)K_f K_{dry}/K_m + K_f}{(1-\phi)K_f + \phi K_m - K_f K_{dry}/K_m} \qquad (4-22)$$

where the fluid moduli K_f is the harmonic average of water moduli K_w and gas moduli K_g:

$$K_f = S_w K_w^{-1} + (1-S_w)K_g^{-1}. \qquad (4-23)$$

For the very high frequency moduli M_∞, we assume that all liquid in partially saturated rock is concentrated in fully saturated patches and the rest of the rock is filled with gas. The patch is "unrelaxed" because of the disequilibrium caused by oscillatory variations of pore pressure between the fully-water-saturated patch and the fully-gas-saturated patch. Then the effective moduli at the high frequency M_∞ is equal to the harmonic average of the compressional moduli of the rock with only water M_w and rock with only gas M_g:

$$M_\infty^{-1} = S_w M_w^{-1} + (1-S_w)M_g^{-1} \qquad (4-24)$$

or

$$M_\infty^{-1} = \frac{S_w - S_{wir}}{1-S_{wir}} M_w^{-1} + \frac{1-S_w}{1-S_{wir}} M_g^{-1} \qquad (4-25)$$

if taking irreducible water saturation into consideration. M_w and M_g can be calculated through Gassmann's equation for each patch. The characteristic frequency that accords with equation 4 - 18, at which the inverse quality factor is maximum, then is

$$f_c = \frac{\kappa}{{L_c}^2 \eta(\beta_p + \beta_f)} \qquad (4-26)$$

where β_p is the compressibility of the pore space (Walsh, 1965; Zimmerman, 1991)

$$\beta_p = \frac{1}{\phi}\left(\frac{1}{K_{dry}} - \frac{1}{K_m}\right) \qquad (4-27)$$

and β_f is the compressibility of the effective fluid by isostress average (Wood, 1955) of the moduli of the liquid and gaseous phases $\beta_f = S_w\beta_w + (1 - S_w)\beta_g$; η and κ are the viscosity and permeability of the effective fluid; L_c is the characteristic length, which represents the scale of the medium heterogeneity and is related to the pore and grain details.

Additionally, shear-wave attenuation depends on P-wave attenuation of fully water-saturated sediments. Assuming the reduction in both the compressional modulus and shear modulus between high-frequency and low-frequency limits are caused by the aligned defects or flaws, the shear-modulus-versus-frequency dispersion is derived from compressional-modulus-versus-frequency dispersion by Hudson's theory for crack media (Hudson, 1980, 1981). If the material isotropy caused by the random oriented defects is responsible for both the compressional and shear reduction, then the ratio is

$$\frac{Q_P^{-1}}{Q_S^{-1}} = \frac{1}{M/G}\left[\frac{4}{3} + \frac{5}{4}\frac{(M/G - 2/3)(M/G - 4/3)^2}{M/G - 8/9}\right] \qquad (4-28)$$

where M or G is assumed to be the geometrical average of the low and high frequency limits of the compressional or shear moduli $M = \sqrt{M_0 M_\infty}$, $G = \sqrt{G_0 G_\infty}$.

White's layered model

White et al. (1975) considered a periodic layered system composed of porous media 1 and 2. Each medium is a fluid-saturated isotropic solid (Figure 4-3b). In the perspective of the elementary volume as shown, there is no fluid flow across the center of the layer. The fluid flows through the boundary of two media. Under this assumption, the saturation of phase i (water or gas) is equal to

$$S_i = \frac{d_i}{d_1 + d_2}, i = 1 \; or \; 2; \tag{4-29}$$

the complex compressional modulus is as follows

$$M^* = \left[\frac{1}{M_0} + \frac{2(r_2 - r_1)^2}{i\omega(d_1 + d_2)(I_1 + I_2)}\right]^{-1} \tag{4-30}$$

where

$$M_0 = \left(\frac{S_1}{M_{sat,1}} + \frac{S_2}{M_{sat,2}}\right)^{-1}. \tag{4-31}$$

The $M_{sat,i}$ is the compressional modulus of the fluid-i-saturated rock, estimated by Gassmann's equation (Gassmann, 1951). For each medium,

$$r_i = \left(1 - \frac{K_{dry}}{K_m}\right)\frac{M_i}{M_{sat,i}} \tag{4-32}$$

which is the ratio of the fast P-wave fluid tension to the total normal stress,

$$I_i = \frac{\eta_i}{\kappa_i k_i} coth\left(\frac{k_i d_i}{2}\right) \tag{4-33}$$

where

$$M_i = \frac{K_m}{1 - \phi - K_{dry}/K_m + \phi K_m/K_{f,i}}, \tag{4-34}$$

K_m is solid-grain modulus, $K_{f,i}$ is the fluid i bulk modulus, K_{dry} is the dry-rock matrix modulus, η_i and κ_i are viscosity and permeability of each fluid phase, respectively. Additionally,

$$k_i = \sqrt{\frac{i\omega\eta_i}{\kappa_i K_{E,i}}} \tag{4-35}$$

where

$$K_{E,i} = \frac{M_{dry} M_i}{M_{sat,i}}. \quad (4-36)$$

The approximate resonance frequency separating the relaxed and unrelaxed states is

$$f_c = \frac{8\kappa_2 K_{E,2}}{\pi \eta_2 d_2^2} \quad (4-37)$$

where subscript 2 refers to water for a layered medium alternately saturated with water and gas.

White's spherical model

White (1975) modeled the seismic effects of patchy saturation by considering porous rocks saturated with brine but containing spherical gas-filled regions (Figure 4-3a). The idealized geometry of a unit cell consists of the gas region with radius a and the surrounding water shell with radius b. The gas saturation S_g is equal to a^3/b^3. Adjacent unit cells do not interact with each other. The pressure difference resulting from the different fractional volume change of two patches leads to fluid flow across the boundary, followed by attenuation and dispersion of seismic waves. Assuming the gas region is denoted by subscript 1, the outer water region is denoted by subscript 2, and the dry frame bulk moduli of both region 1 and 2 are the same. The Q_P is the ratio of real and imaginary parts of the complex compressional modulus M^*.

$$M^* = K^* + \frac{4}{3}\mu_{dry} \quad (4-38)$$

where

$$K^* = \frac{K_\infty}{1 - K_\infty W} = K_r^* + iK_i^* \quad (4-39)$$

$$W = \frac{3a^2(R_1 - R_2)(-I_1 + I_2)}{b^3 i\omega(Z_1 + Z_2)} \quad (4-40)$$

$$R_1 = \frac{K_1 - K_{dry}}{1 - K_{dry}/K_m} \frac{3K_2 + 4\mu_2}{K_2(3K_1 + 4\mu_2) + 4\mu_2(K_1 - K_2)S_g} \quad (4-41)$$

$$R_2 = \frac{K_2 - K_{dry}}{1 - K_{dry}/K_m} \frac{3K_1 + 4\mu_1}{K_2(3K_1 + 4\mu_2) + 4\mu_2(K_1 - K_2)S_g} \quad (4-42)$$

$$Z_1 = \frac{\eta_1 a}{\kappa_1}\left[\frac{1 - e^{-2\alpha_1 a}}{(\alpha_1 a - 1) + (\alpha_1 a + 1)e^{(-2\alpha_1 a)}}\right] \quad (4-43)$$

$$Z_2 = -\frac{\eta_2 a}{\kappa_2} \frac{(\alpha_2 b + 1) + (\alpha_2 b - 1)e^{2\alpha_2(b-a)}}{(\alpha_2 b + 1)(\alpha_2 a - 1) - (\alpha_2 b - 1)(\alpha_2 a + 1)e^{-2\alpha_1 a}} \quad (4-44)$$

$$\alpha_i = \left(\frac{i\omega\eta_i}{\kappa_i K_{Ei}}\right)^{1/2} \quad (4-45)$$

$$K_{E,i} = \left[1 - \frac{K_{f,i}(1 - K_i/K_m)\left(1 - K_{dry}/K_m\right)}{\phi K_i\left(1 - K_{f,i}/K_m\right)}\right] K_{A,i} \quad (4-46)$$

$$K_{A,i} = \left(\frac{\phi}{K_{f,i}} + \frac{1-\phi}{K_m} - \frac{K_{dry}}{K_m^2}\right)^{-1} \quad (4-47)$$

$$I_i = \frac{\left(1 - K_{dry}/K_m\right)K_{A,i}}{K_i} \quad (4-48)$$

$$K_\infty = \frac{K_2(3K_1 + 4\mu_2) + 4\mu_2(K_1 - K_2)S_g}{3K_1 + 4\mu_2 - 3(K_1 - K_2)S_g} \quad (4-49)$$

where K_i and μ_i are saturated bulk and shear moduli of region i which could be estimated from Gassmann's equation; K_m and $K_{f,i}$ are solid and fluid bulk moduli; η_i is the fluid viscosity. The characteristic frequency is

$$f_c \approx \frac{\kappa_2 K_{E,2}}{\pi\eta_2 b^2} \quad (4-50)$$

4.3.2 Numerical Integration

The goal of the inversion is to obtain the best estimation and its uncertainty of the rock parameters $\boldsymbol{m}$. From the posterior, we know the joint conditional distribution of each target parameter $P(\boldsymbol{m}|\boldsymbol{Q})$. The marginal distribution can tell us the solution and uncertainty of each parameter m_i, which is calculated by the following integration

$$P(m_i|Q) = \int_{m_1} \cdots \int_{m_j} \cdots \int_{m_n} P(\boldsymbol{m}|\boldsymbol{Q}) dm_1 dm_2 \cdots dm_j \cdots dm_n, \quad j = 1 \cdots n \; except \; i. \quad (4-51)$$

Because the rock physics model that links the model and the data is nonlinear, the posterior and its marginal distribution must be computed numerically. In order to compute the integration in equation 4 - 51, we use uniform discretization of the model space $m_i \in [a_i, b_i]$, evaluate the probability at each point of the discretized space, and compute the numerical integration of the corresponding parameter.

4.4 Application: The Hydrate ridge, Oregon margin

We test the methodology using OBS and sonic log datasets in Hydrate Ridge, Oregon margin. The Hydrate Ridge is a 25-km-long and 15-km-wide accretionary ridge in the Cascadia convergent margin (Mackay et al., 1995). Gas hydrate and accompanying free gas has been found to be well developed beneath Hydrate Ridge (Tréhu et al., 1999). A seismic experiment was conducted during 2002 and multichannel streamer and OBS data were acquired to map the concentration of gas hydrate and free gas. Throughout the region, gas hydrate, which occupies, on average, 2%–8% of the pore space, is present in a depth range that extends from ~30 mbsf to the BSR (Bottom Simulated Reflection, which indicates the bottom of gas hydrate and usually the top of free gas zone). The 3-D seismic data enable reconstruction of the geologic history. The OBS allows to record shear and compressional waves, from which we can estimate Q_p and Q_s. We use OBS survey TN112 (station 01, shot line NS-01, as shown in Figure 4-4). It crosses Ocean Drilling Program (ODP) well 1244E and 1245E (leg 204). The ODP Leg 204 is the first expedition dedicated to understanding gas hydrate in an accretionary complex. According to the ODP analysis by Tréhu et al. (2006)and Lee and Collett (2005), the average gas hydrate saturations are about 10.2% and 10.4% for Site 1244 (76−127 mbsf (meters below seafloor)) and Site 1245 (73−129 mbsf), respectively. The free gas is often accompanying with and contained beneath the gas hydrate reservoir because gas hydrate is easy to resolve, and the reservoir is under low permeability so that it forms a good cap for free gas. The free gas saturation between 127 and 226 mbsf at Site 1244 estimated from Modified Boit-Gassmann theory by Lee (2002) is about 1.6% or 1.7%. And at Site 1245, the free gas saturation is about ~6.4% or 6.8% (129−294 mbsf).

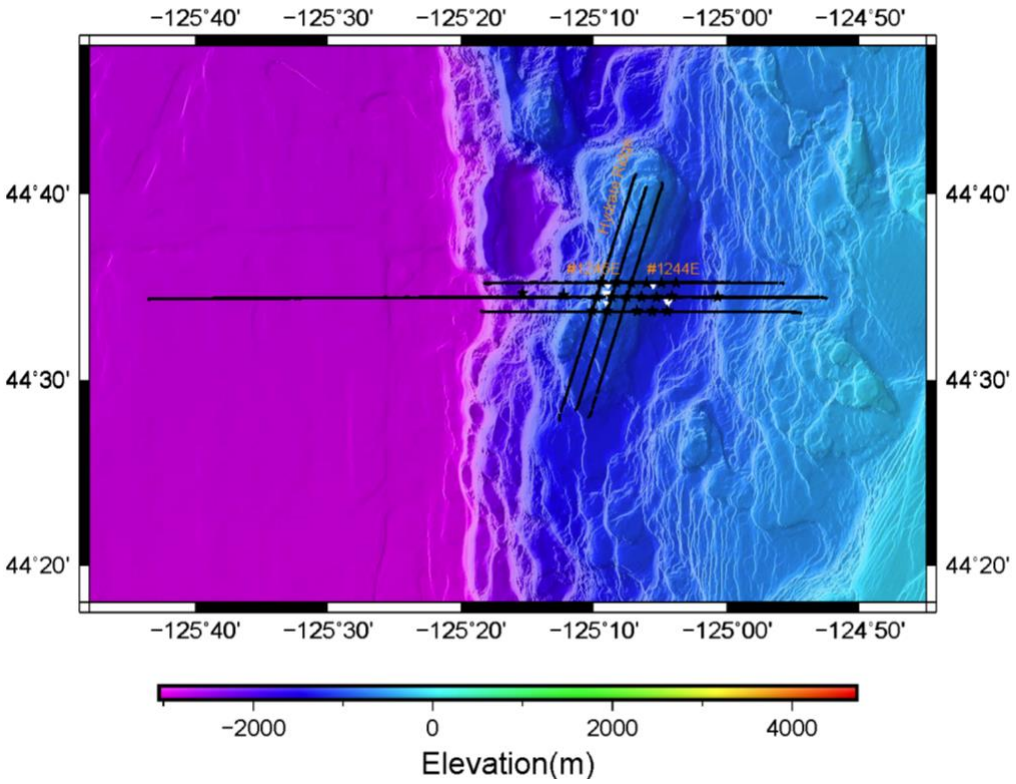

Figure 4-4. Geological setting of the Hydrate Ridge, offshore Oregon Margin. The shots (black dots, interval is about 40 m) and OBSs (black stars) were deployed. The ODP wells crossing the survey lines are shown as white triangles.

The first step of the inversion is to accurately estimate Q from both OBS and sonic log data. For OBS data, we take it as the common reflection data, the compressional wave in hydrophone component and shear wave in the rotated transverse component. As shown in Figure **4-5**, the first thing for Q measurement is to extract the traces corresponding to the well locations from the OBS data. The gas hydrate and free gas zones are then identified on both components (target depth can be converted into traveltime by V_p or V_s). After picking up the target signals from the free gas zone, we implement the estimation method–CFS paired with Technique I, suggested by Lei and Morgan (2016). In order to suppress the uncertainty of the estimation, we also randomly simulate 100 truncation windows around the one suggested in Chapter 2, because the window size or location matters a lot in Q estimation. By doing so, we would have 100 estimated Q's and could take the mean of them. For the sonic log data, the Dipole Shear Sonic Imager (DSI) recorded the Upper

Dipole (UDP), Lower Dipole (LDP) and Monopole P&S mode (MPS) logs for both vertical exploration well 1244 and 1245. We have eight records that represent signals obtained from eight receivers in the logging device for each depth, of which the P- and S- waves are identified by their traveltimes considering their source-receiver distances and V_p and V_s (Figure 4-6). Assuming the wavelet energy loss from first receiver (receiver 1) to the last one (receiver 8) is due to intrinsic attenuation, we could carry out the Q estimation on truncated signals that represent P- or S- waves from receiver 1 and receiver 8. The reason that I choose signals from receiver 1 and receiver 8 not other combinations is that they have the longest travelling distance, meaning that the signals has been mostly attenuated, which will reduce the estimation errors according to the finding in Chapter 2. In the waveform profile (Figure 4-6), the first peak of P- or S- waveform can be located by the quotient of distance over velocity, and the window size is set as about 1.8 times of the wave frequency which is in accordance with the conclusion made in Chapter 2. The measured Q from both OBS and sonic log data for free gas zone is shown in Table 4-1 and Figure **4-7**. Please note the P-wave attenuation is estimated from data acquired on the MPS mode, while the S-wave attenuation is from data acquired on the UDP mode.

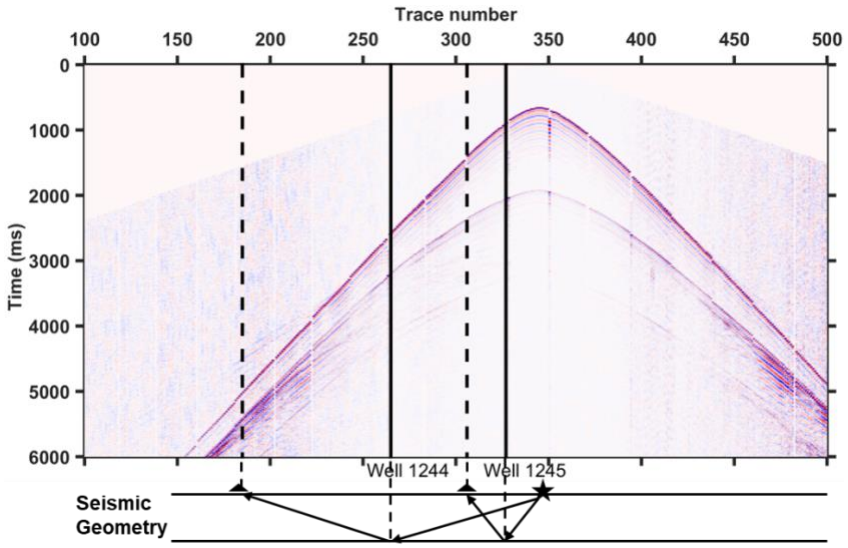

Figure 4-5. OBS data, H component, line NS1, station 01, Cruise TN112, Hydrate Ridge. The traces whose CMP's correspond to the well locations are as the dashed lines.

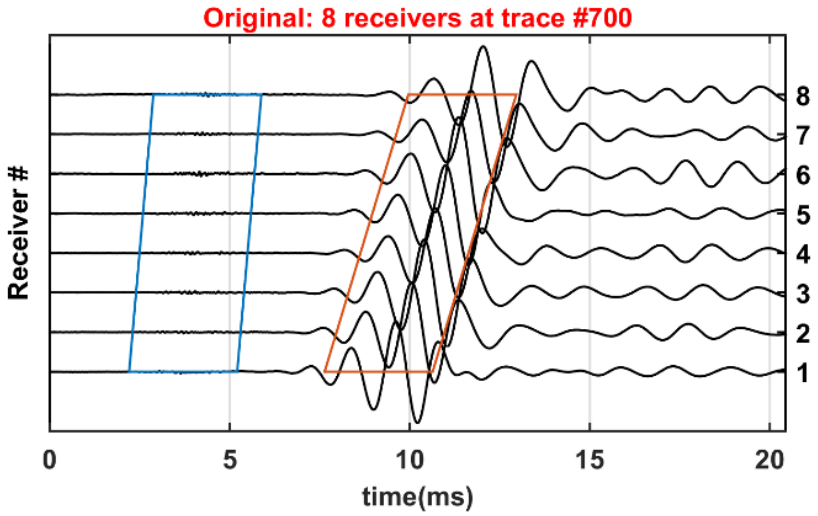

Figure 4-6. One trace of the sonic log, representing one depth. The receiver 1 is closest to source and receiver 8 is furthest to the source. The blue diamond area picks the compressional wave which is faster than the shear wave that is selected by red diamond area. The time window for diamonds is 2.5 ms.

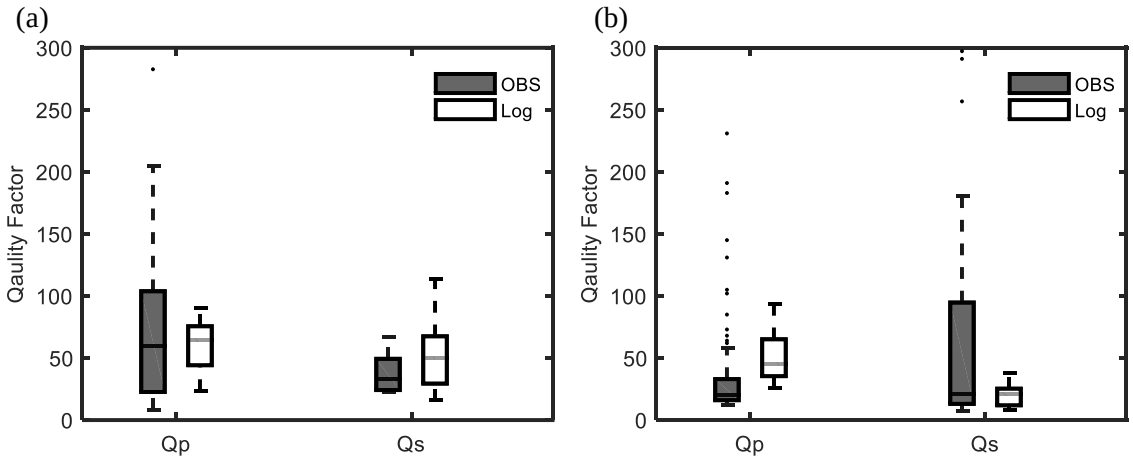

Figure 4-7. *Q* estimation from Oregon Margin OBS data and from ODP sonic log data, a. well 1244; b. well 1245.

Table 4-1. Mean of *Q* estimated from seismic and sonic log data, Hydrate Ridge, Oregon Margin

		Q_p	Q_s
Log	Well 1244	62	51
	Well 1245	43	20
OBS	Well 1244	58	33
	Well 1245	32	19

To ensure the validity of the forward modeling and the reliability of the inverse modeling, it is necessary to conduct a sensitivity analysis. By using the attenuation model of Dvorkin and Mavko (2006), the summary of the input parameters $\boldsymbol{m}$ is below and their appropriate boundaries and prior values are in Table **4-2**.

$$\boldsymbol{m} = \{S_w, S_{wir}, K_m, G_m, \eta_g, \eta_w, \phi, \phi_c, P_p, P_d, T, gg, f, \kappa, L_c\}. \quad (4-52)$$

where S_w, S_{wir} represents the water and irreducible water saturation in the rock; K_m, G_m are the bulk and shear moduli of the solid phase of the rock; the viscosity is denoted as η; pore pressure and differential pressure (difference between the pore pressure and the overburden pressure) are denoted as P_p and P_d; the temperature, gas gravity, frequency, permeability and characteristic size are T, gg, f, κ, L_c, respectively. Because the frequency of a given data is fixed and easily calculated, we did not take the frequency into consideration when conducting the sensitivity analysis but set it as frequencies estimated from P- or S- wave seismic data. The other parameter ranges that we use are as Table **4-2**. After global sensitivity analysis (Saltelli et al., 2010) of each parameter to the rock physics model (Figure 3-4), the P-wave quality factor is the most responsive to saturation, porosity, bulk and shear moduli, rock permeability, and characteristic size; slightly reacts to the water viscosity and differential pressure. Summarily, six parameters $\{S_w, \phi, K_m, G_m, \kappa, L_c\}$ have the potential to be reliably estimated by this joint Q_p and Q_s attenuation model considering their sensitivities. On the other hand, the data available (Q_p and Q_s from OBS and sonic log data) mathematically determines that it is possible to invert any four of the six parameters.

Then, we conduct the joint inversion process by using the attenuation from OBS and sonic log data to estimate gas saturation, porosity, permeability, and characteristic size. The final marginal distributions of parameters are shown in Figure **4-9**, and the best estimation with its uncertainty is as Table **4-3**. Please note that here the marginal distribution is integrated from likelihood not posterior, meaning that we do not consider the prior information for this case, which

will validate the model itself without including the prior calibration. In the discussion section, we illustrate the advantages and disadvantages of this method.

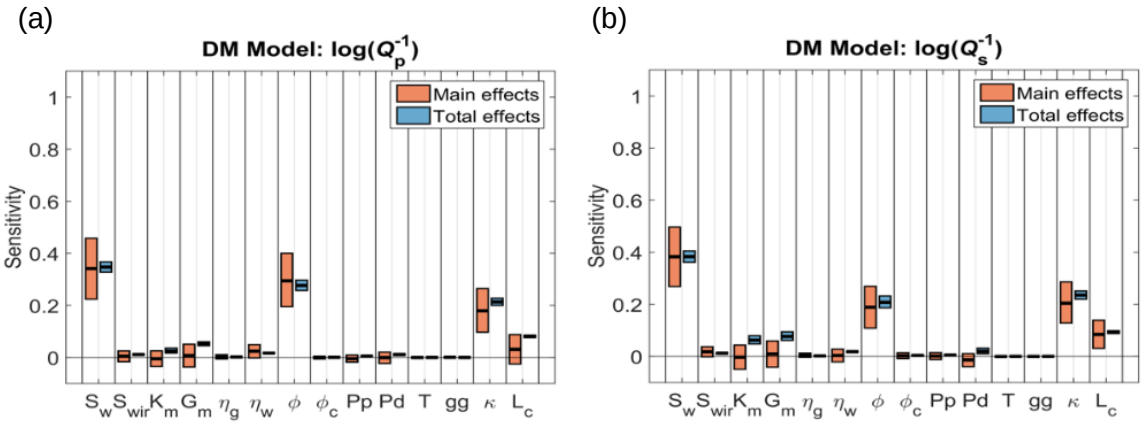

Figure 4-8. Sensitivity indices for Dvorkin-Mavko model: a. log(Q_p^{-1}); b. log(Q_s^{-1}). Main and total effects are two different kinds of indices representing the extent of parameter sensitivities to the DM model.

Table 4-2. Initial values and bounds for each parameter

		Well 1244 (127~226m[a])	Well 1245 (129~294m[a])
	Bounds	Values	Values
Gas Saturation S_g	0~80%	0.4%[b], 0.3%[c], 1.6%[d], 1.2%[d]	1.6%[b], 1.7%[c], 6.4%[d], 6.8%[d]
Irreducible Water Saturation S_{wir}	0.0~0.2	0.0	0.0
Porosity ϕ	0.26~0.95[j]	0.50[a], 0.61[j]	0.50[a, i], 0.62[j]
Critical Porosity ϕ_c	0.36~0.4[k]	0.38	0.38
Solid Grain Bulk Moduli K_m(GPa)	20~70[a]	25[f]	25[f]
Solid Grain Shear Moduli G_m(GPa)	5~50[a]	9[f]	9[f]
Gas Viscosity η_g (mPa·S)	0.1~0.2	0.15[g]	0.15[g]
Water Viscosity η_w (mPa·S)	1~5	3[g]	3[g]
Gas Specific Gravity gg	0.56	0.56[f]	0.56[f]
Pore Pressure P_p (MPa)	8~12[i]	10.0[i]	10.0[i]
Differential Pressure P_d (MPa)	0.1~2	0.5[i]	0.5[i]
Frequency f (Hz)	0~10^6	40(OBS); 10000(monopole); 1400(dipole)[h]	40(OBS); 10000(monopole); 1400(dipole)[h]
Temperature T (°C)	5~17[j]	7[j]	7[j]
Intrinsic Permeability κ (mD)	0.001~1000[l]	63.8[m], 405[m]	63.8[m], 405[m]
Characteristic Size L_c (mm)	0.2~2.0[n, o](DM)	1.5(DM)	1.4(DM)

[a]Lee and Collett (2005); [b]Based on V_p (Lee and Collett, 2005); [c]Moduli methods (Lee and Collett, 2005); [d]NMR log (Lee and Collett, 2005); [e]Tréhu et al. (2006); [f]Mavko et al. (2009); [g]Carcione and Picotti (2006); [h]Estimated from OBS and log data; [i]Tréhu et al. (2004); [j]Shipboard Scientific Party (2003); [k]Nur et al. (1998); [l]Spinelli et al. (2004); [m]Screaton et al. (1995); [n]Dvorkin and Nur (1993); [o]Mavko et al. (2009)

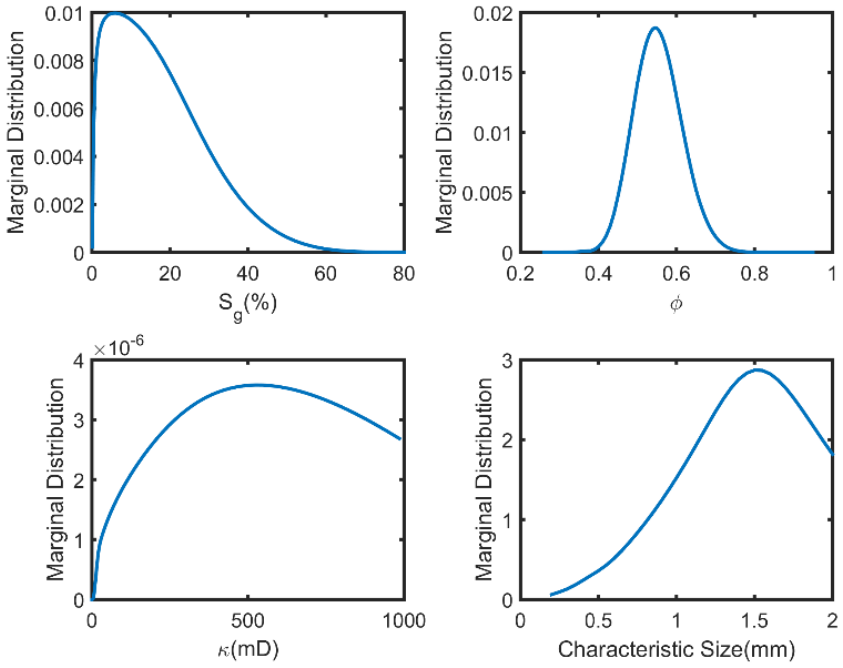

Figure 4-9. Numerical integration results: marginal distribution of the likelihood of the well 1244

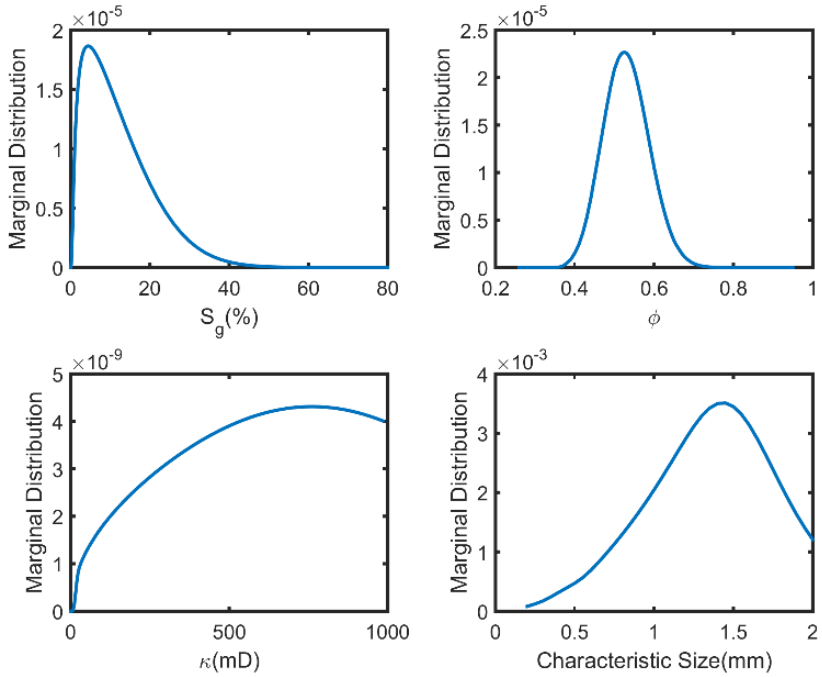

Figure 4-10. Numerical integration results: marginal distribution of the likelihood of the well 1245

Table 4-3. Best estimation (±2$\boldsymbol{\sigma}$) of the numerical integration

	S_g (%)	ϕ	κ (mD)	L_c (mm)
Well 1244	5.9±1.83	0.55±0.012	525±63.0	1.50±0.084
Well 1245	4.5±1.11	0.53±0.012	765±63.1	1.45±0.082

4.5 Discussion

The joint inversion workflow successfully integrates the sonic log data, which enhances the parameter estimation dimensions and reliability. It could be implemented on unconventional gas reservoirs such as shale gas, tight gas, or coalbed methane, besides the conventional one, only if we choose proper rock physics models against the target reservoirs. The essence of the attenuation inversion is the measurable anelastic energy dissipation when seismic wave passing through the rock bearing gas. The gas in the pores increases the chance of the fluid movement and thus increases the fluid friction either between multiphases or between fluid and grain surfaces. So, it is believable that the proposed method is applicable to shale gas (organic rich rock physics model by Li et al., 2015), or tight gas (a rock physics model for low-porosity-low-permeability condition by Ruiz and Cheng, 2010; Wang, 2017).

The mentioned three rock physics models have commons and differences based on its origination or derivation. They all modeled the wave-induced fluid flow created by mesoscopic-scale heterogeneity. Mesoscopic length scales are those larger than grain sizes but smaller than wavelengths. Heterogeneity across these scales may be caused by lithological variations or patches with different immiscible fluids. Due to its smaller scale than wavelength, we do not expect a significant level of scattering attenuation if the heterogeneity is mesoscopic. Additionally, they are all patchy saturation models assuming that porous frame properties are everywhere uniform, and the gas and water are separately distributed into the adjacent patch pairs. Biot's theory then works

on the local model for mesoscopic flow between two patches. The differences only lie in patch geometries. Dvorkin-Mavko model is derived from the standard linear solid by assuming the rock consisting of adjacent patches, some of which might be fully water-saturated while other patches may contain gas. The whole volume will have patchy distribution. White's spherical model, however, assumes the gas and fluid are reserved in the inner sphere and outer shell of a concentric porous sphere, respectively. Moreover, the White's layered model consists of alternating thin layers of porous rock separately saturated with gas and fluid. Under the same condition, the sensitivity analyses implemented on those three models are shown in Figure 3-4, Figure 4-11, Figure 4-12. They have the same sensitive parameters except that the sensitive indices are different. Especially, the White's layered model seems much less sensitive to gas saturation.

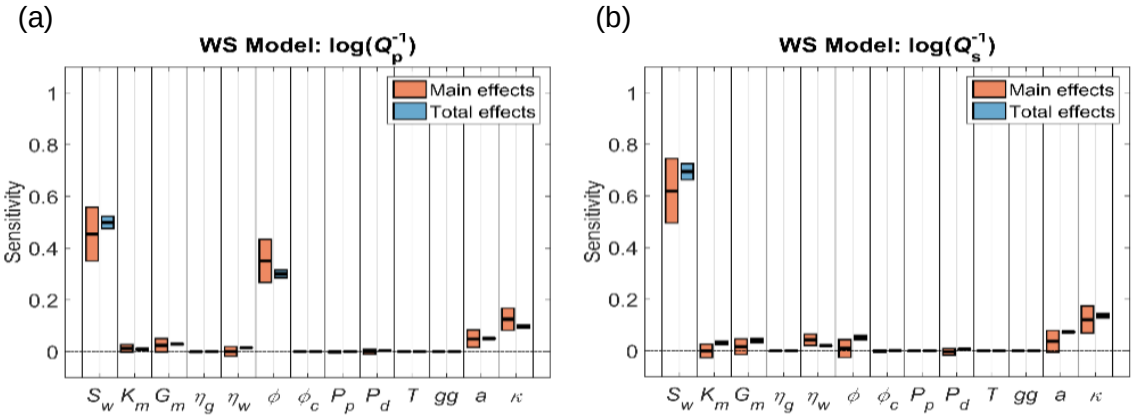

Figure 4-11. Sensitivity indices for White's spherical model: a. log(Q_p^{-1}); b. log(Q_s^{-1}). Main and total effects are two different kinds of indices representing the extent of parameter sensitivities to the WS model.

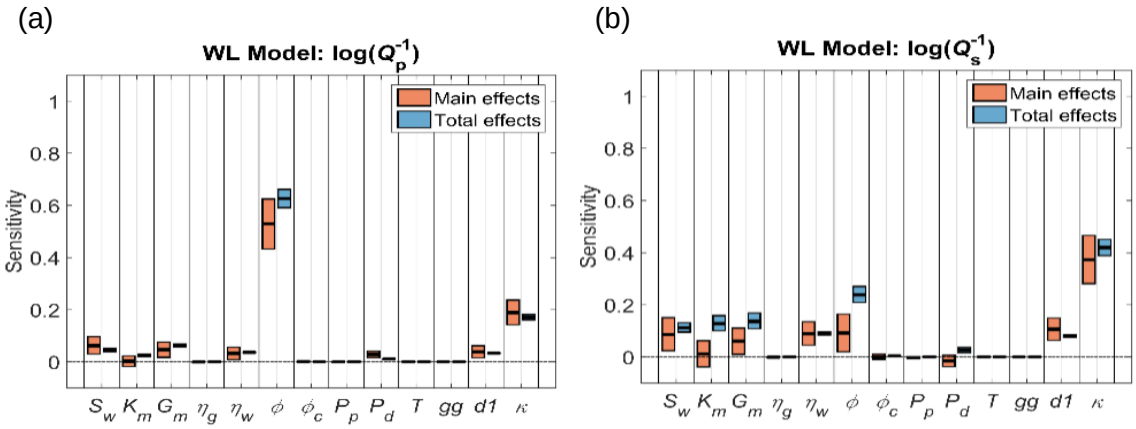

Figure 4-12. Sensitivity indices for White's layered model: a. log(Q_p^{-1}); b. log(Q_s^{-1}). Main and total effects are two different kinds of indices representing the extent of parameter sensitivities to the WL model

Mathematically, the number of independent information determines how many unknowns we can solve. Our method solves four parameters from Q_p and Q_s of seismic and sonic log data (Figure 3-11). If we could have more independent information added into the inversion workflow, it is expected to invert more parameters. Even though the sonic log data reduces the ambiguity of the four-variable inverse problem, the multi-solutions caused by the nonlinearity of the model are still existent. Figure 3-7 showed the numerical test for Dvorkin-Mavko model. Assuming the parameters of the rock physics model are given as Table **4-2**, now we change S_w and ϕ within their bounds in a step to exhaustively calculate the modeled Q_p. It is obvious that the relationship between attenuation and parameters S_w and ϕ is a nonlinear surface. Conversely, given a Q_p value, the number of corresponding solutions of saturation and porosity are infinite. The projection of the solutions in the plane of saturation and porosity will be roughly an ellipse (Figure 3-8). By adding Q_s, we have one more ellipse and the final solutions should be the intersection points *A* and *B* of those two circles, which enormously mitigates the ambiguity from an infinite number of solutions into two solutions. If we increase the number of the unknown parameters to three, let's say S_w, ϕ, and κ, and the known information were Q_p, Q_s from seismic data and Q_p from sonic log data, then the $S_w - \phi - \kappa - Q$ relation would be about a three-dimensional solid. Similarly, given a Q value,

the corresponding solutions to the unknowns projected in the $S_w - \phi - \kappa$ space would be a surface if existing. Then, the final solution would be the intersection of the three surfaces obtained by knowing Q_p, Q_s from seismic data and Q_p from sonic log data, which might be multiple points in the $S_w - \phi - \kappa$ space if existing. Furthermore, if we extend this problem to $S_w - \phi - \kappa - L_c - Q$ space, the final solution would be the intersection of four 4-dimensional solids by knowing Q_p, Q_s from seismic data and Q_p, Q_s from sonic log data, which also consists of multiple points but in the $S_w - \phi - \kappa - L_c$ space. Summarily, we can see that the additional known Q's do not completely but enormously mitigate the ambiguity of the inverse problem. The residual ambiguity would be suppressed by constraints or the prior information. For example, Figure 3-9 and Figure 3-10a show us the joint probability-density distribution and marginal distribution of a two-parameter (S_w, ϕ) inverse problem. Even though for gas saturation the margin of the likelihood is multi-mode, the posterior is single mode after imposing a given prior.

Additionally, we implement the same workflow for White's layered model and White's spherical model to compare their efficacy. In the White's layered model, the characteristic size describes the scale of the spherical patch, while it describes the scale of the layered patch in the White's spherical model. Since they are poorly determined, we set relatively large ranges for them according to literatures. For White's layered model, $L_c \in$ [10 ~ 20] mm, the initial value takes middle value 15 mm (Carcione and Picotti, 2006; Morgan et al., 2012); while for White's spherical model, $L_c \in$ [0.4 ~ 1.5] mm, the initial value takes middle value 0.8 mm (Mavko et al., 2009). The marginal distributions of gas saturation, porosity, permeability, and characteristic size are as Figure 4-13, Figure **4-14**, Figure 4-15, Figure 4-16. In Figure 4-13, we can see a multi-mode for gas saturation. It could be suppressed by prior information, since the two modes are far away from each other and the free gas saturation is highly likely less than 10% of the Hydrate Ridge area (Lee and Collett, 2005). However, both of them perform worse than the Dvorkin-Mavko model. It is difficult to have a mode for the characteristic size, even though we enlarge its range to an unreasonable

zone. The possible explanation is that the assumed patchy geometry of Dvorkin-Mavko model much more agrees with the in-situ state of Hydrate Ridge area; or the sensitivity of some parameters such as saturation to the White's spherical model is much lower than that to Dvorkin-Mavko model. Since the characteristic size has significant impacts on the attenuation rock physics model but is hard to determine, further investigation is needed to improve the inversion workflow.

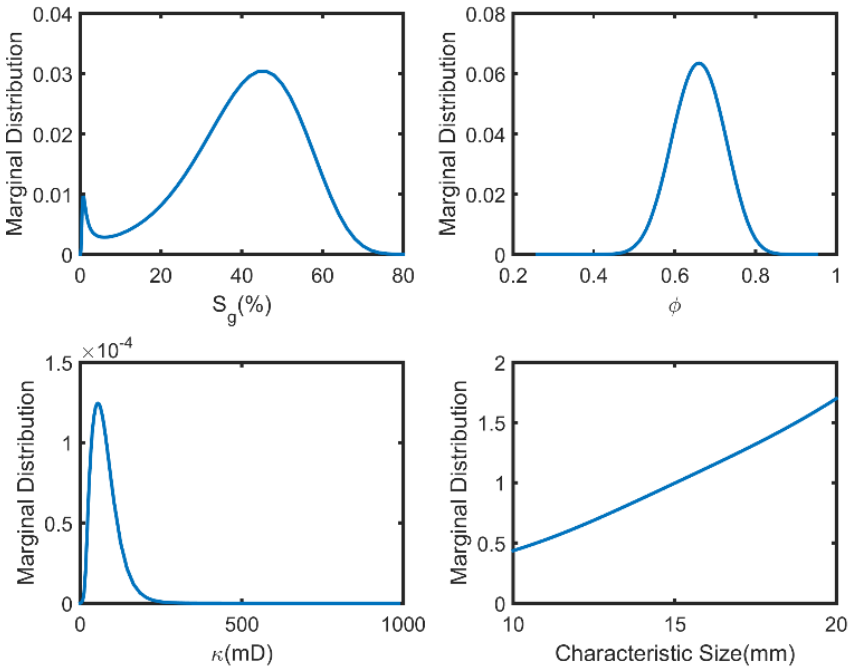

Figure 4-13. Numerical integration results: marginal distribution of the likelihood of the well 1244, White's layered model

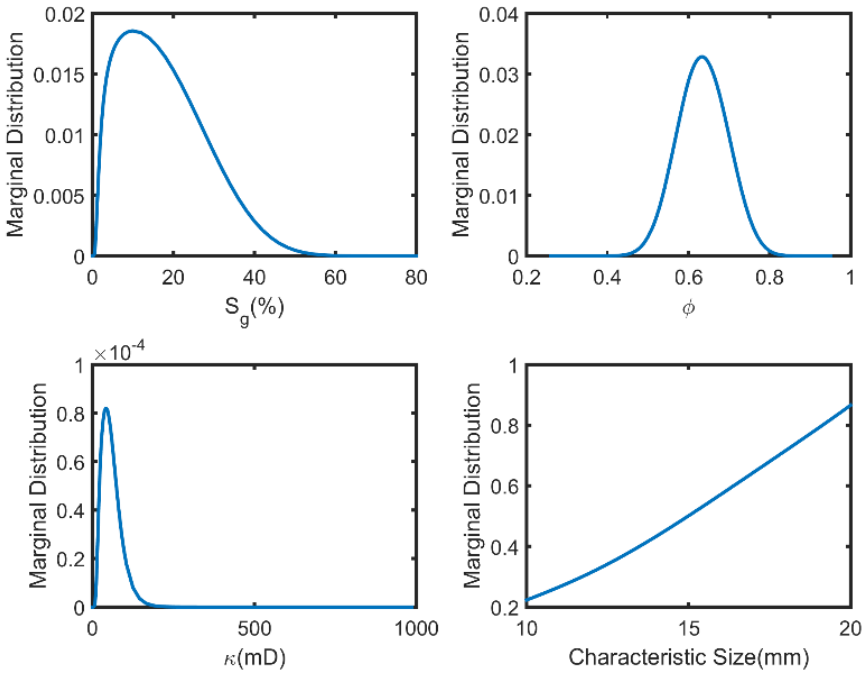

Figure 4-14. Numerical integration results: marginal distribution of the likelihood of the well 1245, White's layered model

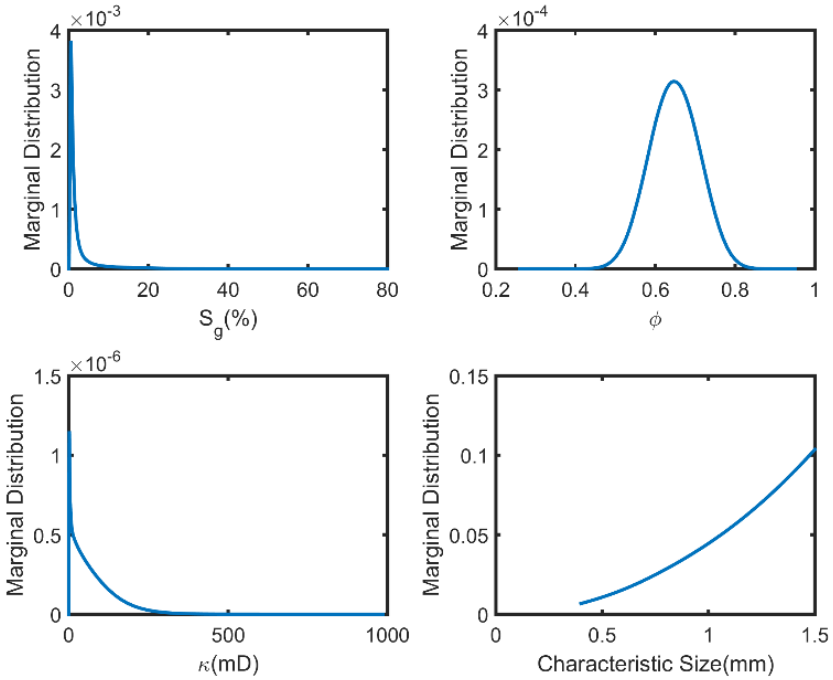

Figure 4-15. Numerical integration results: marginal distribution of the likelihood of the well 1244, White's spherical model

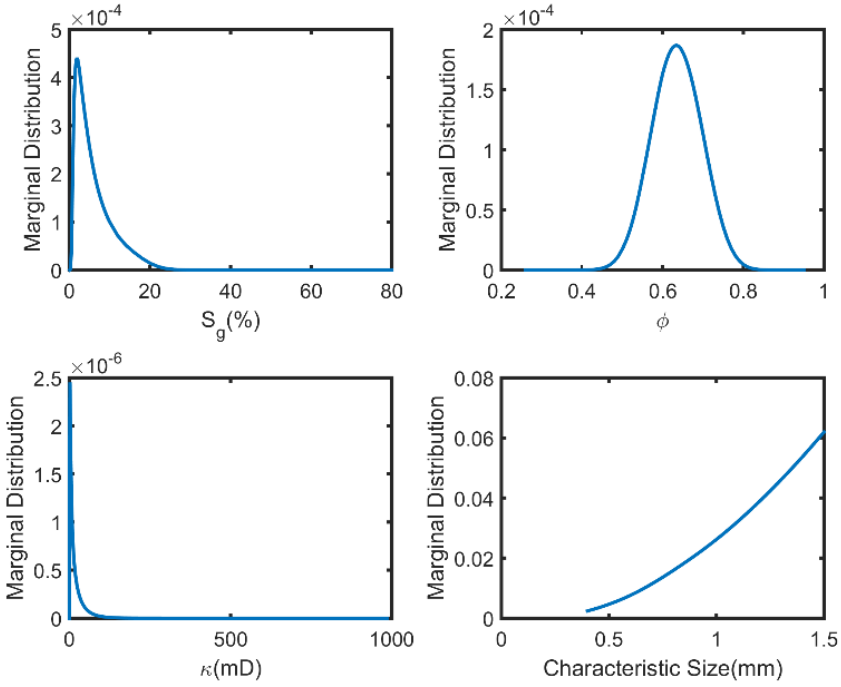

Figure 4-16. Numerical integration results: marginal distribution of the likelihood of the well 1245, White's spherical model

Lastly, we compare the computing efficiency of the stochastic scheme, Markov-Chain Monte Carlo, with the integration approach when obtaining the solution distribution. MCMC scheme samples the parameter space stochastically according to the posterior. The results are shown in Table **4-4**, which almost agree with the results from the integration approach (Table **4-3**). However, it saves a lot of computation and is more efficient especially with respect to a four-parameter inverse problem, taking about 87 seconds for a chain with 50,000 steps in total (Figure **4-17**, Figure 4-18), while the integration approach takes about 3 hours parallelly running on the cluster. The drawback of applying MCMC might be the difficulty in choosing proper searching parameters which matters a lot in MCMC sampling. The integration approach, in turn, is easily to conduct but runs much more slowly. Its computational cost increases at the exponential rate with the number of the parameters.

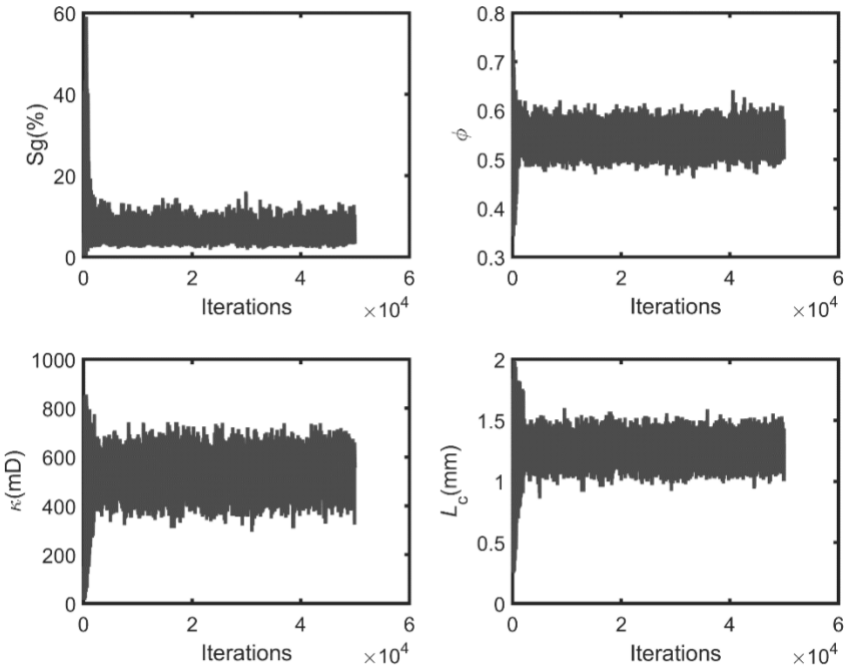

Figure 4-17. MCMC results: marginal distribution of the likelihood of the well 1244, Dvorkin-Mavko model

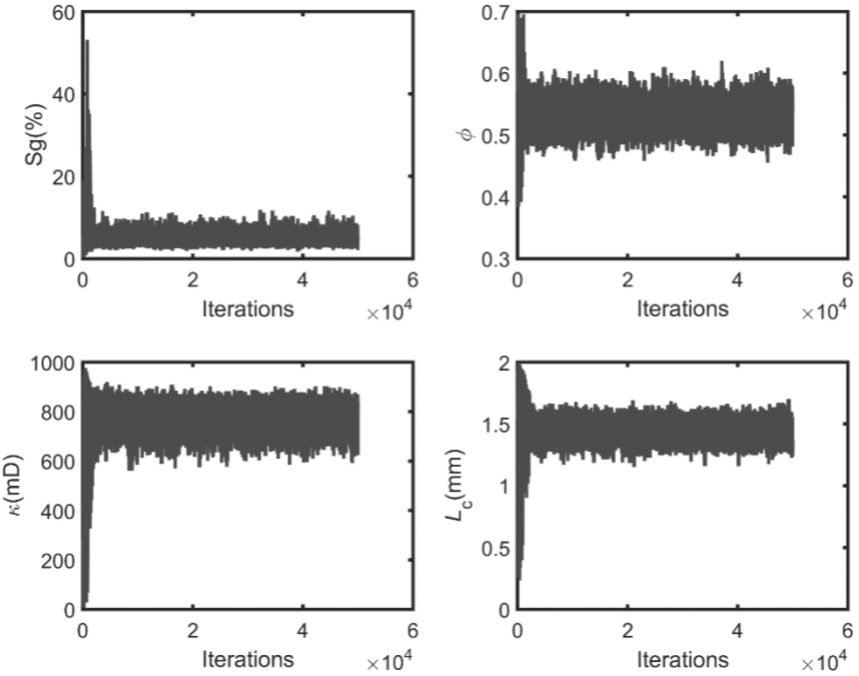

Figure 4-18. MCMC results: marginal distribution of the likelihood of the well 1245, Dvorkin-Mavko model

Table 4-4. Best estimation (±2$\boldsymbol{\sigma}$) of the MCMC scheme

	S_g (%)	ϕ	κ (mD)	L_c (mm)
Well 1244	5.1±3.35	0.54±0.042	529±122.9	1.26±0.180
Well 1245	4.5±2.54	0.53±0.042	776±96.5	1.45±0.145

4.6 Conclusion

As showed in Table 4-1, the seismic data and sonic waveform data from ODP well 1244 and 1245, where gas was discovered (Lee and Collett, 2005), are used to estimate the Q_p and Q_s at different frequencies for gas-bearing zones. The frequency dependency of quality factor makes the integration of seismic data with sonic logs feasible in the attenuation inversion workflow. In Figure 3-11, the seismic Q and sonic log Q fall in different frequency bands. The four independent dimensions of information are mathematically able to solve four unknowns.

The gas saturations S_g = 5.9% ± 1.83% at Site 1244 and S_g = 4.5% ± 1.11% at Site 1245 are compatible to the statement (Tréhu et al., 2006) that the free gas is at low levels, even though they are not the same as saturations shown in Table **4-2** by Lee and Collett (2005). The possible explanations are: firstly, the free gas might migrate through the gas hydrate stable zone along faults or fractures at these sites; secondly, part of the free gas might form the hydrate beneath the BSR when the condition changes in the gas aggregation area; moreover, the estimation offered by Lee and Collett (2005) remains in question because the generality of some of the empirical relationships used to convert geophysical observations to in-situ gas or gas hydrate quantity relies on the calibration of various proxies; however, to accurately obtain the calibration constant without other independent estimations of free gas is not easy. Except that, other parameters estimated are in good agreement with the analysis by Lee and Collett (2005). Additionally, the numerical integration of the posterior effectively provides us the marginal distribution of the corresponding parameter. Compared with the stochastic scheme such as Markov-Chain Monte Carlo, this method gives us a smoother distribution without even random errors. Moreover, the application on the Hydrate Ridge demonstrates the generalizability of this method to shallow environments that have low levels of pressure and gas saturation. Also, this research focuses on gas reservoir characterization, but the

methodology is promisingly extendible to oil or other types of reservoirs if we could have a significant *Q* anomaly.

Acknowledgements. We thank Institute for Geophysics at the University of Texas at Austin (UTIG) for providing the OBS dataset and thank Lamont-Doherty Earth Observatory at Columbia University for collecting and distributing the IODP dataset.

4.7 Reference

Akbar, N., Dvorkin, J., Nur, A., 1993. Relating P - wave attenuation to permeability. GEOPHYSICS 58, 20 – 29. doi:10.1190/1.1443348

Akbar, N., Dvorkin, J., Nur, A., 1993. Relating P - wave attenuation to permeability. GEOPHYSICS 58, 20 – 29. doi:10.1190/1.1443348

Barnes, C., Cergy-pontoise, U. De, Charara, M., Williamson, P., 2014. P & S wave attenuation effects on full-waveform inversion for marine seismic data 949–953.

Biot, M.A., 1956a. Theory of Propagation of Elastic Waves in a Fluid-Saturated Porous Solid. I. Lower Frequency Range. J. Acoust. Soc. Am. doi:10.1121/1.1908241

Biot, M.A., 1956b. Theory of Propagation of Elastic Waves in a Fluid - Saturated Porous Solid. II. Higher Frequency Range. J. Acoust. Soc. Am. 28, 168 – 178. doi:10.1121/1.1908241

Bosch, M., Mukerji, T., Gonzalez, E.F., 2010. Seismic inversion for reservoir properties combining statistical rock physics and geostatistics: A review. GEOPHYSICS 75, 75A165-75A176. doi:10.1190/1.3478209

Budiansky, B., O'connell, R.J., 1976. Elastic moduli of a cracked solid. Int. J. Solids Struct. 12, 81–97. doi:10.1016/0020-7683(76)90044-5

Cabrera, F., Vivas, F.A., Camacho, G.D., Gonzalez, H., 2013. Mesoscopic P-wave attenuation model to estimation of free gas saturation, in: 13th International Congress of the Brazilian Geophysical Society & EXPOGEF, Rio de Janeiro, Brazil, 26–29 August 2013. Society of Exploration Geophysicists and Brazilian Geophysical Society, pp. 1078–1082. doi:10.1190/sbgf2013-223

Carcione, J.M., 2014. Wave fields in real media : wave propagation in anisotropic, anelastic, porous and electromagnetic media, Third edition. ed.

Carcione, J.M., Picotti, S., 2006. P-wave seismic attenuation by slow-wave diffusion: Effects of inhomogeneous rock properties. Geophysics 71, 01–08.

Carcione, J.M., Picotti, S., Gei, D., Rossi, G., 2006. Physics and Seismic Modeling for Monitoring CO2 Storage. Pure Appl. Geophys. 163, 175–207. doi:10.1007/s00024-005-0002-1

Chadwick, R.A., Arts, R., Eiken, O., 2005. 4D seismic quantification of a growing CO2 plume at Sleipner, North Sea, in: Petroleum Geology: North-West Europe and Global Perspectives – Proceedings of the 6th Petroleum Geology Conference. Geological Society of London, pp. 1385–1399. doi:10.1144/0061385

Cooke, D.A., Schneider, W.A., 1983. Generalized linear inversion of reflection seismic data. GEOPHYSICS 48, 665–676. doi:10.1190/1.1441497

Daley, T.M., Ajo-Franklin, J.B., Doughty, C., 2011. Constraining the reservoir model of an injected CO2 plume with crosswell CASSM at the Frio-II brine pilot. Int. J. Greenh. Gas Control 5, 1022–1030. doi:10.1016/J.IJGGC.2011.03.002

Duijndam, A.J.W., 1988. BAYESIAN ESTIMATION IN SEISMIC INVERSION. PART I: PRINCIPLES1. Geophys. Prospect. 36, 878–898. doi:10.1111/j.1365-2478.1988.tb02198.x

Dvorkin, J., Mavko, G., 2006. Modeling attenuation in reservoir and nonreservoir rock. Lead. Edge

25, 194. doi:10.1190/1.2172312

Dvorkin, J., Nur, A., 1993. Dynamic poroelasticity: A unified model with the squirt and the Biot mechanisms. Geophysics 58, 524. doi:10.1190/1.1443435

Emmerich, H., 1987. Incorporation of attenuation into time-domain computations of seismic wave fields. Geophysics 52, 1252. doi:10.1190/1.1442386

Gassmann, F., 1951. Über die Elastizität poröser Medien, Vier. Der Natur.

Gelinsky, S., Shapiro, S.A., 1994. Poroelastic velocity and attenuation in media with anisotropic permeability, in: SEG Technical Program Expanded Abstracts 1994. Society of Exploration Geophysicists, pp. 818–821. doi:10.1190/1.1932010

Gouveia, W.P., Scales, J.A., 1998. Bayesian seismic waveform inversion: Parameter estimation and uncertainty analysis. J. Geophys. Res. Solid Earth 103, 2759–2779. doi:10.1029/97JB02933

Hudson, J. a. A., 1981. Wave speeds and attenuation of elastic waves in material containing cracks. Geophys. J. R. Astron. Soc. 64, 133–150. doi:10.1111/j.1365-246X.1981.tb02662.x

Hudson, J.A., 1980. Overall properties of a cracked solid. Math. Proc. Cambridge Philos. Soc. 88, 371–384. doi:10.1017/S0305004100057674

Jackson, D.D., Anderson, D.L., 1970. Physical mechanisms of seismic-wave attenuation. Rev. Geophys. 8, 1. doi:10.1029/RG008i001p00001

Klimentos, T., 1995. Attenuation of P- and S- waves as a method of distinguish gas and condensate from oil and water. Geophysics 60, 447–458.

Klimentos, T., McCann, C., 1990. Relationships among compressional wave attenuation, porosity, clay content, and permeability in sandstones. GEOPHYSICS 55, 998–1014. doi:10.1190/1.1442928

Knight, R., Dvorkin, J., Nur, A., 1998. Acoustic signatures of partial saturation. GEOPHYSICS 63, 132–138. doi:10.1190/1.1444305

Lee, M.W., 2002. Biot – Gassmann theory for velocities of gas hydrate - bearing sediments. GEOPHYSICS 67, 1711 – 1719. doi:10.1190/1.1527072

Lee, M.W., Collett, T.S., 2005. Gas Hydrate and Free Gas Saturations Estimated from Velocity Logs on Hydrate Ridge, Offshore Oregon, USA, in: Tréhu, A.M., Bohrmann, G., Torres, M.E., and Colwell, F.S. (Ed.), Proceedinfs of the Ocean Drilling Program, Scientific Results, 204. pp. 1–25. doi:102973/odp.proc.sr.204.103.2006

Lei, X., Morgan, E.C., 2016. A comparison of methods for estimating Q, in: SEG Technical Program Expanded Abstracts 2016. Society of Exploration Geophysicists, pp. 3021–3025. doi:10.1190/segam2016-13971809.1

Lei, X., Morgan, E.C., 2015. Characterization of Gas-charged Sediments from Joint Inversion of Qp and Qs, in: SEG Technical Program Expanded Abstracts 2015. Society of Exploration Geophysicists, pp. 2765–2770. doi:10.1190/segam2015-5904497.1

Lei, X., Xue, Z., 2009. Ultrasonic velocity and attenuation during CO2 injection into water-saturated porous sandstone: Measurements using difference seismic tomography. Phys. Earth Planet. Inter. 176, 224–234. doi:10.1016/j.pepi.2009.06.001

Li, Y., Guo, Z.-Q., Liu, C., Li, X.-Y., Wang, G., 2015. A rock physics model for the

characterization of organic-rich shale from elastic properties. Pet. Sci. 12, 264–272. doi:10.1007/s12182-015-0029-6

Lindseth, R.O., 1979. Synthetic sonic logs—a process for stratigraphic interpretation. GEOPHYSICS 44, 3–26. doi:10.1190/1.1440922

Mackay, M.E., Moore, G.F., Klaeschen, D., von Huene, R., 1995. The case against porosity change: Seismic velocity decrease at the toe of the Oregon accretionary prism. Geology 23, 827–830.

Mavko, G., Nur, A., 1979. Wave attenuation in partially saturated rocks. Geophysics 44, 161–178.

Mavko, G., Tapan, M., Dvorkin, J., 2009. The Rock Physics Handbook: Tools for seismic analysisin porous media, Second Edi. ed. Cambridge University Press, New York.

Morgan, E.C., Vanneste, M., Lecomte, I., Baise, L.G., Longva, O., McAdoo, B., 2012. Estimation of free gas saturation from seismic reflection surveys by the genetic algorithm inversion of a P-wave attenuation model. Geophysics 77, R175. doi:10.1190/geo2011-0291.1

Müller, T.M., Gurevich, B., Lebedev, M., 2010. Seismic wave attenuation and dispersion resulting from wave-induced flow in porous rocks — A review. Geophysics 75, 75A147. doi:10.1190/1.3463417

Nur, A., Mavko, G., Dvorkin, J., Galmudi, D., 1998. Critical porosity: A key to relating physical properties to porosity in rocks. Lead. Edge 17, 357. doi:10.1190/1.1437977

O'Connell, R.. J., Budiansky, B., 1978. Measures of Dissipation in Viscoelastic Media. Geophys. Res. Lett. 5, 5–8.

O'Connell, R.J., Budiansky, B., 1974. Seismic velocities in dry and saturated cracked solids. J. Geophys. Res. 79, 5412–5426. doi:10.1029/JB079i035p05412

Oldenburg, D.W., Scheuer, T., Levy, S., 1983. Recovery of the acoustic impedance from reflection seismograms. GEOPHYSICS 48, 1318–1337. doi:10.1190/1.1441413

Pride, S.R., Berryman, J.G., Harris, J.M., 2004. Seismic attenuation due to wave-induced flow. J. Geophys. Res. 109, 1–19. doi:10.1029/2003JB002639

Raji, W.O., Rietbrock, a., 2012. The use of seismic attenuation for monitoring saturation in hydrocarbon reservoirs. SEG Tech. Progr. Expand. Abstr. 2012 1–6. doi:10.1190/segam2012-0309.1

Rasolofosaon, P.N.J., 1988. Influence of permeability on the attenuation of bulk and interface acoustic waves (experiment versus theory), in: SEG Technical Program Expanded Abstracts 1988. Society of Exploration Geophysicists, pp. 925–927. doi:10.1190/1.1892406

Ruiz, F., Cheng, A., 2010. A rock physics model for tight gas sand. Lead. Edge 29, 1484–1489. doi:10.1190/1.3525364

Saleh, M., Vega, S., Prasad, M., Sharma, R., 2009. A study of permeability and velocity anisotropy in carbonates, in: SEG Technical Program Expanded Abstracts 2009. Society of Exploration Geophysicists, pp. 4238–4242. doi:10.1190/1.3255766

Saltelli, A., Annoni, P., Azzini, I., Campolongo, F., Ratto, M., Tarantola, S., 2010. Variance based sensitivity analysis of model output. Design and estimator for the total sensitivity index. Comput. Phys. Commun. 181, 259–270. doi:10.1016/j.cpc.2009.09.018

Sato, H., Fehler, M.C., 2009. Seismic Wave Propagation and Scattering in the Heterogeneous Earth. Springer Berlin Heidelberg, Berlin, Heidelberg. doi:10.1007/978-3-540-89623-4

Scales, J.A., Tenorio, L., 2001. Prior information and uncertainty in inverse problems. GEOPHYSICS 66, 389–397. doi:10.1190/1.1444930

Screaton, E.J., Carson, B., Lennon, G.P., 1995. Hydrogeologic properties of a thrust fault within the Oregon Accretionary Prism. J. Geophys. Res. 100, 20025. doi:10.1029/95JB02152

Shatilo, A., Sondergeld, C., Rai, C., 1996. Relationship between ultrasonic P - wave attenuation and porosity, permeability and clay content in Glenn Pool sandstone, in: SEG Technical Program Expanded Abstracts 1996. Society of Exploration Geophysicists, pp. 1679–1682. doi:10.1190/1.1826451

Shipboard Scientific Party, 2003. Leg 204 Summary, in: Tréhu, A.M., Bohrmann, G., Rack, F.R., Torres, M.E., et al. (Ed.), Proceedings of the Ocean Drilling Program, Initial Reports Volume 204.

Singleton, S., Images, R.S., 2007. The use of Seismic Attenuation and Simultaneous Impedance Inversion in Geophysical Reservoir Characterization SEG / San Antonio 2007 Annual Meeting SEG / San Antonio 2007 Annual Meeting 1422–1426.

Spikes, K., Mukerji, T., Dvorkin, J., Mavko, G., 2007. Probabilistic seismic inversion based on rock-physics models. GEOPHYSICS 72, R87–R97. doi:10.1190/1.2760162

Spinelli, G.A., Giambalvo, E.R., Fisher, A.T., 2004. Sediment permeability, distribution, and influence on fluxes in oceanic basement, in: Elderfield, E.E.D. and H. (Ed.), Hydrogeology of the Oceanic Lithosphere, Eds. Cambridge University Press.

Stoll, R.D., Bryan, G.M., 1970. Wave Attenuation in Saturated Sediments. J. Acoust. Soc. Am. 47.

Tarantola, A., 1987. Inverse problem theory : methods for data fitting and model parameter estimation. Elsevier.

Tarantola, A., Valette, B., 1982. Generalized Nonlinear Inverse Problems Solved Using the Least Squares Criterion. Rev. Geophys. Sp. Phys. 20, 219–232.

Tréhu, A.M., Flemings, P.B., Bangs, N.L., Chevallier, J., Gràcia, E., Johnson, J.E., Liu, C.S., Liu, X., Riedel, M., Torres, M.E., 2004. Feeding methane vents and gas hydrate deposits at south Hydrate Ridge. Geophys. Res. Lett. 31, 1–4. doi:10.1029/2004GL021286

Tréhu, A.M., Torres, M.E., Bohrmann, G., Colwell, F.S., 2006. Leg 204 synthesis: gas hydrate distribution and dynamics in the central Cascadia accretionary complex, in: Tréhu, A.M., Bohrmann, G., Torres, M.E., and Colwell, F.S. (Ed.), Proceedinfs of the Ocean Drilling Program, Scientific Results, 204. pp. 1–40. doi:10.2973/odp.proc.sr.204.101.2006

Tréhu, A.M., Torres, M.E., Moore, G.F., Suess, E., Bohrmann, G., 1999. Temporal and spatial evolution of a gas hydrate–bearing accretionary ridge on the Oregon continental margin. Geology 27, 939–942.

Ulrych, T.J., Sacchi, M.D., Woodbury, A., 2001. A Bayes tour of inversion: A tutorial. Geophysics 66, 55–69.

Walsh, J.B., 1995. Seismic attenuation in partially saturated rock. J. Geophys. Res. 100, 15407. doi:10.1029/94JB03264

Walsh, J.B., 1966. Seismic Wave Attenuation in Rock Due to Frcition. J. Geophys. Res. 71, 2591–2599.

Walsh, J.B., 1965. The effect of cracks on the compressibility of rock. J. Geophys. Res. 70, 381–

389. doi:10.1029/JZ070I002P00381

Wang, D.-X., 2017. A STUDY ON THE ROCK PHYSICS MODEL OF GAS RESERVOIR IN TIGHT SANDSTONE. Chinese J. Geophys. 60, 64–83. doi:10.1121/1.1908239

White, J.E., 1975. Computed Seismic Speeds and Attenuation in Rocks With Partial Gas Saturation. Geophysics 40, 224. doi:10.1190/1.1440520

White, J.E., Mihailova, N., Lyakhovitsky, F., 1975. Low‐frequency seismic waves in fluid‐saturated layered rocks. J. Acoust. Soc. Am. 57, S30–S30. doi:10.1121/1.1995164

Wood, A.B., 1955. A textbook of sound, Third Revi. ed. Macmillan Co., New York.

Wu, R.-S., Aki, K., 1988. Multiple scattering and energy transfer of seismic waves—Separation of scattering effect from intrinsic attenuation II. Application of the theory to Hindu Kush region. Pure Appl. Geophys. PAGEOPH 128, 49–80. doi:10.1007/BF01772590

Zener, C.M., Siegel, S., 1949. Elasticity and Anelasticity of Metals. J. Phys. Colloid Chem. 53, 1468. doi:10.1021/j150474a017

Zhao, W., Li, H., Yao, F., 2004. Attenuation Characterization of seismic waves in the wavelet domain and th detection of gas, in: SEG Int'l Exposition and 74th Annual Meeting, Denvor, Colorado. pp. 8–11.

Zhu, T., Harris, J.M., 2015. Improved estimation of P-wave velocity, S-wave velocity, and attenuation factor by iterative structural joint inversion of crosswell seismic data. J. Appl. Geophys. 123, 71–80. doi:10.1016/j.jappgeo.2015.09.005

Zimmerman, R.W., 1991. Compressibility of sandstones. Elsevier.

Chapter 5 **Summary**

The dissertation consists of three technical papers. The first one is committed to investigate the Q measurement which is the base of the following research. The goal of this paper is to provide a guideline when conducting CFS, SRM, or PFS, to make sure the estimated Q is reliable. By comparing the synthetic data simulated through different data preprocessing techniques under different given conditions, we conclude:

- The best window size when truncating signals as the source or received wavelet is 1.8 times of the signal period;
- Q measurement for highly attenuated rock, e.g., sediments with large amount of gas or thick layers, would be more reliable;
- the effective-bandwidth coefficient within 0.2 ~ 0.4 is a good value;
- any pair of technique I or IV and CFS or SRM could be the optimal choice of methods and techniques, namely imposing the FFT for spectral transformation and/or wavelet estimation for restoring the interfered waveform;
- technique IV is superior once in practice where there is a "thin layer" effect;
- the estimation error generally increases with larger amounts of noise or smaller S/N;
- the higher frequency data has lower estimation errors.

The second paper aims at realizing the joint Q_p and Q_s inversion. The workflow consists of the rock physics model construction (only DM model is covered), sensitivity analysis, Bayesian model establishing, and the sampling scheme choice. The whole workflow is carried out on OBS data from Finneidfjord, Norway. By joint inversion, we reach:

- Q is more effective than velocity in rock property inversion;
- the additional Q_s reduces the ambiguity of the inverse problem, allows us to invert one more rock property;

- Bayesian model is powerful in solving a highly nonlinear problem;
- the attenuation inversion bears the ability to quantify even very small amount of gas.

The last paper covers a more general and more advanced inversion workflow. We construct an attenuation inversion approach which allows to integrate seismic data with sonic log data and offer three rock physics models as candidates for this workflow in case of different geological settings. The basic steps are the same as the second paper. But we could invert four parameters instead of two from the sensitive parameter pool. This workflow provides readers a higher degree of freedom to reproduce our work or apply the proposed workflow to their special cases. Besides the points from the second paper, we have more awareness:

- when solving the Bayesian model, posterior integration method is less efficient than the MCMC approach;
- the inversion could be implemented on unconventional gas reservoirs such as shale gas, tight gas, or coalbed methane only if we find a proper rock physics model to describe the storage state of the gas;
- three rock physics models all simulate the wave-induced fluid flow in the mesoscopic scale. The only difference among them is the patch geometry, which corresponds to different storing states of gas.

Recommendations and Potential Future work

The complete attenuation inversion workflow for rock property estimation in this thesis is solid and significant in industrial application. For example, it can be used to validate Q, which is important in Q compensation, by comparing the inverted rock properties with those of logs; the attenuation-based gas saturation estimation can avoid false direct hydrocarbon indicator (DHI) because of its stronger response to gas inclusion; or it can assist to monitor CO_2 injection through

inverting time-lapse seismic data. However, there is still room to improve it. Firstly, in the chapter 4, the integration of sonic logs leads to the property estimation localization problem. Namely, the estimated properties can only stand for those near the well location. A potential solution to this problem might be to spatially intercept the logs if enough number of wells available, or to add more information such as velocity models or frequency-dependent reflectivity models into this attenuation workflow, which are more widely distributed in spatial space. Secondly, if we could have instantaneous Q values for the whole profile/cube (e.g., Q estimation by the Q tomography technique), a detailed S_g or other property profile/cube is easily to be obtained through the proposed workflow, which is going to be more informative than the single layer estimation. Lastly, the characteristic size discussed in this dissertation, which has significant impacts on the attenuation inversion, is hard to be determined. Further work on its determination is a potential way to improve the inversion workflow.

Education

2014–Present	Ph.D.	Energy and Mineral Engineering, Penn State University
2011–2014	M.S.	Geophysics, China University of Geosciences Beijing
2007–2011	B.S.	Geophysics, China University of Geosciences Beijing

Research Interest

I have research experiences in seismic data acquisition, forward modeling, acoustic or elastic impedance inversion, and rock physics. My current research interest focuses on seismic attenuation inversion, including *Q* estimation, wavelet estimation, rock physics models, and stochastic inversion.

Research Experience

- August 2014 - Present, Research Assistant, Seismic Attenuation Inversion for Reservoir Characterization
- June 2012 - May 2014, Seismic Geometry Design on the Complex Seismic Condition in Puyang Oilfield
- December 2011 - May 2012, Special Seismic Data Inversion: Gas Hydrate Exploration in the South China Sea
- February 2011 - July 2011, Research of Geophysical Anomaly Features of Gas Hydrate in the North of South China Sea

Research Publications

- Chen, Y., K. Dunn, X. Liu, M. Du, X. Lei, 2013, New Method for Estimating Gas Hydrate Saturation in Shenhu Area: Geophysics, 79(5), IM11-IM12.
- Lu, L., X. Lei., & X. Liu, 2013, Prediction of Porosity in the North Margin of South China Sea: Chinese J. Geophys. (In Chinese), 56(2): 601-607.

Papers Presented

- Lei, X., C. E. Morgan, 2017, Characterization of Gas-charged Sediments from Joint Inversion of Q_p and Q_s with sonic logs, Oral presentation at SEG International Exposition and 87th Annual Meeting in Huston, Texas.
- Lei, X., C. E. Morgan, 2016, A Comparison of Methods for Estimating *Q*, E-presentation at SEG International Exposition and 86th Annual Meeting in Dallas, Texas.
- Lei, X., C. E. Morgan, 2015, Characterization of Gas-charged Sediments from Joint Inversion of Q_p and Q_s, presented at SEG International Exposition and 85th Annual Meeting in New Orleans, Louisiana.
- Lei, X., Y. Liu, X. Liu, 2014, Assessment of Seismic Geometry Footprints Based on Common Focus Point Concept: CPS/SEG Beijing-2014 International Geophysical Conference.